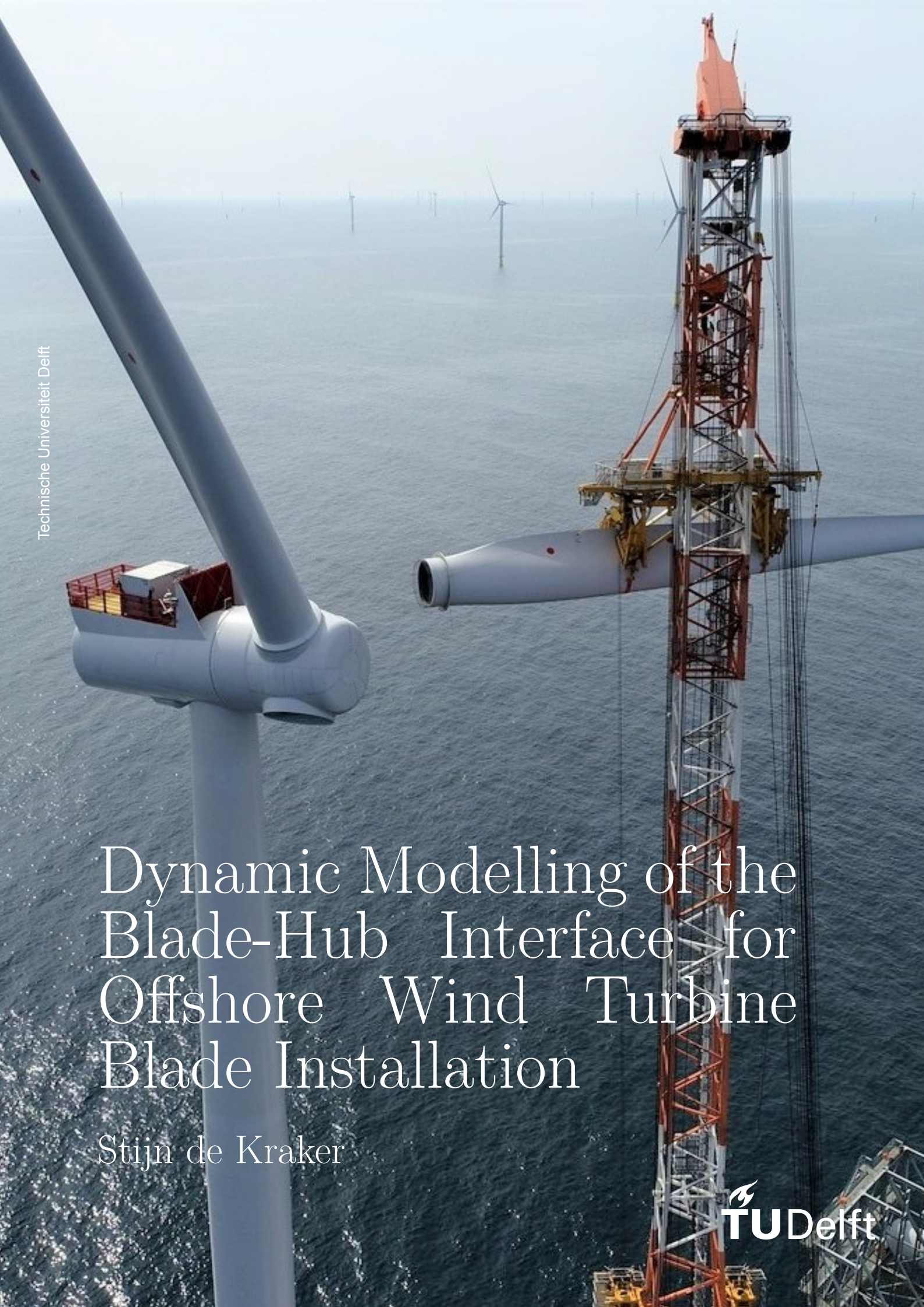

Technische Universiteit Delft

Dynamic Modelling of the Blade-Hub Interface for Offshore Wind Turbine Blade Installation

Stijn de Kraker

TU Delft

Dynamic Modelling of the Blade-Hub Interface for Offshore Wind Turbine Blade Installation

by

Stijn de Kraker

to obtain the degree of Master of Science
at the Delft University of Technology,
to be defended publicly on February 17, 2023.

Student number:	4466330	
Project duration:	February, 2022 – February, 2023	
Thesis committee:	Prof. dr. dr. A. Metrikine,	TU Delft, supervisor
	Dr. ir. B.C. Ummels,	TU Delft
	Dr. ir. J. Breukels,	Allseas Engineering
	Dr. ir. N. Mallon,	Allseas Engineering

An electronic version of this thesis is available at http://repository.tudelft.nl/.

TU Delft Allseas

Abstract

In the last decades, the urgency for sustainability has dawned on humanity. The increasing pressure for more renewable energy sources is accompanied by the success of the offshore wind turbine. As a result, the installation of offshore wind farms has become a major business. The challenges posed during installation become more complicated with larger turbines. Forces exerted on taller and softer support structures and longer blades limit the installation options of the wind turbine components even more. Nevertheless, the dimensions of wind turbines have grown explosively over the years and this growth is foreseen to continue.

To overcome the growing challenges of blade installation on offshore wind turbines, it is crucial to better understand the forces and the induced motions. Insufficient understanding of the behaviour of the support structure and blade during installation of the latter could lead to over-conservatism of an already vastly time-constrained process, resulting in loss of workable weather and unnecessary costs.

The objective of the research conducted in this thesis is to develop a dynamic model of a 20 MW offshore wind turbine to quantify motions at the blade-hub interface during blade installation and examine potential mitigations. When the objective is reached, a good comprehension of the blade behaviour is achieved, allowing for exploration of solutions to reduce the observed motions and increase workability.

A 20 MW wind turbine does not exist as of writing, but with a scaling assessment a configuration was composed. The future wind turbine is estimated to have a hub height of 154.7 m and a blade length of 131.5 m with an estimated weight of slightly less than 90 tonnes. Due to offshore placement of the wind turbine, the length of the support structure is estimated to be extended with a water depth of 35 m. The problem has been further delineated by assuming the weather conditions of a typical North Sea offshore site at the boundary of what is currently possible for blade installation. Installation is assumed to be conducted with a floating vessel, posing even more challenges.

Modelling the installation of a blade is subdivided into examining the behaviour of a wind turbine support structure and a blade suspended from a crane separately. The performed simulations are conducted in 3D, with the support structure and blade being multi-body systems excited by unidirectional waves, wind and current. Calm, normal, and rough weather conditions are assumed as input conditions to examine the environmental impact. A combination of the results of the models simulating the multi-body systems provide the relative motions between the support structure and the blade, resulting in potential impact velocities in the horizontal plane. The model is solved in the time domain, because it allows for a better understanding of the input and output variables.

The simulation results indicate that in a calm sea-state, the maximum potential impact velocity of the wind turbine blade resulting from the simulations is 0.21 m/s. After applying mitigations to the simulated motions, this velocity can be reduced to 0.14 m/s. The results show that specifically dampening the first mode shapes of the support structure and the yaw and pendulum mode shapes of the blade blade effectively reduce the motions to a level that safe installation could be ensured.

Multiple case studies are examined, resulting in parameters and states that lead to circumstances under which blade installation is not feasible. Only the case studies in which calm weather conditions are assumed, single blade installation may be possible, but only if sufficient mitigation has been applied. Initial environmental and structural damping insufficiently attenuates the motions of both structures.

Damping is currently added using damping coefficients. To figure out exactly how much damping is required to safely install a blade and to what extent this is achievable with a tagline, an even more extensive configuration of the model is required. It is recommended to include spring-damper systems resembling the taglines and an aerodynamic profile of the blade.

Preface

I am grateful to announce that an incredible journey is coming to an end. I am proud of what I achieved in almost twelve months and of the difficulties that have been overcome. Something that beforehand appeared to be one of the greatest obstacles for me as a student has turned out to be enlightening process.

I would like to express my gratitude to everybody that was of importance in helping me to complete this research. In addition, I would like to thank the institutes that facilitated the opportunity of conducting such an educative and pleasurable project. Performing on a level to be able to deliver a graduation thesis was not possible without the features provided by the TU Delft and Allseas Engineering. In particular I would like to thank:

Bart Ummels, for your unwavering support, advice, and introduction to the offshore wind industry throughout the year. I could never imagine a person being more enthusiastic and well informed on the most current facts about the offshore wind industry. The enthusiasm had a beneficial effect on the progress of this study. I appreciated how well we interacted and I would recommend you to anyone asking for knowledge of the wind industry.

Niels Mallon, for guiding me in the right direction throughout the modelling phase of this conducted research. The ideas you have provided me with were decisive in achieving the results of this graduation project.

Jeroen Breukels, for giving me the opportunity to start a graduation project at Allseas Engineering. The expertise on how to properly conduct a research project has proved extremely valuable, for which I am very thankful.

Andrei Metrikine, for encouraging me to pursue the challenges posed by structural dynamics, of which I thought I already had a reasonable amount of knowledge. However, your knowledge made me realise that much more can be aspired to.

My colleagues at Allseas Engineering, for bearing with me after the countless questions. The answers have undoubtedly resulted into the study it has become and that I could not have achieved what I achieved up to this day without my colleagues.

Stijn de Kraker
Delft, February 2023

Contents

List of Figures

List of Tables

Nomenclature

a_{wave}	Wave acceleration
A_i	Wave amplitude
A_{wind}	Wind contact surface
α	Angle of attack
α_0	Power law coefficient
B_j	Damping
C_D	Drag coefficient
C_M	Inertia coefficient
D_1	Monopile diameter
D_{hub}	Hub diameter
D_{ou}	Outer diameter
D_{in}	Inner diameter
D_{rotor}	Wind turbine rotor diameter
E	Modulus of elasticity
f_n	Natural frequency
$F_{current}$	Current force
F_{waves}	Wave inertia and drag force
F_{wind}	Wind force
γ	
h	Height
h_{ref}	Reference height
H_{crane}	Crane tip height
H_{hub}	Hub height
H_{max}	Maximum wave height
H_{lift}	Load lift height
H_s	Significant wave height
I_j	Mass moment of inertia
$I_{yy,j}$	Area moment of inertia
k	Wave number
K_1	Longitudinal cable stiffness
L_c	Chord length
L_{cable}	Hoist cable length
L_j	Segment lengths
λ_{wave}	Wave length
$\lambda_{Zephyros}$	Scale factor Zephyros
MSL	Mean Sea Level
$\overline{M_j}$	Modal mass
M_j	Segment mass
M_t	Top mass
ω_i	Wave frequency
ω_n	Natural frequency
ω_p	Peak frequency
ω_r	Damped natural frequency
Ψ	Eigenvector modeshape
q_j	Generalised coordinate
R	Dissipation
R_j	Rotational stiffness
RAO	Response Amplitude Operator
RNA	Rotor Nacelle Assembly
ρ_{air}	Air density
ρ_{water}	Water density
ρ_{steel}	Steel density
r/R	Normalised blade span position
S_ζ	Spectral density
σ	
t	Wall thickness
T	Kinetic energy
T_p	Peak period
θ_j	Degree of freedom support structure
U_i	Blade velocity
$U_{current}$	Current velocity
U_{wave}	Wave velocity
$U_{wind,mean}$	Mean wind velocity
$U_{wind,std}$	Standard deviation wind velocity
V	Potential energy
W	Work
z_0	Roughness length
ζ_i	Modal damping coefficient

$\overline{\zeta_{sea-state}}$ Wave elevation sea-state profile

$1P$ Rotor frequency

$3P$ Blade passing frequency

$\overline{\zeta_{wind}}$ Wind velocity profile

C_a Added mass coefficient

M_added Water added mass monopile

M_blade Blade mass

M_inside Mass inside monopile

M_yoke Blade yoke mass

1

Introduction

1.1. Offshore wind industry status

In 2016, the Paris Agreement was signed by 196 countries. It legally binds countries to limit global warming to well below 2, preferably 1.5 degrees Celsius increase. For the Netherlands, this means a 49% reduction in greenhouse gas emissions compared to 1990. The increasing pressure for sustainability is accompanied by the success of the wind turbine and the last couple of years especially the offshore wind turbine. Offshore wind farms are important because offshore the wind is the strongest and wind turbines can thrive with less restrictions. The wind turbine industry is constantly growing and governments are setting targets for their country's wind industry that ensure this growth for the foreseeable future. Figures 1.1a and 1.1b demonstrate the global growth over the last decade, a period of increasing environmental awareness. During this period, installed offshore wind capacity increased tenfold. To put the installed power in perspective, the global energy consumption in 2020 has been taken as an illustration. To generate sufficient power with offshore wind turbines alone to meet the global consumption of 2020, every wind turbine must operate 354 hours in a day for a whole year at maximum output. The statistics illustrate the picture of both huge strides being made and a great deal that remains to be done. The global statistics shown in figure 1.1 are especially boosted by the Chinese market. In that country, onshore and offshore wind farm projects have increased exponentially in recent years, but it still accounts for only 6.1% of total power generation in China [14].

(a) (b)

Figure 1.1: Global installed wind power statistics [1].

When looking at the European market, figures 1.2a and 1.2b give an indication of the status of offshore wind energy in Europe. By 2021, Europe installed 5,795 offshore wind turbines, which together generate circa 28 GW and provides 15% of Europe's electricity consumption [15]. For five years the European wind energy grew on average by 3 GW, with the United Kingdom being the main contributor. The European expansion of offshore wind in the last decade is remarkable, but the forecast of the following ten years indicates that the European industry is far from being where it wants to be. Figure 1.2b predicts 102.6 GW newly installed wind power by 2030, although some studies forecast these numbers will already be achieved in 2025 [16].

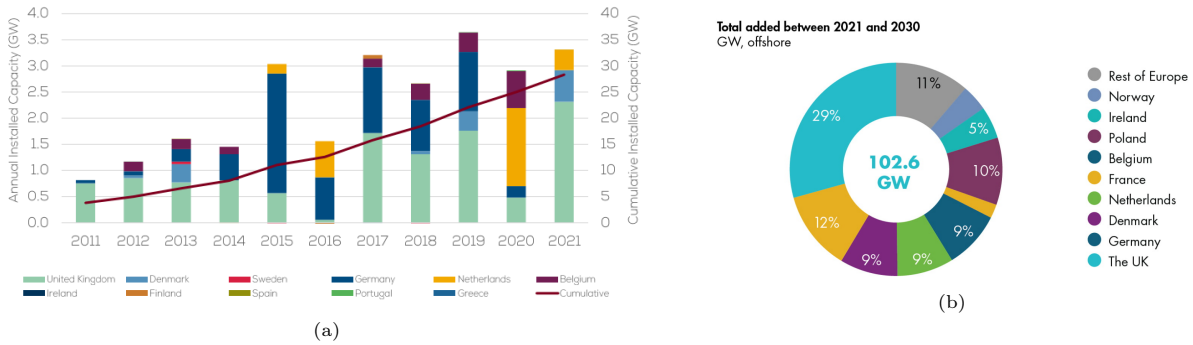

(a) (b)

Figure 1.2: Offshore wind turbines in Europe [2].

To achieve climate neutrality, Europe has set targets for offshore wind increasing to 450 GW by 2050. Almost half that is installed in the North Sea. The North Sea is very suitable for wind farms due to relatively shallow waters, a favourable wind climate and a proximity of great ports and energy consumers [17]. But even the North Sea has limited space. Vessel manoeuvring space is limited by a wall of wind turbines, with higher risk of accidents. In addition, huge investments are needed in offshore grid connections and in the reinforcements of onshore grids. Furthermore, ports need 6.5 billion of investments over the decade to prepare for the 2030 targets [2]. However, that does not stop the tremendous development in the industry.

The Dutch government announced in 2022 that it wants 21 GW of offshore wind installed in the North Sea by 2030. Offshore wind could provide 16% of dutch energy consumption if that objective is realised [17]. The target for 2023 is set at 4.5 GW of offshore wind energy, supplying 3.3% of all the energy in the Netherlands. To achieve the goals set by the government, not only more turbines will be installed but, more importantly, turbines with more capacity are introduced. The Netherlands was lagging behind in recent renewable energy sources, but installed a record setting 1.5 GW in 2020. Globally, only China outperformed the Dutch that year [18].

1.2. Scale of future wind turbines

Wind turbine technology development never pauses. The key to reaching the targets set is not only in quantity, but also in quality of the wind turbines. Onshore and offshore wind turbines have continued to evolve in scale over the years, especially in size. But where the growth of onshore wind turbine dimensions encounter a limit, offshore turbines kept growing. Appendix B elaborates on the evolution of the offshore wind turbine. For example, the largest wind turbine ever installed when this graduation work was commenced, has been surpassed for some time already. The advantage of a taller wind turbine with a larger rotor is the power output. The power output is calculated using equation 1.1. Increasing the rotor diameter D increases the power output quadratically. In addition, equation 1.1 shows that the power output scales proportionally with the wind velocity U_{wind} cubed. The larger wind turbines reach to unprecedented heights, accompanied by higher wind velocities at these heights.

$$P = \frac{1}{2}\rho_{air}\frac{\pi}{4}D_{rotor}^2 U_{wind}^3 \tag{1.1}$$

Figure 1.3 depicts the expansion of the dimensions. And looking at the current development, the future is now. 10 MW wind turbines are already being realised and the possibilities of a 20 MW turbine are being explored. According to the literature from 2009 underlying figure 1.3, a 20 MW could end up having a rotor diameter of 250 m a hub height of 170 m. One can imagine that such large structures onshore would receive adverse reactions. Hence, wind turbines of that size will only appear offshore.

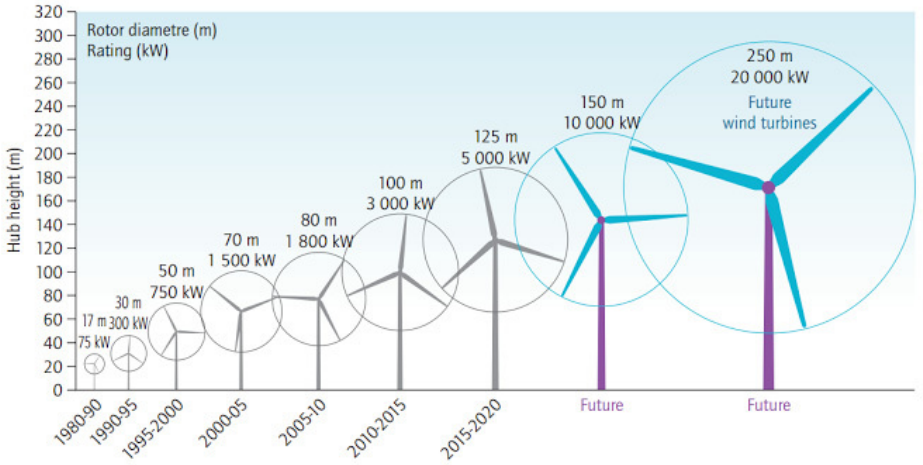

Figure 1.3: Wind turbine expansion [3].

Figure 1.4 shows that most offshore wind turbines are supported by a monopile. For offshore wind turbines, monopile foundations are most frequently employed and are used at water depths of up to 50 to 60 metres. Monopile foundations are preferred over other solutions because of their low manufacture, transport, and installation costs as well as their low risk profile. Because of this, monopile foundations are used by more than 80% of the wind turbines that are currently operational in the North Sea [19].

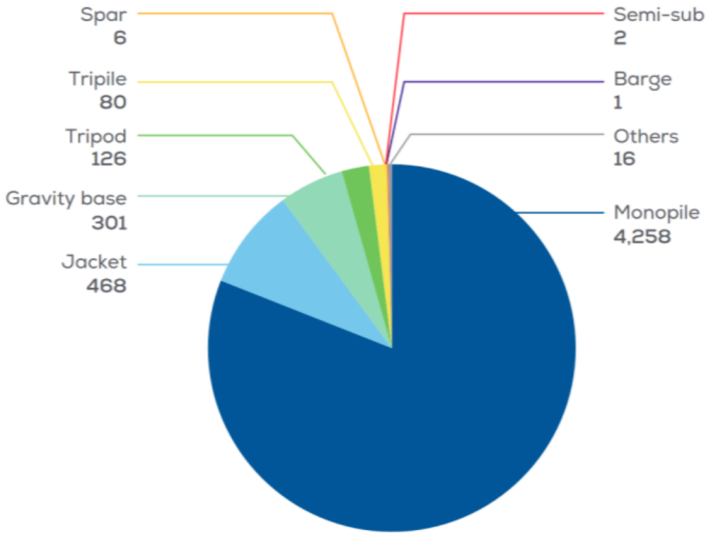

Figure 1.4: Number of foundations of offshore wind turbines in Europe by substructure [4].

1.3. Installation process

A constantly growing wind turbine industry presents challenges. The pressurised construction supply chain and the equally complicated installing process delay a sustainable tomorrow. The installation process starts with the monopile being inserted in the seabed, whereafter the transition piece and tower components are carefully connected to the monopile in that order. These elements combined comprise the support structure. Next, the moving parts of the turbine are installed. Firstly, the nacelle, which contains the drive train of the wind turbine, is hoisted on top of the support structure. Secondly, the hub is attached to the nacelle. The hub is the connection between the drive train and the blades and allows the rotor to rotate. Lastly, the blades are mated to the hub. The blades and hub together are the rotor of the wind turbine.

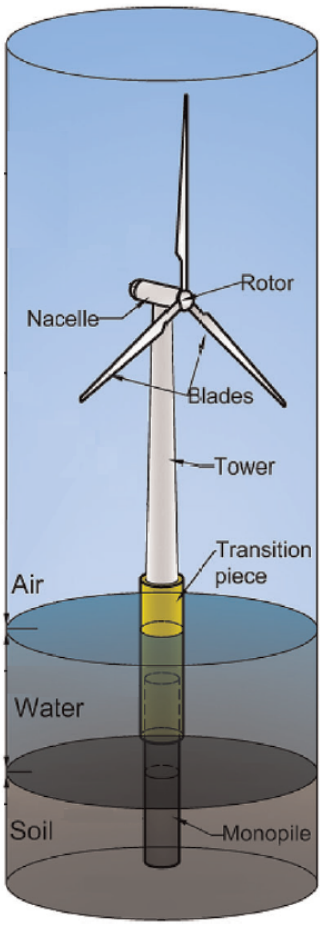

Figure 1.5: Schematic offshore wind turbine terminology [5].

To install wind turbines offshore of up to 20 MW in the future with the dimensions mentioned in previous section, it would require a crane that reaches hundreds of metres in height and can also lift hundreds of tonnes. On top of that, the conditions at sea are never perfect. Currently, the most advanced approach to overcome those problems is a jack-up lift vessel. Such a vessel type is known for being stable. The present largest ship of this type is the Voltaire owned by Jan de Nul [20]. It is suitable for installing the Haliade-X 14 MW turbine by General Electric, which was for the first time commercially ordered for the Dogger Bank C project whose construction begins in 2025. More on jack-up lift vessels can be found in section 2.7. Installing wind turbines with jack-up lift vessels is a technique developed for shallow water depths and relatively small wind turbines. With the expansion drift of the offshore wind turbine industry and the shallow waters getting very crowded, new concepts are being explored. Installing offshore wind turbines in deeper waters with floating vessels is one of them.

The installation process of an bottom founded offshore wind turbine is very delicate as damage to a wind turbine can be a costly delay. However, one thesis cannot cover the entire installation process described above and therefore this research focuses on one of the closing stages, installing a wind turbine blade. A costly delay can occur during the alignment and mating phase of a blade being installed. If something catastrophic happens to a bolt, intended to secure the blade to the hub, the blade might have to be hoisted back to the deck of the installation vessel for repair. Insufficient understanding of the behaviour of the support structure and blade during installation of the latter could lead to over-conservatism of an already vastly time-constrained process, resulting in loss of workable weather and unnecessary costs. The motions of the blade and support structure should be analysed to prevent this from happening. Predicting the motions induced by a given sea-state is part of the preliminary examination that precedes installation.

1.4. Blade-hub connections

Installing a blade includes securing the blade to the hub. The blade is connected with the hub through the blade root. Blade root designs have varied over the years and the most common one, the T-bolt joint, is discussed below. The design of the connection was driven by cost, which typically represents 20% of the blade cost [21].

The T-bolt joint is a widely used industrial connection. The main elements are the nut and the screw attaching specifically the blade root laminate to the hub. Figure 1.6a supports the explanation, some of the components are also visible in figure 1.6b. The nut, a transverse cylinder, receives the load from the blade root laminate and transfers it to a tension bolt, located in a hole drilled in the laminate. A high pretension in the bolt makes sure the fatigue loads of the screw are minimised and prevents fatigue from happening in the bolt. The T-bolt joint is one of the most efficient joints for large blade roots due to the omission of adhesives and therefore provides long-term performance [22].

When the final phase of mating is entered, as illustrated in figure 1.6b, significant risks of impact can appear frequently. When sideways motions of the blade or hub occur, it could damage a bolt or guide pin and repairs might be necessary. If an incident occurs, delay is inevitable.

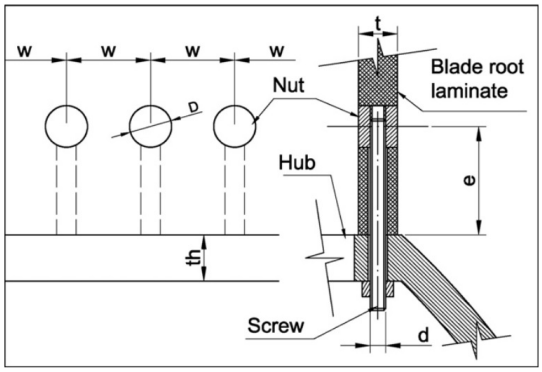

(a) T-bolt joint, including main components and typical design variables [23].

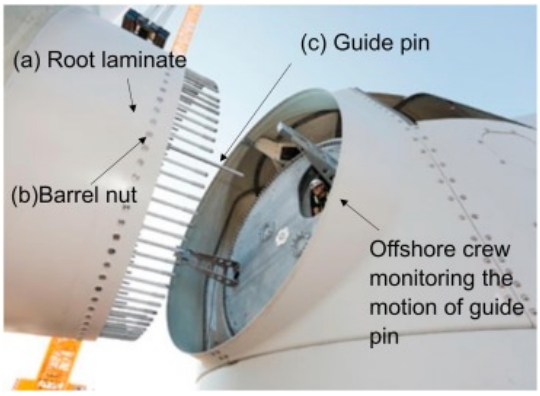

(b) Mating phase of a single blade to the hub [24].

In appendix B.2 a further study of blade-hub interfaces is conducted. Various types of current and future blade-hub connection designs are discussed including some results of these connections being used in the future 20 MW offshore wind turbines.

1.5. Research objective and question

As stated in previous sections, offshore wind turbine installation is very challenging. With the scaling of wind turbine structures come new challenges, but nothing insurmountable, as proven over the past decades. An objective of this research is to overcome challenges that arise during the design stage of the wind turbine and during the installation phase of the blades of a 20 MW turbine. However, this requires observing all components listed in previous section, since the properties of those components already installed, affect the motions that are being analysed. The selected type of foundation used in this thesis is the monopile, as this is and will remain the most commonly used bottom founded support structure for the upcoming future [25]. The result will determine whether a project is feasible. The main objective of this research reads:

"To develop a dynamic model of a 20 MW offshore wind turbine to quantify motions at the blade-hub interface during blade installation and examine potential mitigations."

The main research question of this research reads:

"How can the motions of a 20 MW offshore wind turbine nacelle-hub assembly and a rotor blade during installation be modelled and managed as to maximise weather workability?"

The following sub-questions have been listed to support the main research question:

1. What are the characteristics of a future 20 MW offshore wind turbine?
2. Which combinations of forces shall be considered during blade installation?
3. How can an offshore wind turbine support structure with a nacelle-hub assembly be modelled?
4. How can an offshore wind turbine blade be modelled during blade installation?
5. What are the motions of the hub-blade interface?
6. Can the hub and blade motions be effectively reduced to maximise installation feasibility?

1.6. Methodology

To achieve a result that suffices the research objective and questions, the research followed a specific sequence of stages. The thesis will be subdivided into two parts. The first part outlines the preliminary study before creating the multi-body systems. The second part is aimed at the simulation of the wind turbine support structure and blade with the help of multi-body dynamics. The accompanying research questions are mentioned along the corresponding stage.

Part 1: Preliminary study prior to model development.

1. Conduct a study on the properties and dimensions, including the installation phases, of (offshore) wind turbines.
2. Collect metocean data in order to enable quantification of wave, current and wind forces.
3. Perform a wind turbine scaling assessment, concluding in a 20 MW offshore wind turbine (RQ 1).
4. Visualise the research objective by portraying the multi-body system with the established delineations.

Part 2: Dynamical modelling of offshore wind turbine support structure and blade.

1. Quantify the unidirectional, but independent, wave, current and wind forces supported by either a wave or a wind spectrum (RQ 2).
2. Quantify the motions in a 3D model of a bottom founded support structure including nacelle and hub by analysing the multi-body dynamics of the structure in Matlab (RQ 3).
3. Quantify the motions in a 3D model of a blade suspended from a crane on a floating vessel by analysing the multi-body dynamics of the blade in Matlab (RQ 4).
4. Combine the support structure and blade motions to apprehend the motions of the blade root relative to the hub (RQ 5).
5. Assess the impact of mitigations in an effort to optimise blade behaviour during the blade installation phase (RQ 6).

1.7. Scope delineation

Installing a wind turbine offshore is very challenging and the installation phase can be divided in several components. The component this research focuses on is the blade and installing a blade can be subdivided into multiple stages. The complete blade installation phase and the corresponding stages are not all equally important to be able to achieve the research objective and thus a breakdown of these stages and a delineation of the scope is given. During blade installation, the blade is not the only component that is analysed as the research questions can only be answered by taking the motions of the support structure, the blade and if required the installation vessel into account. Thus the design of a support structure is included in the scope of this research. Additionally, selections are made that change variables into parameters. For example, choosing a specific installation site fixes the value for water depth and by only taking the 20 MW turbine into account, support structure dimensions are fixed as well.

Another choice to be made is if the model is solved in the time domain or the frequency domain.

1.7.1. Site selection

This research is aimed at the behaviour of a 20 MW turbine, which will not be installed in the near future. Therefore the selected sites cannot be areas where construction may soon take place. The expectation is that 20 MW turbines will be commissioned at the end of this decade, so locations that are also being commissioned around that time are selected for this research. The Dutch government announced a plan to nearly double the total planned capacity for offshore wind by introducing multiple new locations. Nederwiek and Doordewind are two of those designated areas that enter service in 2030. Figure 1.7 shows the location with respect to other European offshore wind energy sites. The exact locations of the individual wind turbines in both sites are not yet available, but coordinates somewhere in the aforementioned areas, which are not necessarily the definitive locations where the wind turbines will be placed, are estimated with the help of the global offshore renewable map, created by 4C Offshore [6].

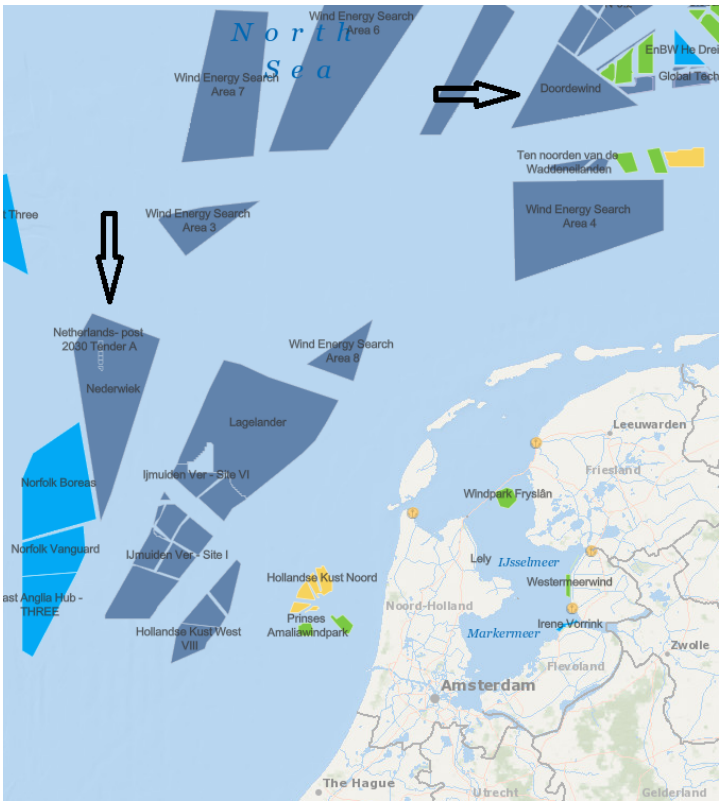

Figure 1.7: Offshore wind energy locations off the Dutch coast [6].

The two sites both have an average water depth of circa 35 m with a small standard deviation. By choosing these specific sites for this research, the water depth gets eliminated as a variable. Table 1.1 provides the power output of both offshore wind locations.

Table 1.1: Power output of Nederwiek and Doordewind

Wind Farm	Total power [MW]
Nederwiek	6000
Doordewind	4000

1.7.2. Time-domain vs. frequency-domain

The multi-body system is analysed in the time-domain to properly display physical signals, mathematical functions, or time series of environmental data. In the time-domain, the modal analysis is straightforward, whereas in the frequency domain the analysis is much more complicated and requires the evaluation of nonlinear Eigenmodes. A stability analysis in the time-domain will be much more

expensive from the computational point of view, partly because the step size must be kept small to obtain accurate results.

Nevertheless, the multi-body system is solved in the time-domain, in which a graph shows how a signal changes over time ensuring a deeper comprehension of a system's structural behaviour. A frequency-domain graph shows how much of the signal is contained inside each given frequency band throughout a range of frequencies.

2

Wind turbine characteristics

This chapter provides an insight into the offshore wind turbine community. Firstly, all important components of an offshore wind turbine used for this research are described. Secondly, a more extensive explanation on the installation process is provided.

2.1. Support structure

The support structure of an offshore wind turbine described in this thesis consists of a monopile, a transition piece and a tower. The support structure, consisting of monopile, transition piece and tower, must be capable of withstanding enormous forces from not only waves and wind, but also the weight of the rotor-nacelle assemblies (RNA) listed below in table 2.1. Figure 1.5 displays every component of an offshore wind turbine. The rigidity of the monopile and tower is an important parameter for the deflection, velocity and natural frequency of the structure. At larger sizes, the tower might be transported and installed in sections. The transition piece is the component that connects the monopile with the tower and is installed separately, but new designs are introduced with the transition piece integrated with the monopile. The transition piece can always be distinguished by the yellow colour. Monopiles and tower components could have a mass up to 2000 tonnes or more.

2.2. Nacelle

The nacelle is the component that conceals the drive-train of the wind turbine. This is a heavy component that can potentially have a weight over several hundred tonnes. Connected to the nacelle is the hub. The hub is part of the rotor and attaches the blades to the drive train.

2.2.1. Drive train

The drive train of a wind turbine has the following elements. An above mentioned hub, a main bearing, a main shaft, a brake and a generator are all components of a direct-drive wind turbine generator. A geared-drive generator has more to it, as can be observed from figure 2.1. A geared-drive generator additionally features a gearbox and a high-speed shaft for the sole purpose of rotating the generator at high velocity. A higher velocity is accompanied with a smaller generator, which means the geared-drive generator is more compact than the direct-drive counterpart.

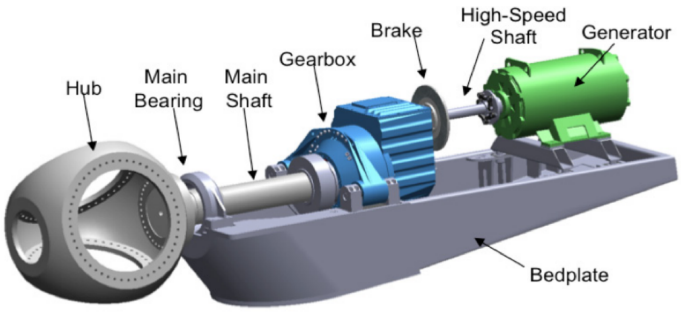

Figure 2.1: Geared-drive generator [7].

A direct-drive wind turbine has the advantage over a geared drive wind turbine of not having a gearbox and eliminating gearbox failure and maintenance and downtime effects. The nacelle of a direct-drive wind turbine is considerably smaller, in particular due to in the absence of a gearbox. These advantages do not necessarily make direct-drive wind turbines more preferred, as there are other factors and reliabilities to take into account. Next to the already mentioned characteristics, the fact is that the energy generating concept of a direct-drive wind turbine is much larger in dimensions with higher total costs [26]. The power electronics partly or fully decouple the rotor mechanical frequency from the grid electrical frequency to enable variable-speed operation [27]. Primarily due to the elimination of extensive maintenance, a direct-drive wind turbine is preferred offshore.

2.3. Rotor characteristics

The rotor is what makes the drive train rotate. It comprises of three blades and a hub, although there are designs with a different amount of blades. A hub consists of two parts, the load carrying structure and the nose cone or spinner. The load carrying structure inside the hub transfers all loads from the blades to the main shaft. Because this component must bear large forces, it is typically made of cast iron. The nose cone is the aerodynamic cover of the hub and is typically made of composite or sheet aluminum. Connections between different materials are often called hybrid connections, which is applicable in this case as the blade is a laminate and the rest of the turbine is made of steel.

2.4. Blade design

A wind turbine blade is designed to create lift and drag forces, that act on the rotor. This is accomplished by extracting energy form the wind by decelerating it. If the lift force is greater than the drag force, the rotor starts to rotate. Blades have a complicated aerodynamic profile and are anisotropic, which means that the material has different properties in different directions.

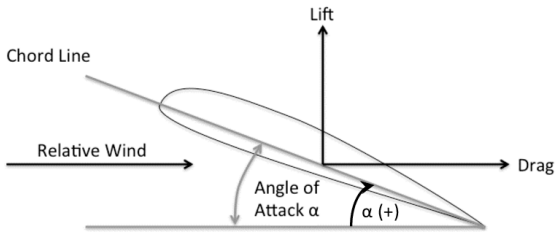

Figure 2.2: Wind turbine aerofoil.

The lift and drag of the aerofoil in figure 2.2 produce an aerodynamic load, which is influenced by the relative wind velocity. The relative velocity is a summation of the wind velocity and the blade velocity. The angle of attack depends on blade twist and pitch and varies along the length of the blade. The generated aerodynamic lift and drag are converted into effective thrust that is absorbed by the generator and reaction forces in the direction of rotation.

2.4.1. Blade load characteristics

The blade hub connections of a wind turbine are subjected to severe fatigue loading. A blade has a design life of circa 25 years. In these years, it will suffer circa 100 million load cycles due to wind shear, gravity loading and wind gusts [10]. At the blade root, the involved unidirectional fibre oriented composites abruptly end, because it is a hybrid connection and the blade and hub are not intertwined into one another. This causes unwanted shear stresses in the laminate's resin and adhesives. The shear strength and stiffness of both are significantly less than the axial strength generated by the composites and that will mean that a far greater number of composites will be needed in the blade root. This and the existence of gaps as a result of the connections are factors that require additional material to enable sufficient load transfer and makes it so that the cylinder is tapered. Connections increase vulnerability to crack growth and damage, a connection provides a location for crack initiation, growth and a way in for moisture. This element contributes to a connection which contains less holes, contrary to the factors that contribute to more holes. This trade-off will be discussed later in this report in section B.2.1.

The development of IntegralBlade technology enables each fiberglass-reinforced epoxy blade to be cast in one piece. This process eliminates weaker areas at glued joints and produces blades of optimum quality, strength, and reliability [28]. In order to maximise the efficiency of the joint, it is necessary to understand the failure modes of the laminate, providing experimental failure loads and describing failure mechanisms.

2.5. Reference Wind Turbines

Reference wind turbines are designed to be used as a baseline that is defined with publicly available design parameters for studies that explore innovative technologies that might be implemented in wind turbines. Also, the reference wind turbines offer an entry point for newcomers to wind energy. The characteristics of the International Energy Agency (IEA) 15 MW Offshore Reference Wind Turbine are listed in table 2.1 together with the characteristics of the DTU 10 MW Reference Wind Turbine [29, 30]. The blade design of the 10 MW turbine is used as the benchmark of the 15 MW blade design. Both use the same FFA-W3 aerofoil series with a different scale factor [29]. In this research, the hub height is the altitude of the hub compared to the mean sea level. Table B.1 in appendix B lists the characteristics of existing wind turbines.

Table 2.1: Specifications of reference wind turbines

Type	Unit	IEA reference (2020) [29]	DTU reference (2013) [29, 30]
Power	$[MW]$	15	10
Hub height	$[m]$	150	119
Roter diameter	$[m]$	240	178.3
Blade length	$[m]$	117	86.3
Hub diameter	$[m]$	6	5.7
Power density	$[W/m^2]$	331.6	400.5
Blade tip speed	$[m/s]$	95	90
Blade root diameter	$[m]$	5.2	-
Blade mass	$[t]$	65	41
Rotor nacelle assembly mass	$[t]$	1,017	674
First flapwise natural frequency	$[Hz]$	0.555	-
First edgewise natural frequency	$[Hz]$	0.642	-

2.6. Components assessment

In this section, the impact of all components of an offshore wind turbine on blade installation is identified.

2.6.1. Support structure challenges

It is desirable to minimise the motions of a wind turbine during blade installation. The motion of the support structure, consisting of a monopile and a tower, is excited by wave and wind forces. The stiffness of the structure is determined by the diameter and wall thickness. It will be revealed later in this thesis that modifying the diameter in particular has an impact on the stiffness. Soil stiffness cannot be neglected, because it makes the turbine less stiff which results in different natural frequencies and possibly greater deflections. Mitigation of the turbine deflection can be applied by adding a tuned mass damper [31].

2.6.2. Nacelle challenges

A nacelle is a heavy top mass and counteracts mitigation. It is of importance to include the nacelle in the support structure model before analysing relative motions between support structure and blade, as it will likely affect the support structure motions negatively.

2.6.3. Blade challenges

Blade installation is the final phase of the wind turbine. It faces significant risks of impact and due to relative motions between blades and hub, delicate assemblies are submitted to high impact forces causing delays in the installation process of the wind turbine. Blade wind interaction is the prevalent cause of the blade movement. The cranes used to hoist the blade to hub height is located on a floating vessel. The crane motions should also be taken into account when analysing blade movements.

The installation process of a geared-drive and a direct-drive wind turbine are very different. When installing a single blade, with most techniques, the blade must be installed horizontally and not at an angle with the horizontal axis. This means that after one single blade is installed, the partially installed rotor needs to rotate. When geared-drive, the rotation can be achieved by the wind turbine drive train. But with direct-drive, a forced rotation of the rotor is required. The rotor could also be installed in one piece, a so called rotorstar installation.

2.7. Installation mitigation resources

This section elaborates on mitigations for excessive support structure or blade movements.

2.7.1. Installation vessel

During lift operations, wind and waves can destabilise the ship. Jack-up lift vessels are commonly used to install offshore wind turbines in shallow water. The vessel provides a stable working platform that emerges from the water with the help of jack-up legs supported by spudcans that anchor the legs in the ground. The demand for use of jack-up lift vessels keep increasing because of the exponentially growing offshore wind energy market, but with increasing water depths also come new challenges. As the jack-up vessels used for offshore wind energy reposition more frequent than jack-up platforms used for the oil and gas industry, the spudcans do not penetrate the soil very deep. As a result, the wind turbine installing jack-ups are more sensitive to wind and wave loads [32]. With increasing depth this problem will also worsen.

A jack-up vessel is a potential mitigation of blade motions, but it must be noted that for this thesis a floating installation vessel is used.

2.7.2. Cranes

Cranes are a proper means to compensate for movements of the lifted load. A very common way to counteract vertical wave motions is heave compensation. This is a system in which a winch moves proactively and fully automatically based on the vertical movement of the crane boom to keep the load in the same vertical position. The movement of this crane boom is a prognosis of the wave movements. Such an active system is limited to a maximum load and a maximum number of pulleys, respectively due to a maximum stress a winch can handle and the maximum length of cable that a winch can reel in, in a short period of time.

Figure 2.3: A Liebherr crawler installed on a barge master during testing [8].

Another new concept is the BM-T700 of the company Barge Master in figure 2.3[8]. This is a platform that compensates for the roll, pitch and heave motions of the crane attached on top of it with respect to the vessel. Combined with a dynamic positioning system of the ship, which is discussed further in section 2.7.6, 95% of the vessel movements could be mitigated and the workability of the operation increases significantly. The system was tested with a Liebherr crawler crane on top of it. This crane is able to reach a hoist height of 148 m with a maximum load capacity of 250 tonnes [33]. This would suffice for the offshore wind turbines which are currently being installed, but not for the scaled 20 MW wind turbine.

2.7.3. Blade yokes

To prevent the blade from rotating during a lift operation, a yoke has been added which grabs the blade around its center of mass. The LT975 Blade Dragon in figure 2.4a and the Boom Lock technology in figure 2.4b are examples of blade lifting yokes. The former is a remote-controlled lifting yoke for rotor assembly and disassembly. It can install blades at all angles compared to the horizontal axis, which is convenient when installing a direct-drive wind turbine that can not rotate by its own during installation. Direct-drive means that no gearbox is present in the wind turbine. The Blade Dragon has a single point that can rotate in the vertical plane and for that reason it can operate in wind velocities up to 18 m/s [34]. This is a condition in which wind turbine contractors do not currently operate. The latter of the two lifting yokes is also operable in a condition that contractors do not operate, namely a wind velocity of 15 m/s. With the Boom Lock technology, a wind turbine blade can rotate in the horizontal plane and can only be installed in a horizontal position [35].

(a) The Blade Dragon is a remote-controlled lifting yoke for rotor assembly and disassembly under an optional angle [34].

(b) The Boom Lock consists of a trolly, mounted at a conventional crane that grabs the hoisting block of the rotor blade in horizontal position [36]

Figure 2.4: Lifting yoke concepts

The blade yokes have a mass that needs to be included when modelling the wind turbine blade suspended from a crane. This mass is usually a factor two of the blade mass, for the sole purpose of counteracting the wind forces [37].

2.7.4. Taglines

Taglines are used to reduce motions of the blades [38]. They are mounted to the blade ends to mitigate any pendulum or yaw motion of the blade. The taglines can be seen in both subfigures of figure 2.4. Typically, the entire process is done without active tagline force control, but that is something that is being tested in different researches [39].

2.7.5. Tuned mass damper

An aforementioned tuned mass damper could be added to a support structure as additional damping. A tuned mass damper is one of the oldest structural vibration control devices. A number of tall buildings, particularly in Japan, are now equipped with such a system for vibration mitigation under wind and moderate earthquakes [40]. The addition of a tuned mass damper in an offshore wind turbine is already investigated and will be used as a mitigation opportunity in this research [41].

2.7.6. Dynamic positioning

The founders of the first dynamic positioning (DP) systems were companies, research institutes and universities from Norway, encouraged by the discovery of oil and gas off the coast of Norway. A dynamically positioned vessel automatically keeps its position exclusively by using active propellers and thrusters, with no anchoring involved and thereby counteracting environmental forces and moments from wind, waves and current [42]. DP operates in that it can control three horizontal degrees of freedom, namely surge, sway and yaw. The first two are translational motions and the latter is a rotational motion.

3

Model Setup

Before the general installation process of an offshore wind turbine can begin, a preliminary assessment of the installation site should be done. Firstly, the preliminary assessment is addressed in this chapter. Secondly, a scaling assessment resulting in a 20 MW turbine is completed. Lastly, the configurations of installing a wind turbine blade used in this research are interpreted.

3.1. Metocean data analysis

Metocean data is site-specific environmental data, a combination of meteorology and oceanography data. Critical metocean parameters are significant wave height and spectral peak period, among others. Methods to properly display the processed metocean data are wind roses, scatter diagrams, line charts and extreme tables. Several of such methods are displayed in this chapter and some will be discussed in appendix C. Since measurements of metocean data is done relatively short and often 50-year return periods are needed, extrapolation of this data is necessary.

3.1.1. Waves

Data about waves is oceanography data. Waves can occur as wind waves or swell waves. Wind waves are everywhere and constantly generated by the wind in the higher frequency range of non-extreme waves. A swell is a group of waves with a longer peak period and is therefore in the lower frequency range. These swell waves are generated in storms that occur in the North Sea, often off the coast of Norway. Figure 3.1 depicts a first clear picture of wave behaviour at a certain location over a period from 1979 to 2016, every season of the year. Figure 3.1a illustrates the significant wave height and figure 3.1b illustrates the spectral peak period. The orientation in figure 3.1 is the direction the waves come from, not where the waves are headed. In this case, the measurement location is at a coordinate somewhere in the designated wind farm area Nederwiek and the waves come from the North, somewhere off the coast of Norway. Motions of the waves translate in motions of the structure and vessel and tend to make the offshore operations more difficult.

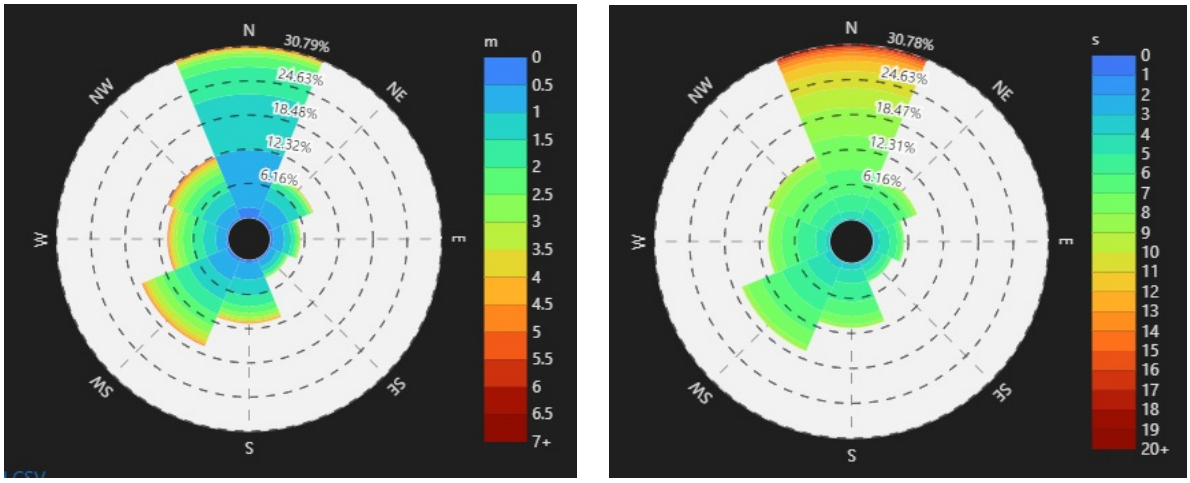

(a) Significant wave height in mean direction of spectral peak [12].

(b) Relative peak period in mean direction of spectral peak [12].

Figure 3.1: Wave statistics of coordinates located in new Dutch wind farm Nederwiek.

3.1.2. JONSWAP spectrum

Ocean waves are generated by wind. The longer the wind blows, the quicker it blows, and the larger the area it covers, the larger the waves get. An empirical relationship that describes the energy distribution of the waves with frequency in the ocean is the JONSWAP (Joint North Sea Wave Project) spectrum. This empirical relationship is displayed in equation 3.1. In essence, the JONSWAP spectrum is a fetch-limited variation of the Pierson-Moskowitz spectrum, with the exception that the wave spectrum is never entirely developed and may continue to evolve for a very long time due to non-linear wave-wave interactions. As a result, in the JONSWAP spectrum, waves continue to develop with time or distance as indicated by α, while γ specifies that the peak in the spectrum is more apparent. The significant wave height H_s and spectral peak period T_p are important variables in determining the JONSWAP spectrum and are dependent on one another. This dependence is elaborated in appendix C through equation C.2.

$$S_\zeta = \frac{320 H_s^2}{T_p^4 \omega^5} exp^{\frac{-1950}{T_p^4 \omega^4}} \gamma^A$$
$$A = exp^{-\left(\frac{\frac{\omega}{\omega_p}-1}{\sigma\sqrt{2}}\right)^2} \tag{3.1}$$

Equation 3.1 describes energy per frequency, with frequency in rad/s as the input. The result is plotted in figure 3.2. This result was determined by assuming a calm sea-state. The calm sea-state will eventually be used as input for the support structure multi-body system. The results of a normal and rougher sea-state are presented in appendix C.

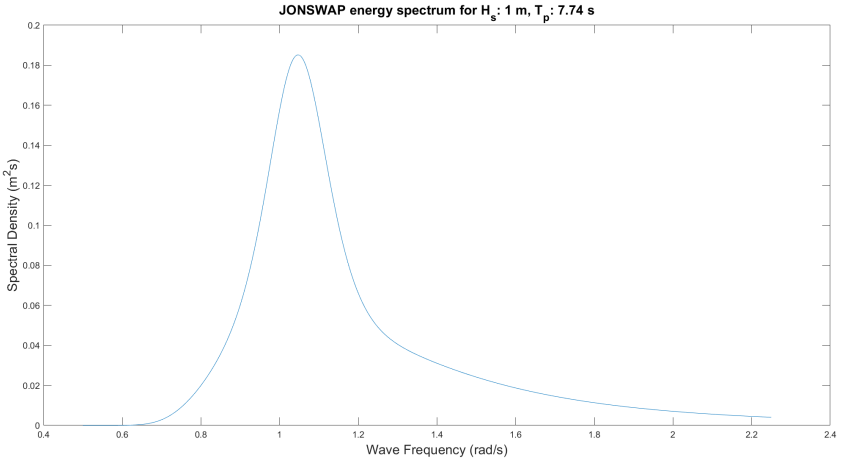

Figure 3.2: JONSWAP spectrum for normal sea-state, $H_s = 1$ m and $T_p = 6$ s

3.1.3. Wind

The blade installation process that is being discussed in this research, is usually limited to a mean wind velocity of 8 to 12 m/s [39, 43]. A mean wind velocity is measured in a 10-minute interval at a height of 10 m. Wind roses of both designated wind farm locations discussed in this chapter can be seen in figure 3.3. These give a first impression of the strength and direction of the wind, as figure 3.1 does for the waves. Hub heights of wind turbines reach over 100 m, thus wind velocities need to be scaled to higher altitudes. The measurements rendered in figure 3.3 are conducted at locations approximately 200 km distant from each other, but it can be observed that both wind roses are very much alike.

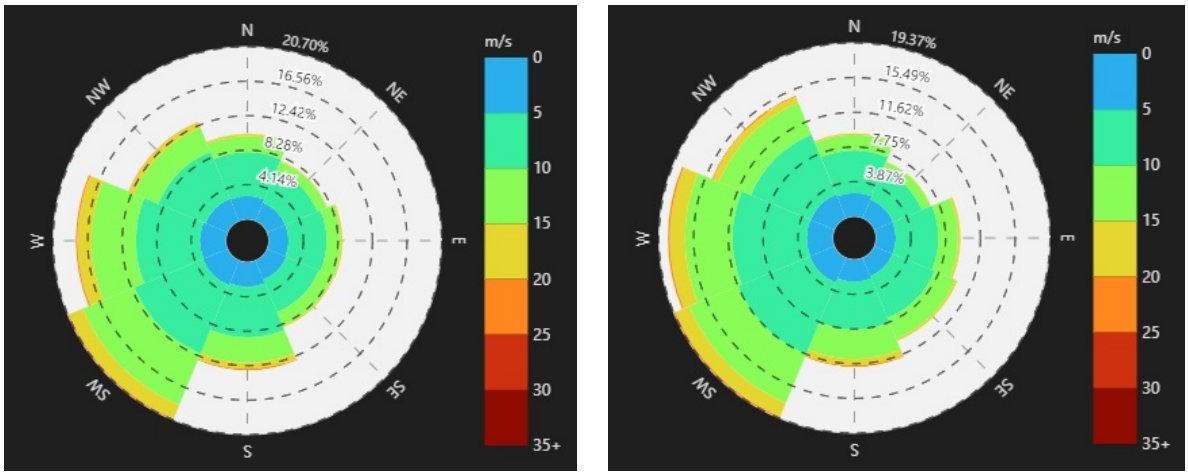

(a) Wind velocity in wind direction from the Nederwiek location [12].

(b) Wind velocity in wind direction from the Doordewind location [12].

Figure 3.3: Wind statistics of two locations.

3.1.4. Wind velocity scaling

Measured mean and maximum wind velocities are recorded at a standard height of 10 m. There are two common profiles to scale a known wind velocity. The profiles are depicted in equation 3.2 and 3.3, respectively the logarithmic profile and the power law profile [44]. The logarithmic profile is used when scaling from a reference height of 10 m to heights up to 100 m. If the hub height is above 100 m, the power law profile is applied, with a new reference height of 100 m and a scaled wind velocity at that height. α_0 is 0.11 over open water and z_0 is 0.0002 m at sea [45]. Both scale profiles are used in this thesis.

$$U(h) = U(h_{ref}) * \frac{ln(\frac{h}{z_0})}{ln(\frac{h_{ref}}{z_0})}, \qquad h < 100m \tag{3.2}$$

$$U(h) = U(h_{ref}) * (\frac{h}{h_{ref}})_0^{\alpha}, \qquad h > 100m \tag{3.3}$$

Appendix C describes in detail the importance of wind velocity forecast. The appendix elaborates on the measured and scaled wind velocities at coordinates located in Nederwiek and Doordewind, whereafter an estimation of the workability in those areas is done.

3.2. Scaling assessment: Zephyros

The future of wind energy remains assured. Where other energy sources are being phased out, power generation through wind turbines is growing and increasing dimensions of wind turbines is a consequence of this. 14 MW turbines are already scheduled to be commissioned and eventually an offshore wind turbine could reach a rated power of 15 MW [28, 46, 47]. The purpose of this scaling assessment is to determine dimensions of the future concept, a 20 MW wind turbine, which is given the name Zephyros in this thesis. Zephyros is Greek for westerly wind, this wind characterises the wind in the North Sea. There are several references available on a scaled 20 MW wind turbine, but the results are very divergent, so the decision was made to do a separate scaling assessment in this research [48, 49]. Additionally, not all characteristics needed for this research were included in the prior scaling assessments. In this chapter, the used methods of scaling are clarified, using the properties of tables 2.1 and B.1 as a baseline. The most important dimensions of the scaled 20 MW wind turbine are listed at the end of this chapter in table 3.1, together with dimensions obtained from a scaling assessment conducted in a different research. This research focused on a 20 MW offshore floating wind turbine with a spar buoy as support structure. For the purpose of this research it is not necessary to scale all dimensions of a wind turbine.

Firstly, the scaling scaling assessment begins with the rotor dimensions. Secondly, the lengths of the support structure are determined and lastly the blade characteristics are defined.

3.2.1. Rotor

The scaling of the rotor starts with calculating the power density of the various wind turbine models denoted in chapter 2. Tables 2.1 and B.1, respectively the reference turbines and the actual turbines, include this power density with W/m^2 as unit. It is noticeable that the 10 MW turbine of DTU (reference) is an outlier and has therefore been left out of consideration for further calculations. The power density of the remaining wind turbines is averaged and this resulted in a power density of 350.9 W/m^2 for the 20 MW concept. With the help of equation 3.4, a rotor diameter of 269.4 m was determined. It is assumed that the power density of Zephyros could become greater than power densities of any existing turbine, as the 20 MW turbine will reach higher than ever before, with higher wind velocities as a result. The power output scales proportionally with the wind velocity cubed. Therefore, the power output might increase after testing the first operational turbine.

$$Power\ density = \frac{Rated\ power}{Rotor\ area} = \frac{P}{\frac{1}{4} * \pi * D_{rotor}^2} \tag{3.4}$$

The rotor consists of a hub and three blades. The hub diameter is assumed to be 6.4 m, as most wind turbines in this report have a hub diameter of 6 m and all dimensions, including the hub, will become larger in the case of the 20 MW turbine. The hub should not be made too large since a larger hub also reduces the overall efficiency of the wind turbine. As this is an undisclosed trade-off, an assumption had to be made [37]. The next dimension that could be calculated due to this assumption is the blade length. With the help of equation 3.5, the blade length is determined to be 131.5 m.

$$Blade\ length = \frac{D_{rotor} - D_{hub}}{2} \tag{3.5}$$

3.2.2. Monopile and tower

A monopile and tower connected by a transition piece create the support structure. The tower reaches up to the hub height. To define the hub height for the 20 MW offshore wind turbine equation 3.6 was used [37]. This results in a hub height of 154.7 m. Figure 3.4 implies the meaning of the rotor diameter and the hub height. Additional important dimensions of the support structure are the cross-sectional diameters. According to an expert of SIF Offshore, monopiles functioning as a foundation of a 20 MW offshore wind turbine will have a diameter of 11 m [19]. The tower has a tapered shape narrowing from 11 m at mean sea level to 6.5 m at hub height. The tower is not modelled as a tapered shape in this thesis. Chapter 4 elaborates on the modelling approach of tower. The hub height is further used in this report to assess wind velocities at that specific altitude. The wind velocities at hub height are important, as blades are hoisted to at least this elevation. Drag and lift forces that affect the motions of the blade during installation depend on this velocity to the power two, but are often measured at a standard altitude of 10 m. A scaling assessment to hub height is done in appendix C.2 as an example.

$$H_{hub} = \frac{D_{rotor}}{2} + 20 \tag{3.6}$$

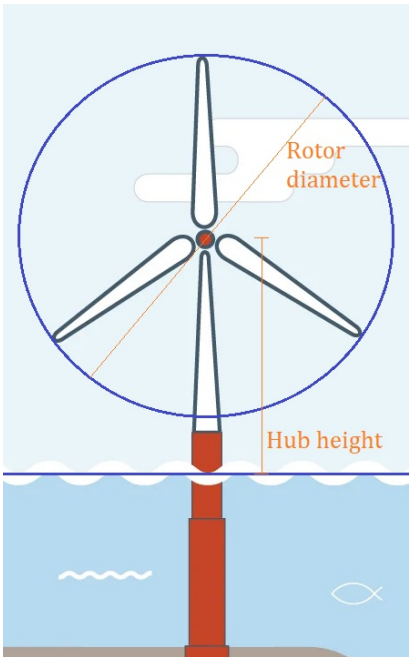

Figure 3.4: Schematic overview of typical dimensions wind turbine.

Figure 3.5: Blade installation by a jack-up lift vessel.

The blade yoke or gripper used for keeping the blade in position during blade installation is not included in the dimensions, but it will be modelled as extra weight at the center of gravity of the blade.

The crane clearance, the distance between the crane tip and the hoisted weight, is an important parameter of a dynamic pendulum system. If a load is hoisted, the operation acts like a pendulum. A simple undamped pendulum has a natural frequency as depicted in equation 3.7 having L representing the crane clearance with an inversely proportional relation [50] to the natural frequency. A small value of L and a large natural frequency could cause rapid motions of the blade. It is assumed that the distance between crane boom tip and center of gravity of the blade is at least 10 meters [37].

$$\omega_n = \sqrt{\frac{g}{L_{cable}}} \tag{3.7}$$

A single blade installation in horizontal position similar to figure 3.5 is considered and the lifting height is equal to the hub height of the wind turbine. This concludes to a minimal crane tip height of 164.7 m.

3.2.3. Nacelle

The nacelles of the existing and reference wind turbines are scaled up with the scale factor determined in equation 3.8 to achieve a weight of 1000 metric tons for the nacelle and hub collectively.

3.2.4. Blade design

In a following chapter, forces that act on a wind turbine blade will be calculated. A calculation of Zephyros' blade dimensions is conducted in this section. To be able to do this calculation, the necessary dimensions should be determined. During modelling the wind turbine blade is extremely simplified with no aerodynamic profile. Only the length and an approached surface is used in the model.

The blade is of the same type as the 15 MW reference turbine of IEA, namely the FFA-W3 aerofoil series as stated in section 2.5. The blade length was already scaled from 117 m to 131.5 m in this chapter.

The blade chord is an important parameter of the blade, especially because it has high impact on the center of gravity of the blade and hence is an important part of the dynamic system.

$$Scale\ factor: \quad \lambda_{Zephyros} = \frac{131.5}{117} = 1.124 \tag{3.8}$$

The max blade chord length and the blade root diameter are two dimensions that are scaled with $\lambda_{Zephyros}$ by multiplying the dimensions of the reference turbine with the scale factor. It results in a max blade chord length of 6.49 m and a blade root diameter of 5.84 m.

Hereafter we look at the shape of the blade to determine at which span position the max chord is located. This is done with the Reynolds number, which is formulated in equation 3.9. The Reynolds number is chosen because the ratio inertial forces over viscous forces stay the same, which is a feature of the Reynolds number. This ratio should be maintained the same to be allowed to apply Reynolds scaling.

$$Re = \frac{U * L * \rho}{\mu} = \frac{U * L}{\nu} \tag{3.9}$$

$$U_1 * L_{c,1} = U_2 * L_{c,2} \tag{3.10}$$

The density ρ and the dynamic viscosity μ of the fluid stay the same. Equation 3.9 will be simplified to equation 3.10, with U_1 being the velocity at max chord position of the 15 MW turbine, $L_{c,1}$ the maximum chord length of the 15 MW turbine, U_2 the velocity at max chord position of Zephyros and $L_{c,2}$ the maximum chord length of Zephyros.

$$U = \omega * r \tag{3.11}$$

In equation 3.11, U refers to both velocities mentioned above, ω is the angular velocity of any wind turbine blade and r is the distance in radial direction to any span position from the blade root, in this case the max chord length position.

As U_1, $L_{c,1}$, $L_{c,2}$ and ω_2 can be easily calculated, the equations give a max chord span position of 26.94 m. This is a shorter distance from the blade root compared with the 15 MW turbine, which is 27.2 m. The assumption is done that this is highly unlikely and that the max chord length should be at a greater distance from the blade root compared with the 15 MW turbine. If both blades widen by the same angle until max chord is reached (labeled with 3), starting at the point at which the blade is no longer cylindrical (labeled with 1), it can be determined that the max chord length span position is at 32.5 m from the blade root. The Reynolds number of this newly determined transverse section is still in the same order of magnitude, which confirms that similar cross sections of different blade sizes behave the same in aerodynamic flow.

The rotor frequency (1P) and the blade passing frequency are also calculated with equation 3.11. The maximum blade tip velocity and rotor diameter are used to determine the maximum angular velocity of the rotor (1P). The maximum blade tip velocity is 85 m/s and the length is the rotor diameter divided by two. The rotor itself passes the tower every rotation, thus 1P. The rotor consists of three blade and every rotation, the tower is passed by three blades, thus 3P. The frequency of 3P is three times 1P. The values are listed in table 3.1. The frequencies are on the low side compared to the usual values [51, 52]. The 1P frequency is very close to the peak frequencies of common sea-states. The solution is to either allow a higher tip velocity or decrease the maximum value. When changing the rotor and blade passing frequency, the first tower resonance frequency has to be taken into account. This frequency is calculated in the next chapter.

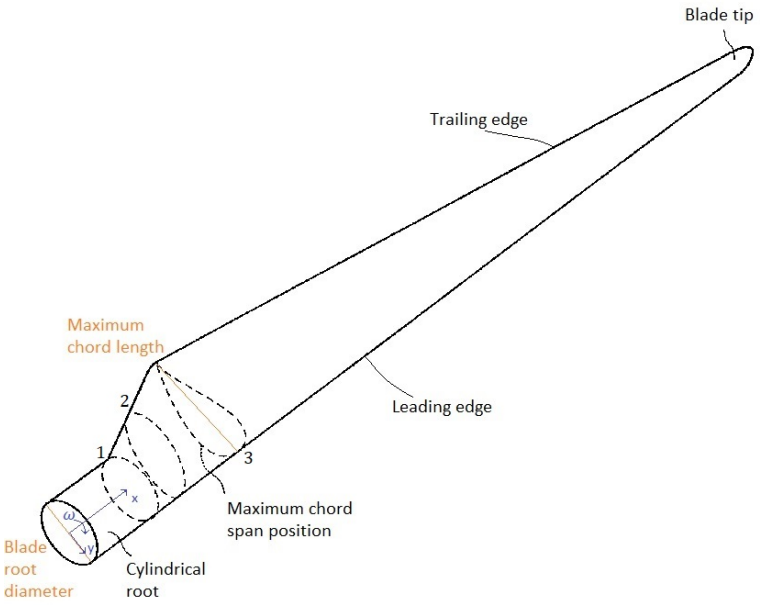

Figure 3.6: Blade characteristics as additional support for the scaling described in the text.

3.2.5. List of scaled dimensions: Zephyros

This sections lists all the dimensions of the scaled 20 MW wind turbine Zephyros and some of the known characteristics of a 20 MW wind turbine that were obtained through a scaling assessment in a different paper, which discussed a floating wind turbines (FWT) with a geared-drive generator.

Table 3.1: Determined dimensions of extrapolated 20 MW wind turbine, Zephyros.

Parameter	Unit	Zephyros	FWT [49]
Rated power	MW	20	20
Rotor diameter	m	269.4	276.0
Power density	W/m^2	350.9	334.3
Hub height	m	154.7	160.2
Hub diameter	m	6.4	-
Blade length	m	131.5	-
Maximum chord length	m	6.49	-
Maximum chord span position	m	32.5	-
Blade root diameter	m	5.84	-
Nacelle + hub mass	$tonnes$	1000	1198
1P	Hz	0.10	-
3P	Hz	0.30	-

3.3. Model configurations

In this section, the configuration of the relative behaviour between the wind turbine support structure and blade in a 3D model during the third-to-last part of the installation phase of a blade is described. The positioning of the blade, before mating and boltening the blade to the hub.

The relative motions of the support structure and blade are modelled resembling figure 3.7. This figure shows the $z-x$ plane of the 3D model. The green component is the nacelle, with attached hub, supported by the grey wind turbine bottom founded support structure. The wind turbine blade is the horizontal grey beam and is suspended from a crane. The blade is installed in a horizontal position, which means that the chord line is in a horizontal position, see figure 2.2 for an illustration of the chord line. The installation vessel is a floating vessel, leading to the assumption that the crane boom tip is in motion during the installation phase.

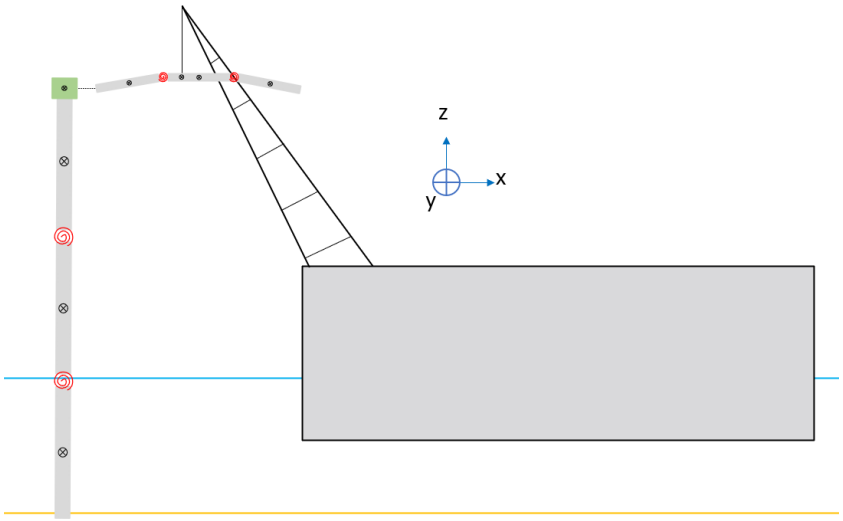

Figure 3.7: Blade installation with floating vessel overview in the $z-x$ plane.

3.3.1. Forces

The forces exerted on the wind turbine support structure and blade are displayed below in a top view of the model in figure 3.8. The wave, current and wind force act independently on the wind turbine support structure, but are displayed together with the bolt arrow. The decomposition of this force is shown in figures 3.9 and 3.10. Various angles can be distinguished in figure 3.8, all relative to the x-axis. The wave force, current force and wind force can be adjusted in direction independently. The wave force is accompanied with the angle β_1, the current force with β_2 and the wind force with β_3.

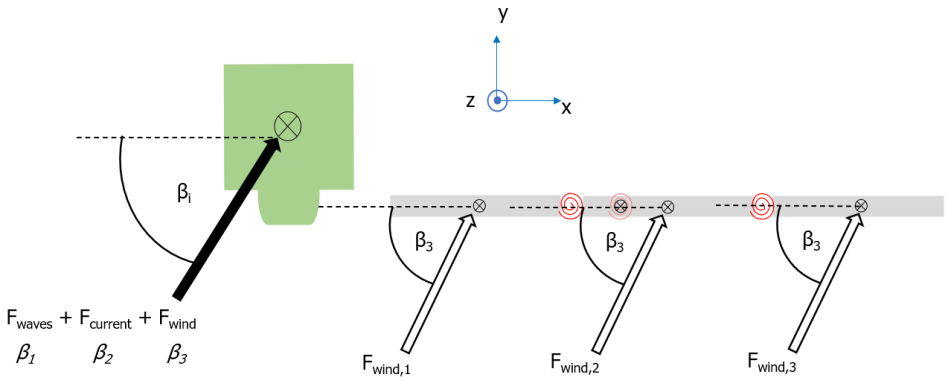

Figure 3.8: All forces acting on wind turbine support structure and blade.

3.3.2. Model configurations with forces

As mentioned above, the angle of any force is relative to the x-axis. At an angle of zero degrees, an illustration of the model in the $z-x$ plane will resemble figure 3.9.

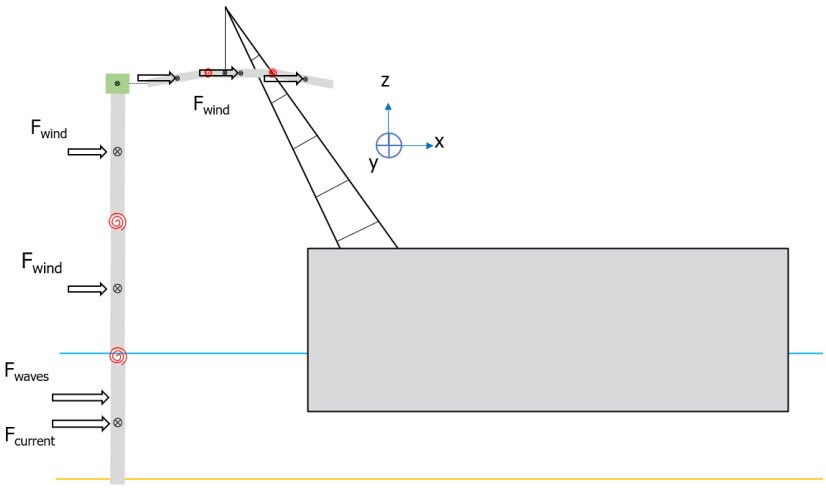

Figure 3.9: Blade installation overview in the $z-x$ plane including forces.

At an angle of 90 degrees, an illustration of the model in the $z-x$ plane will resemble figure 3.10.

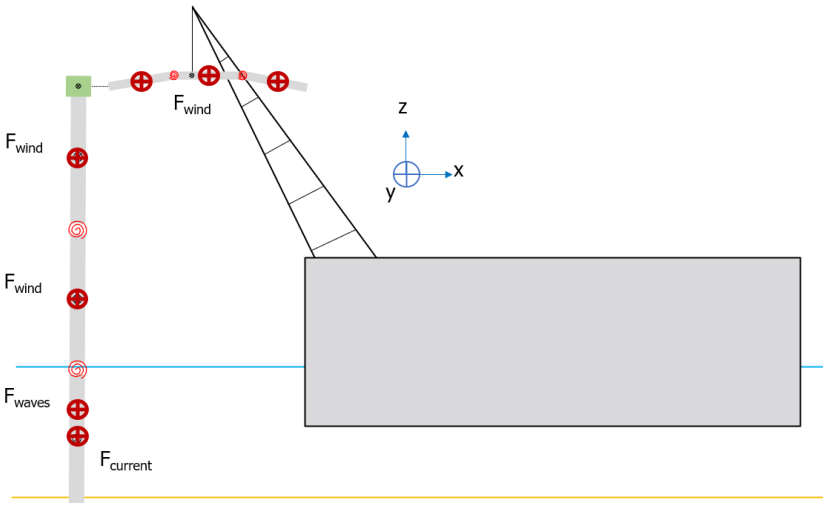

Figure 3.10: Blade installation overview in the $z-x$ plane including forces.

The two situations described above are solely for illustration purpose. The simulations conducted in this report are carried out with different force angle scenarios. The next two chapters will elaborate extensively on the wind turbine support structure and blade models.

4

Support structure dynamic modelling

The problem introduced in this thesis is solved by analysing the support structure with nacelle and hub separately from the blade. In this thesis, the support structure, nacelle and hub together will be referred to as just the support structure. Firstly, this chapter elaborates on the Lagrangian method. Secondly, the model layout that describes the support structure is explained. Lastly, a sensitivity analysis of several parameters of the support structure, and therefore also the nacelle and hub, is conducted.

4.1. The Lagrangian Method

Lagrangian mechanics are more general and easier to apply when dealing with complex systems under limitations, which can be very messy or difficult to work with when using Newtonian mechanics. In this case, it is considerably easier to apply the Lagrangian method.

Lagrangian mechanics is based on the stationary-action principle, also known as the principle of least action. It is a method for generating equations of motions, which normally cannot be easily determined. It has the potential to describe the structural response of a beam more accurate by dividing it into segments. Segments are often called particles and in this chapter the segments represent an inverted N-link pendulum, in which N is the number of segments. The number of degrees of freedom of the bar will result in the same amount of mode shapes. Mode shapes of low-order mathematical expression tend to provide the greatest contribution to structural response. As orders increase, mode shapes contribute less, and are predicted less reliably. But it is nevertheless preferable to divide the beam into more than one segment [53].

A degree of freedom is accompanied by one equation of motion. With problems involving more than one variable, it usually turns out to be much easier to write down the kinetic and potential energy, as opposed to writing down all the forces when using Newtonian mechanics.

The central quantity of Lagrangian mechanics is the Lagrangian in equation 4.1 which is made up of kinetic energy T and potential energy V. The principle of energy conservation states that energy is neither created nor destroyed [54]. The continuation of Lagrangian mechanics in equation 4.2 describes this principle of energy conservation as no external forces are present. The result from equation 4.2 is an equation of motion.

$$L = T - V \tag{4.1}$$

$$\frac{d}{dt}\left(\frac{\partial L}{\partial \dot{q}_j}\right) = \frac{\partial L}{\partial q_j} \tag{4.2}$$

The variables q_j and $\dot{q}_j$ are scalars which denote the position or velocity of any particle. In this particular research, an extension of equation 4.2 is used.

To be able to generate the Lagrangian in equation 4.1, the kinetic and potential energies of the system have to be determined. In this assessment, the kinetic energy takes on the formulation of equation 4.3 and the potential energy appears as in equation 4.4. The two potential energies that are

going to be used in this thesis are the gravitational and elastic energy. Other well known potential energies are gravitational energy between two bodies, electrostatic energy and magnetic energy. The two types of kinetic energy that are going to be used are the energies due to translational and rotational inertia of a segment.

$$T = \frac{1}{2} m v^2 \qquad T = \frac{1}{2} I \dot{\omega}^2 \tag{4.3}$$

$$V = m g h \qquad V = \frac{1}{2} k u^2 \tag{4.4}$$

In equation 4.5, non-conservative forces are included as R and the excitation as W, which is the work done by the forces acting on any segment in the model. Non-conservative forces involve dissipation due to material characteristics [55].

$$\frac{d}{dt}\left(\frac{\partial L}{\partial \dot{q}_j}\right) - \frac{\partial L}{\partial q_j} + \frac{\partial R}{\partial \dot{q}_j} = \frac{\partial W}{\partial q_j} \tag{4.5}$$

The Rayleigh dissipation function R in equation 4.5 can be determined with equation 4.6. B_{ij} is a matrix with $n\,x\,n$ entries and $\dot{\theta}_i$ is the derivative of n degrees of freedom.

$$R = \frac{1}{2} \sum \dot{\theta}_i B_{ij} \dot{\theta}_i^T \tag{4.6}$$

To derive the energies above that result in the Lagrangian and eventually an equation of motion, first, generalised coordinates should be established. Equation 4.7 is implemented. Note: the coordinate system used in this section is different from the coordinate system used in section D. The new coordinate system is depicted in figure 4.1.

4.2. Assumptions

The dynamic model is conditioned by a number of assumptions, apart from using Lagrangian mechanics. The assumptions are listed below and will be discussed in more detail in section 4.5.

1. The support structure is modelled in $3D$.
2. The small angle approximation is applied, up to 2^{nd}-order Taylor polynomial expansions of sine en cosine.
3. The segments are modelled as rigid uniform beams.
4. Torsion of the cylindrical support structure is not taken into account.
5. Bending stiffness of beam is modelled as rotational spring at the bottom of a segment.
6. Soil stiffness correction factor is included to model soil stiffness.
7. Nacelle is modelled as a point mass.
8. The support structure is excited by unidirectional waves, current and wind forces which act separately, modelled with the Morison equation.
9. Aerodynamic and hydrodynamic damping is included by taking the velocity of the support structure relative to the waves and wind.
10. Material damping is introduced as modal damping.

4.3. Model introduction

Assumption two states that the small angle approximation is used. The small-angle approximation provides an approximation for the trigonometric functions if the angle is small and measured in radians. If the Taylor expansion of the sine and cosine up to the 2^{nd}-order polynomial is taken into account, the small-angle approximation results in equation 4.7. Equation 4.8 provides a value not to be exceeded, which results in an angle of approximately 0.2 radians for the small angle approximation to be valid.

$$cos(\theta) \approx 1 - \frac{\theta^2}{2} \qquad (4.7)$$
$$sin(\theta) \approx \theta$$

$$cos(0.2) = 0.980 \approx 1 - \frac{0.2^2}{2} \qquad (4.8)$$
$$sin(0.2) = 0.199 \approx 0.2$$

The generalised coordinates are defined to allow a minimum number of dependent coordinates being used to describe a system. The degrees of freedom q_j in this system, with j representing $1 \dots 6$, are $\theta_1 \dots \theta_6$. The x_i and z_i coordinates in equations 4.9, 4.10 and 4.11 act at the centre of gravity of each member with character i being 1...6 or t for the top mass and are expressed in terms of degrees of freedom and other parameters. The positions are with respect to the origin of the coordinate system.

Figure 4.1 is a representation of the $z - x$ plane. The wind turbine support structure can be represented with the same parameters, but different degrees of freedom, to create the $z - y$ plane. Apart from the z-coordinate, both planes are uncoupled, due to the uncoupled degrees of freedom of the planes. Figure 4.2 supports to illustrate the degrees of freedom of a single segment, of which there exist three in the multi-body system. These translations and rotations are generated by $\theta_1 \dots \theta_6$.

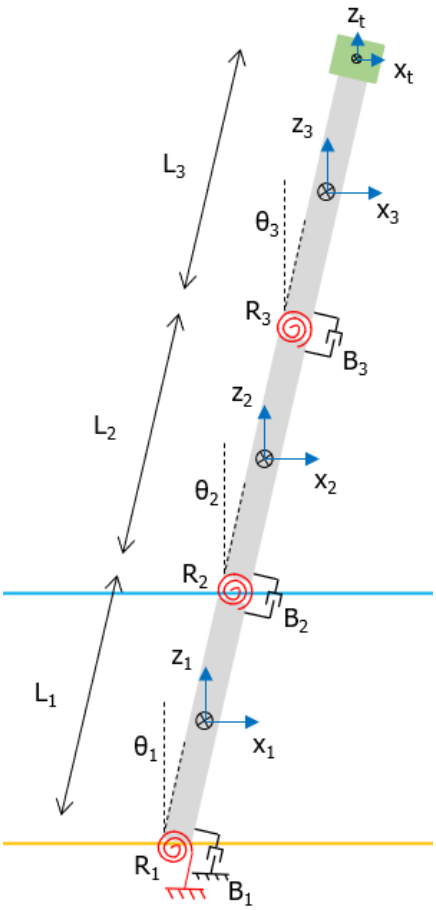

Figure 4.1: Schematic wind turbine model.

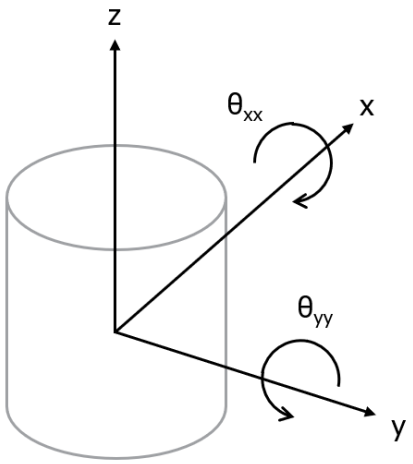

Figure 4.2: Degrees of freedom of a support structure segment.

$$\begin{aligned} x_1 &= \frac{L_1}{2}\theta_1 \\ x_2 &= L_1\theta_1 + \frac{L_2}{2}\theta_2 \\ x_3 &= L_1\theta_1 + L_2\theta_2 + \frac{L_3}{2}\theta_3 \\ x_t &= L_1\theta_1 + L_2\theta_2 + L_3\theta_3 \end{aligned} \tag{4.9}$$

$$\begin{aligned} y_1 &= \frac{L_1}{2}\theta_4 \\ y_2 &= L_1\theta_4 + \frac{L_2}{2}\theta_5 \\ y_3 &= L_1\theta_4 + L_2\theta_5 + \frac{L_3}{2}\theta_6 \\ y_t &= L_1\theta_4 + L_2\theta_5 + L_3\theta_6 \end{aligned} \tag{4.10}$$

$$\begin{aligned} z_1 &= \frac{L_1}{2}\left(1-\frac{\theta_1^2}{2}\right)\left(1-\frac{\theta_4^2}{2}\right) \\ z_2 &= L_1\left(1-\frac{\theta_1^2}{2}\right)\left(1-\frac{\theta_4^2}{2}\right) + \frac{L_2}{2}\left(1-\frac{\theta_2^2}{2}\right)\left(1-\frac{\theta_5^2}{2}\right) \\ z_3 &= L_1\left(1-\frac{\theta_1^2}{2}\right)\left(1-\frac{\theta_4^2}{2}\right) + L_2\left(1-\frac{\theta_2^2}{2}\right)\left(1-\frac{\theta_5^2}{2}\right) + \frac{L_3}{2}\left(1-\frac{\theta_3^2}{2}\right)\left(1-\frac{\theta_6^2}{2}\right) \\ z_t &= L_1\left(1-\frac{\theta_1^2}{2}\right)\left(1-\frac{\theta_4^2}{2}\right) + L_2\left(1-\frac{\theta_2^2}{2}\right)\left(1-\frac{\theta_5^2}{2}\right) + L_3\left(1-\frac{\theta_3^2}{2}\right)\left(1-\frac{\theta_6^2}{2}\right) \end{aligned} \tag{4.11}$$

To be able to create the kinetic energy and dissipation, velocities are compiled. The velocities in equations 4.12, 4.13 and 4.14 are obtained by taking the time derivative of the generalised coordinates in equations 4.9, 4.10 and 4.11. The velocities use the same point of action as the coordinates, the centers of gravity of the segments.

$$\begin{aligned} \dot{x}_1 &= \frac{L_1}{2}\dot{\theta}_1 \\ \dot{x}_2 &= L_1\dot{\theta}_1 + \frac{L_2}{2}\dot{\theta}_2 \\ \dot{x}_3 &= L_1\dot{\theta}_1 + L_2\dot{\theta}_2 + \frac{L_3}{2}\dot{\theta}_3 \\ \dot{x}_t &= L_1\dot{\theta}_1 + L_2\dot{\theta}_2 + L_3\dot{\theta}_3 \end{aligned} \tag{4.12}$$

$$\begin{aligned} \dot{y}_1 &= \frac{L_1}{2}\dot{\theta}_4 \\ \dot{y}_2 &= L_1\dot{\theta}_4 + \frac{L_2}{2}\dot{\theta}_5 \\ \dot{y}_3 &= L_1\dot{\theta}_4 + L_2\dot{\theta}_5 + \frac{L_3}{2}\dot{\theta}_6 \\ \dot{y}_t &= L_1\dot{\theta}_4 + L_2\dot{\theta}_5 + L_3\dot{\theta}_6 \end{aligned} \tag{4.13}$$

$$\begin{aligned} \dot{z}_1 &= \frac{L_1}{2}(\dot{\theta}_1\theta_1 + \dot{\theta}_4\theta_4) \\ \dot{z}_2 &= L_1(\dot{\theta}_1\theta_1 + \dot{\theta}_4\theta_4) + \frac{L_2}{2}(\dot{\theta}_2\theta_2 + \dot{\theta}_5\theta_5) \\ \dot{z}_3 &= L_1(\dot{\theta}_1\theta_1 + \dot{\theta}_4\theta_4) + L_2(\dot{\theta}_2\theta_2 + \dot{\theta}_5\theta_5) + \frac{L_3}{2}(\dot{\theta}_3\theta_3 + \dot{\theta}_6\theta_6) \\ \dot{z}_t &= L_1(\dot{\theta}_1\theta_1 + \dot{\theta}_4\theta_4) + L_2(\dot{\theta}_2\theta_2 + \dot{\theta}_5\theta_5) + L_3(\dot{\theta}_3\theta_3 + \dot{\theta}_6\theta_6) \end{aligned} \tag{4.14}$$

Subsequent, the kinetic and potential energy and work of the forces are composed. The kinetic energy of every member consists of a translational inertia component of the segment at the center of gravity and a rotational inertia component of a segment around its center of gravity. The nacelle is modelled as a point mass and therefore has a translational component only. The translational and rotational components of every segment in both the x-direction and y-direction are depicted relatively in green and blue in equation 4.15. The potential energy contains gravitational and torsional spring energy, with the former in red and the latter in black. It is reported that the equivalent rotational stiffness of the segments are equal in the $z-x$ and $z-y$ plane due to the cylindrical shape of the support structure.

$$
\begin{aligned}
T = {} & \frac{1}{2}M_1\begin{pmatrix}\dot{x}_1\\ \dot{z}_1\end{pmatrix}\bullet\begin{pmatrix}\dot{x}_1\\ \dot{z}_1\end{pmatrix} + \frac{1}{2}I_1\dot{\theta}_1^2 + \frac{1}{2}M_2\begin{pmatrix}\dot{x}_2\\ \dot{z}_2\end{pmatrix}\bullet\begin{pmatrix}\dot{x}_2\\ \dot{z}_2\end{pmatrix} + \frac{1}{2}I_2\dot{\theta}_2^2 \\
& + \frac{1}{2}M_3\begin{pmatrix}\dot{x}_3\\ \dot{z}_3\end{pmatrix}\bullet\begin{pmatrix}\dot{x}_3\\ \dot{z}_3\end{pmatrix} + \frac{1}{2}I_3\dot{\theta}_3^2 + \frac{1}{2}M_t\begin{pmatrix}\dot{x}_t\\ \dot{z}_t\end{pmatrix}\bullet\begin{pmatrix}\dot{x}_t\\ \dot{z}_t\end{pmatrix} + \frac{1}{2}M_1\begin{pmatrix}\dot{y}_1\\ \dot{z}_1\end{pmatrix}\bullet\begin{pmatrix}\dot{y}_1\\ \dot{z}_1\end{pmatrix} + \frac{1}{2}I_1\dot{\theta}_4^2 \\
& + \frac{1}{2}M_2\begin{pmatrix}\dot{y}_2\\ \dot{z}_2\end{pmatrix}\bullet\begin{pmatrix}\dot{y}_2\\ \dot{z}_2\end{pmatrix} + \frac{1}{2}I_2\dot{\theta}_5^2 + \frac{1}{2}M_3\begin{pmatrix}\dot{y}_3\\ \dot{z}_3\end{pmatrix}\bullet\begin{pmatrix}\dot{y}_3\\ \dot{z}_3\end{pmatrix} + \frac{1}{2}I_3\dot{\theta}_6^2 + \frac{1}{2}M_t\begin{pmatrix}\dot{y}_t\\ \dot{z}_t\end{pmatrix}\bullet\begin{pmatrix}\dot{y}_t\\ \dot{z}_t\end{pmatrix}
\end{aligned}
\tag{4.15}
$$

$$
\begin{aligned}
V = {} & M_1 g z_1 + \frac{1}{2}R_1\theta_1^2 + \frac{1}{2}R_1\theta_4^2 + M_2 g z_2 + \frac{1}{2}R_2(\theta_2-\theta_1)^2 + \frac{1}{2}R_2(\theta_5-\theta_4)^2 + \\
& M_3 g z_3 + \frac{1}{2}R_3(\theta_3-\theta_2)^2 + \frac{1}{2}R_3(\theta_6-\theta_5)^2 + M_t g z_t
\end{aligned}
\tag{4.16}
$$

To prevent the equations of motion from becoming excessively long, all third-order variables or higher are omitted.

The right hand side of equation 4.5 is a partial derivative of work. The work is calculated by multiplying a force by the distance covered. As the current and wind forces calculated are uniform or almost uniform over the height of the beam, it is assumed that the point of leverage is at the centre of the distributed forces, the centers of gravity. Wave forces, by contrast, do not have their point of leverage at the centers of gravity. It is assumed that a wave force resembles a triangle, thus the point of leverage is at 2/3 of the total height or 4/3 times the height of the center of gravity of a segment.

$$
\begin{aligned}
W = {} & F_{current,drag}(t)\ cos(\beta_2)\ x_1 + F_{wave}(t)\ \frac{4}{3}\ cos(\beta_1)\ x_1 + F_{air,drag,1}(t)\ cos(\beta_3)\ x_2 \\
& + F_{air,drag,2}(t)\ cos(\beta_3)\ x_3 + F_{current,drag}(t)\ sin(\beta_2)\ y_1 + F_{wave}(t)\ \frac{4}{3}\ sin(\beta_1)\ y_1 \\
& + F_{air,drag,1}(t)\ sin(\beta_3)\ y_2 + F_{air,drag,2}(t)\ sin(\beta_3)\ y_3
\end{aligned}
\tag{4.17}
$$

The work depicted in equation 4.17 will result in moments after taking the partial derivatives. For example, the partial derivative of x_1 over θ_1 is $\frac{L_1}{2}$. This can be seen in matrix 4.25, in which the forces are multiplied by a length.

Damping is introduced. There are four types of damping present in this system. Hydrodynamic, aerodynamic, soil and structural damping. Hydrodynamic and aerodynamic damping is introduced by taking the velocity of the support structure relative to the waves, current and wind. The soil and material damping is introduced as modal damping that focuses. The damping is arbitrarily added with the Rayleigh dissipation function. Equation 4.18 is the damping in the support structure model.

$$
R = \frac{1}{2}\dot{\theta}\begin{bmatrix}
B_{11} & B_{12} & B_{13} & B_{14} & B_{15} & B_{16}\\
B_{21} & B_{22} & B_{23} & B_{24} & B_{25} & B_{26}\\
B_{31} & B_{32} & B_{33} & B_{34} & B_{35} & B_{36}\\
B_{41} & B_{42} & B_{43} & B_{44} & B_{45} & B_{46}\\
B_{51} & B_{52} & B_{53} & B_{54} & B_{55} & B_{56}\\
B_{61} & B_{62} & B_{63} & B_{64} & B_{65} & B_{66}
\end{bmatrix}\dot{\theta}^T
\tag{4.18}
$$

4.4. Equations of motion

After equations 4.15 and 4.16 are implemented into equation 4.1 and the resulting Lagrangian, equation 4.17 and equation 4.22 are substituted into equation 4.5, an ordinary differential equation is the outcome. If these differential equations are solved for the degrees of freedom θ_1, θ_2 and θ_3, coupled equations of motion, are resembled by equation 4.19 evolve.

$$
\vec{M}\ddot{\vec{\theta}}_j + \vec{B}\dot{\vec{\theta}}_j + \vec{K}\vec{\theta}_j = \vec{Moment}
\tag{4.19}
$$

The matrices in equations 4.20, 4.21, 4.22, 4.23, 4.24, 4.25, and 4.26 are the resulting matrices that are substituted in equation 4.19. The forcing terms in equation 4.25 will be discussed in more detail in section 4.7.

Matrices 4.20 and 4.21 include the mass moments of inertia I_j mentioned in equation 4.15. Equation 4.34 has already been incorporated into matrices 4.20 and 4.21. The water added mass is included in M_1.

The mass and stiffness matrices are too large to display properly and it was therefore chosen to split the two matrices in two, resulting in four matrices. The subscripts $1/2$ and $2/2$ mean respectively the left and right side of the original matrix.

$$\vec{M_{1/2}} = \begin{bmatrix} (L_1^2(M_1+3M_2+3M_3+3M_t))/3 & (L_1L_2(M_2+2M_3+2M_t))/2 & (L_1L_3(M_3+2M_t))/2 \\ (L_1L_2(M_2+2M_3+2M_t))/2 & (L_2^2(M_2+3M_3+3M_t))/3 & (L_2L_3(M_3+2M_t))/2 \\ (L_1L_3(M_3+2M_t))/2 & (L_2L_3(M_3+2M_t))/2 & (L_3^2(M_3+3M_t))/3 \\ 0 & 0 & 0 \\ 0 & 0 & 0 \\ 0 & 0 & 0 \end{bmatrix} \tag{4.20}$$

$$\vec{M_{2/2}} = \begin{bmatrix} 0 & 0 & 0 \\ 0 & 0 & 0 \\ 0 & 0 & 0 \\ (L_1^2(M_1+3M_2+3M_3+3M_t))/3 & (L_1L_2(M_2+2M_3+2M_t))/2 & (L_1L_3(M_3+2M_t))/2 \\ (L_1L_2(M_2+2M_3+2M_t))/2 & (L_2^2(M_2+3M_3+3M_t))/3 & (L_2L_3(M_3+2M_t))/2 \\ (L_1L_3(M_3+2M_t))/2 & (L_2L_3(M_3+2M_t))/2 & (L_3^2(M_3+3M_t))/3 \end{bmatrix} \tag{4.21}$$

$$\vec{B} = \begin{bmatrix} B_{11} & B_{12} & B_{13} & B_{14} & B_{15} & B_{16} \\ B_{21} & B_{22} & B_{23} & B_{24} & B_{25} & B_{26} \\ B_{31} & B_{32} & B_{33} & B_{34} & B_{35} & B_{36} \\ B_{41} & B_{42} & B_{43} & B_{44} & B_{45} & B_{46} \\ B_{51} & B_{52} & B_{53} & B_{54} & B_{55} & B_{56} \\ B_{61} & B_{62} & B_{63} & B_{64} & B_{65} & B_{66} \end{bmatrix} \tag{4.22}$$

$$\vec{K_{1/2}} = \begin{bmatrix} R_1+R_2-(\frac{M_1}{2}-M_2-M_3-M_t)L_1g & -R_2 & 0 \\ -R_2 & R_2+R_3-(\frac{M_2}{2}-M_3-M_t)L_2g & -R_3 \\ 0 & -R_3 & R_3-(\frac{M_3}{2}-M_t)L_3g \\ 0 & 0 & 0 \\ 0 & 0 & 0 \\ 0 & 0 & 0 \end{bmatrix} \tag{4.23}$$

$$\vec{K_{2/2}} = \begin{bmatrix} 0 & 0 & 0 \\ 0 & 0 & 0 \\ 0 & 0 & 0 \\ R_1+R_2-(\frac{M_1}{2}-M_2-M_3-M_t)L_1g & -R_2 & 0 \\ -R_2 & R_2+R_3-(\frac{M_2}{2}-M_3-M_t)L_2g & -R_3 \\ 0 & -R_3 & R_3-(\frac{M_3}{2}-M_t)L_3g \end{bmatrix} \tag{4.24}$$

The beam is excited by a moment. The fractions originate from an estimated point of application of the force for the resulting moment. The wave forces decrease exponentially and are estimated to be represented by a triangle, thus the point of application is two-thirds of the length viewed from the base of the force. The other forces are considered to be represented most accurately by a rectangle, thus the point of application is half of the length viewed from the base of the force. The points of action of the forces can also be viewed in figures 3.9 and 3.10. The angles α_1, α_2 and α_3 mentioned in matrix 4.25 are the angles of respectively the waves, current and wind with the x-axis of the system. If the angle is zero, the excitation forces will act unidirectional in the x-direction.

$$\vec{Moment} = \begin{bmatrix} \frac{2L_1}{3} F_{wave}(t)\, cos(\alpha_1) + \frac{L_1}{2} F_{current}(t)\, cos(\alpha_2) + \left(F_{air,1}(t) + F_{air,2}(t)\right) L_1\, cos(\alpha_3) \\ \left(\frac{1}{2} F_{air,1}(t) + F_{air,2}(t)\right) L_2\, cos(\alpha_3) \\ \frac{L_3}{2} F_{air,2}(t)\, cos(\alpha_3) \\ \frac{2L_1}{3} F_{wave}(t)\, sin(\alpha_1) + \frac{L_1}{2} F_{current}(t)\, sin(\alpha_2) + \left(F_{air,1}(t) + F_{air,2}(t)\right) L_1\, sin(\alpha_3) \\ \left(\frac{1}{2} F_{air,1}(t) + F_{air,2}(t)\right) L_2\, sin(\alpha_3) \\ \frac{L_3}{2} F_{air,2}(t)\, sin(\alpha_3) \end{bmatrix} \tag{4.25}$$

$$\vec{\theta} = \begin{bmatrix} \theta_1 \\ \theta_2 \\ \theta_3 \\ \theta_4 \\ \theta_5 \\ \theta_6 \end{bmatrix} \tag{4.26}$$

It can be observed that the matrices are symmetric, but not diagonal and not orthogonal. This means the equations of motion are coupled. In case of the stiffness matrix, this means that a change of stiffness in x-direction directly impacts the stiffness in another direction. It can also be noted that the diagonal entries of the damping and stiffness matrix are positive for certain combinations of R_j and M_j, which indicates that the system is stable.

The upper left part and lower right part of the mass matrix and stiffness matrix have the same entries. This is due to the equal characteristics and parameters of the support structure in both the $z-x$ and $z-y$ plane.

4.5. Parameters

In this section, values for several parameters are obtained. Table 4.1 sums up all the input parameters of the model in this chapter. Some parameters have multiple values, such as the significant wave height, due to a varying sea-state. These sea-states were chosen as to represent a calm and normal sea-state to compare support structure and blade behaviour in different weather conditions in which installation might be possible. A rough sea-state was added to emphasise the effect of waves on the support structure and blade.

Table 4.1: Independent parameters wind turbine model Lagrange method.

Parameter	unit	Value		
g	m/s^2	9.81		
$U_{wind,mean}$	m/s	7 - 11 - 20		
H_s	m	1 - 2.5 - 7		
T_p	s	6 - 7.74 - 13		
$U_{current}$	m/s	0.7		
α_1	-	30°		
α_2	-	30°		
α_3	-	45°		
h	m	35		
L	m	154.7		
M_t	kg	10e6		
ζ_1	-	0.005		
ζ_2	-	0.005		
ζ_3	-	0.005		
ζ_4	-	0.005		
ζ_5	-	0.005		
ζ_6	-	0.005		
ρ_{water}	kg/m^3	1025		
ρ_{air}	kg/m^3	1.225		
ρ_{steel}	kg/m^3	7850		
E_{steel}	Pa	210e9		
$C_{D,wind}$	-	0.7		
$C_{D,water}$	-	0.7		
$C_{M,water}$	-	2		
j	-	1	2	3
$D_{ou,j}$	m	11	10	8.1
t	m	0.08	0.06	0.04
$D_{in,j}$	m	10.84	9.88	8.02
L_j	m	35	77.35	77.35

The relation for wall thickness in equation 4.27 applies only to monopiles. The outer diameter of the 15 MW IEA wind turbine at hub height and mean sea level are respectively 6.5 m and 10 m [29]. The outer diameter of Zephyros 20 MW monopile is 11 m. The key properties and dimensions of the 15 MW IEA offshore reference wind turbine support structure are publicised, on which the properties and dimensions of the Zephyros' support structure are derived when the outer diameter of 11 m is taken into account. Due to the assumption in this model of the segments being uniform, the scaled dimensions of the support structure are averaged. These averages were a first indication of the support structure diameters, but are different from the values in table 4.1. This is because the diameter is an important property in defining the natural frequencies of the support structure, thus the diameter was modified to suffice other turbine characteristics. This resulted in the values depicted in table 4.1. L_j describes

the length of a member. The use of metocean data input parameters H_s and T_p is explained in section 3.1.2. A mean wind velocity of 11 m/s approaches the current installation boundaries of 8 to 12 m/s [39, 43].

The values in table 4.2 are dependent parameters as they rely on at least one independent parameter mentioned in 4.1, but are relevant to get a good understanding of the model's behaviour. This dependence is represented by some equations. The inner diameter $D_{i,j}$ and wall thickness t of the various members are dependent parameters but are displayed in input parameter table 4.1 with dependent parameters to be able to compare it easily with the outer diameter. Equations 4.27 and 4.28 are needed to determine wall thickness of the monopile and tower in mm [25, 37, 56]. The D/t ratio is increasing due to larger pile diameters. If this ratio does not increase, the wall thickness and mass of a pile will become too large. This is something that is still under research as the industry is always growing.

$$\frac{D}{t} = 160, \quad D > 10 \tag{4.27}$$

$$\frac{D}{t} = 130, \quad D \approx 9 \tag{4.28}$$

$$H_{max} = \frac{2H_s}{\sqrt{8}}\sqrt{ln(N)} = 1.86H_s\,, \quad with\ N = 1000 \tag{4.29}$$

$$M_j = \frac{\pi}{4}(D_{ou,j}^2 - D_{in,j}^2)\rho_{steel}L_j \tag{4.30}$$

$$M_{inside} = \frac{\pi}{4}D_{in,1}^2\rho_{water}L_1 \tag{4.31}$$

$$M_{added} = C_a\frac{\pi}{4}D_{ou,1}^2\rho_{water}L_1 \tag{4.32}$$

$$I_{yy,j} = \frac{\pi}{64}(D_{ou,j}^4 - D_{in,j}^4) \tag{4.33}$$

$$I_j = \frac{M_j L_j^2}{12} + M_j d^2 \tag{4.34}$$

Equation 4.29 calculates the maximum wave height out of 1000 waves that occur in a three hour storm. The significant wave height H_s is a statistic that denotes the characteristic height of random waves in a sea state. It is the average of the highest one-third of waves that occur in a three hour storm when N is 1000 [57].

Equation 4.30 describes the mass of a segment without added mass or mass inside of the segment. For segment one, this is necessary to include. The mass on the inside of the monopile is determined with equation 4.31 and the water added mass is included with equation 4.32. A vibrating structure in water induces acceleration in the water, producing an extra force on the structure. Conveniently, this additional force may be calculated as the result of multiplying the structure's acceleration by an equivalent mass of water outside of the monopile [58]. The water mass inside of the structure is not defined as added mass because it is assumed to move with the monopile instead of pushed aside. Therefore it is not inertia added to a system because of an acceleration. The added mass coefficient C_a is determined as one [25]. When the three masses are added, the value used for M_1 in this chapter is obtained.

Equation 4.33 shows how to calculate the area moment of inertia of a segment. Equation 4.34 gives the equation of the mass moment of inertia. The latter part of equation 4.34 is the parallel axis theorem. Given the body's moment of inertia along a parallel axis via the object's center of gravity and the perpendicular distance between the axes, it may be used to calculate the mass moment of inertia of a rigid body about any axis.

The segments are rigid and the bending stiffness of the segment is modelled as rotational stiffness at the bottom of a segment. The bending stiffness will resemble equation 4.35 including a factor. This factor is determined numerically by equalising the static deflection, first and second natural frequency of a simplified wind turbine model with the static deflection, first and second natural frequency of a cantilever beam with the same properties. This cantilever beam is depicted in figure 4.4 and the simplified wind turbine model is shown in figure 4.3. The parameters that were adjusted to arrive at the simplified wind turbine model are enumerated below.

1. The wind, wave and current forces are eliminated and only one force excites the model at the top of the beam.
2. The top mass is excluded during the cantilever beam calculation.
3. The diameter is constant over the length of the wind turbine support structure.
4. The wall thickness is constant over the length of the wind turbine.
5. The wind turbine outlined in figure 4.3 has a constant area moment of inertia over the length of the wind turbine monopile and tower.
6. Static deflection is achieved in the steady-state solution, damping has been augmented to quickly arrive at this steady-state regime.

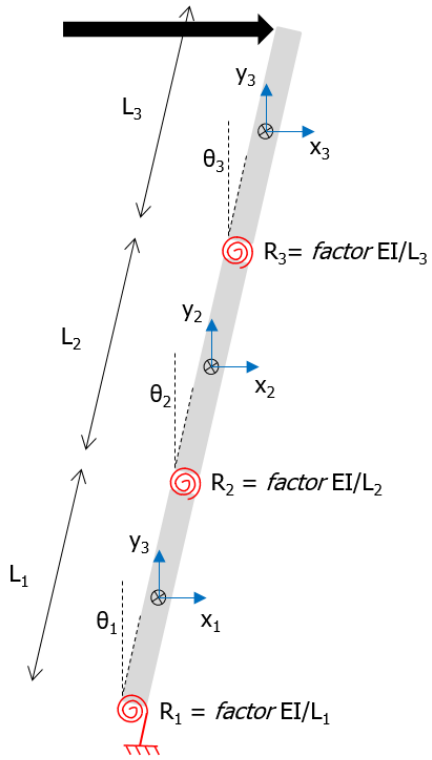

Figure 4.3: Simplified wind turbine model for rotational stiffness validation.

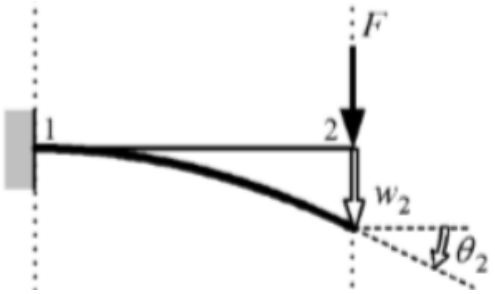

Figure 4.4: Cantilever beam [9].

The deflection of the dynamic system in figure 4.3 corresponds with the deflection of the equation in figure 4.4 when the rotational stiffnesses have the following values: for R_1 the factor resulted in 3.32, for R_2 in 1.35 and for R_3 the factor is 1.07. However, these factors do not take into account the soil stiffness. The stiffness at the seabed is overestimated. A stiffness correction factor is implemented that considers the soil stiffness. This correction factor is not determined without the soil added mass taken into account. An correction factor of 0.8 is added to the already existing factor of 3.32, thus becoming 2.656 [59].

After inserting these factors in equation 4.35 with the non simplified parameters, the three rotational stiffnesses resulted in the values as listed in table 4.2.

$$R_j = factor * \frac{EI_j}{L_j} \tag{4.35}$$

The inner and outer diameter mentioned in table 4.1 are constant over the length of a section in this thesis. Thus the mass per unit length and the area moment of inertia have a constant value per section.

The damping due to soil and material characteristics in the system is included via modal damping. The Rayleigh dissipation function gives the option to choose the amount of damping that is added with a damping coefficient $\zeta_{damping}$. The Rayleigh dissipation function is determined with the help of equations 4.36 to 4.38. In this chapter, the support structure model, the mass M_i, modal mass $\overline{M_j}$, critical damping C_r and damping C are 6x6 matrices. The Modal mass and critical damping are diagonal matrices, where the modal mass matrix is a unit matrix. The advantage of adding damping to the model in this manner is that the damping coefficient $\zeta_{damping,i}$ can be set separately for every mode shape. As the added mass of the water is included in to model, the mode shapes of the support structure will now be referred to as wet mode shapes.

$$[\overline{M}] = \Psi^T [M] \Psi \tag{4.36}$$

$$B_{r,i} = 2\zeta_i \overline{M_j} \omega_i \tag{4.37}$$

$$B = (\Psi^T)^{-1} diagonal(B_r, i) (\Psi)^{-1} \tag{4.38}$$

In section 4.11, the impact of varying the damping coefficient is examined. A study indicated an initial value of the damping coefficient to be between 0.15% and 1.5% [60]. Table 4.22 suggest that every entry is non-zero, but some entries certainly are. Matrix 4.39 elaborates on this, the entries that are non-zero alternate due to varying damping coefficient inputs. Table 4.39 is a result from using equations 4.36 to 4.38.

$$\vec{B} = \begin{bmatrix} B_{11} & B_{12} & B_{13} & 0 & 0 & 0 \\ B_{21} & B_{22} & B_{23} & 0 & 0 & 0 \\ B_{31} & B_{32} & B_{33} & 0 & 0 & 0 \\ 0 & 0 & 0 & B_{44} & B_{45} & B_{46} \\ 0 & 0 & 0 & B_{54} & B_{55} & B_{56} \\ 0 & 0 & 0 & B_{64} & B_{65} & B_{66} \end{bmatrix} \tag{4.39}$$

The effect of the modal damping is validated by comparing the decrease of the maximum deflections of the nacelle over time after an initial deflection of ten meters to the result of equation 4.40. The result is plotted in figure 4.5 and it can be concluded that the damping does what it is expected to do. For both results shown in figure 4.5 the same damping coefficient of 0.0244 is applied to attenuate the 1^{st} damped wet mode shape.

$$x_{top,check} = e^{-\omega_n \zeta_1 t} \tag{4.40}$$

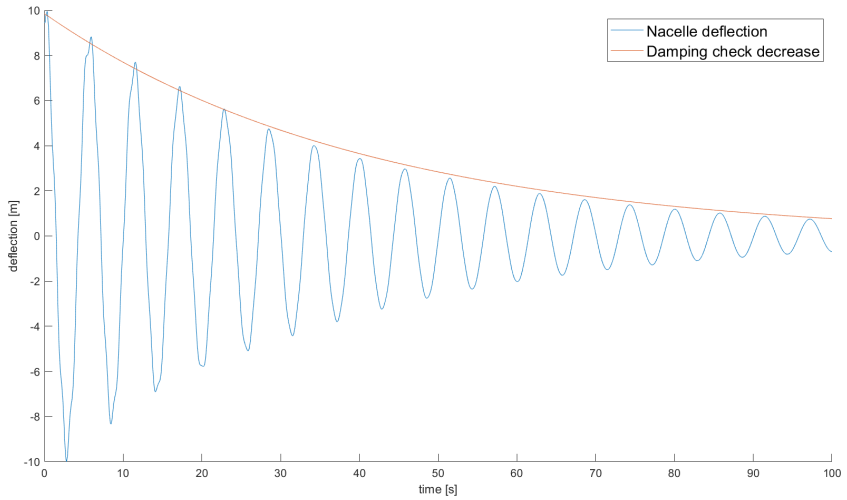

Figure 4.5: Damping validation.

Table 4.2 gives the values of the remaining parameters that depend on at least one parameter listed in table 4.1. The value of M_1 includes the added mass from inside and outside the monopile.

Table 4.2: Dependent parameters wind turbine model Lagrange method.

Parameter	unit	Value		
j	-	1	2	3
M_j	kg	$4.16 * 10^6$	$1.14 * 10^6$	$6.15 * 10^5$
$I_{yy,j}$	m^4	40.91	23.14	8.23
I_j	$kg * m^2$	$4.25 * 10^8$	$5.67 * 10^8$	$3.07 * 10^8$
R_j	N/rad	$6.52 * 10^{11}$	$8.48 * 10^{10}$	$2.39 * 10^{10}$

4.6. Natural Frequencies

A frequency in which a structure naturally vibrates, is called a natural frequency. It is a frequency at which a system freely oscillates in the absence of a driving force. In this section, the derivation of the natural frequencies of the wind turbine support structure, including the nacelle and hub, illustrated in this thesis, is discussed. The first few steps are the general approach of the derivation and are also used later in this study for the calculation of the natural frequencies of the wind turbine blade.

$$\vec{M}\ddot{\vec{\theta}}_j + \vec{K}\vec{\theta}_j = 0 \tag{4.41}$$

Without damping and a driving force, equation 4.19 results in equation 4.41. Having completed the necessary derivation, the natural frequency can be determined using equation 4.43, where $\vec{K}$ and $\vec{M}$ in this section refer to matrices 4.23, 4.24, 4.20 and 4.21. The dimensions of these matrices are $6x6$, indicating that the model has six degrees of freedom, resulting in six wet mode shapes. Equations 4.26 depicts these degrees of freedom. The determined natural frequencies are listed in table 4.3. As can be seen in this table, three wet mode shapes are solely in the $z-x$ plane and three are in the $z-y$ plane. The two planes are uncoupled and therefore the wet mode shapes have similar natural frequencies.

$$(-\omega_n^2\vec{M} + \vec{K})\vec{\theta} = 0 \tag{4.42}$$

$$\omega_n = \sqrt{\frac{\vec{K}}{\vec{M}}} \tag{4.43}$$

$$T = \frac{2\pi}{\omega_n}\ [rad/s] \tag{4.44}$$

$$f_n = \frac{1}{T}\ [Hz] \tag{4.45}$$

Table 4.3: Natural frequencies of six wet mode shapes of offshore wind turbine support structure.

	$\omega\ [rad/s]$	$f\ [Hz]$	$T\ [s]$	mode shape
1	1.0991	0.1749	5.7166	1^{st} $z-x$
2	1.0991	0.1749	5.7166	1^{st} $z-y$
3	6.7017	1.0665	0.9376	2^{nd} $z-x$
4	6.7017	1.0665	0.9376	2^{nd} $z-y$
5	20.8115	3.3123	0.3019	3^{rd} $z-y$
6	20.8115	3.3123	0.3019	3^{rd} $z-x$

The frequencies to not coincide with the rotor (1P) and blade passing frequency (3P). The 15 MW reference turbine of IEA has a first tower-monopile frequency of 0.17 Hz [29]. If the approach of this

research is used to calculate the first tower-monopile frequency of an offshore wind turbine with the characteristics of the 15 MW reference turbine of IEA, the frequency is circa 0.156 Hz. Table 4.4 lists the input parameters of the 15 MW turbine that are adjusted in the calculation. The diameters of the tower and monopile of the 15 MW turbine are averaged per segment, of which three exist in this research. The first tower frequency is very susceptible to variation of the averaged diameter. This causes the minor deviation of the result. Additionally, the approach of the soil stiffness is different. The soil stiffness has considerable influence on the first support structure frequency.

Table 4.4: Parameters of 15 MW IEA reference wind turbine.

Parameter	Unit	Magnitude
Hub height	[m]	150
Water depth	[m]	30
Monopile diameter	[m]	10
Top mass	[kg]	$1.02 * 10^6$
Modus of Elasticity	[Pa]	$200 * 10^9$

Another method of determining the natural frequencies is with the Eigenvalue problem. The square root of the Eigenvalues are the natural frequencies and the Eigenvectors are the entries of the degrees of freedom to create three wet mode shapes. The wet mode shapes corresponding the natural frequencies are depicted in appendix E. The Eigenvectors are more extensively discussed in section 4.5.

Resonance is the term used to describe the phenomenon of enhanced amplitude that occurs when the frequency of an applied periodic force is equal to or near the natural frequency of the system on which it acts. The resonance frequency is not equal to the natural frequency if damping occurs. The resonance frequency is important to consider when comparing it with the JONSWAP spectrum in figure 3.2. Equation 4.46 is used to calculate the resonance frequency [61] of a mode. The damping ratio is different for every wet mode shape. The damping ratio is also varied for a sensitivity analysis and thus the resonance frequency is not fixed.

$$\omega_r = \omega_n \sqrt{1 - \zeta_i^2} \tag{4.46}$$

The resonance frequency has to coincide to some extent with a single wave frequency of the irregular wave. Frequencies between the peaks have less energy to excite any movements.

4.7. Forcing vector

In this section, the calculations of the different aforementioned forces of the waves, current and wind exciting the wind turbine are described. Eventually, these forces will lead to moments that are incorporated in the equations of motion after taking the partial derivatives of the work done by the forces. Every force mentioned in this section is a unidirectional force and can take on any direction in the horizontal plane individually.

The wave and wind forces are time-dependent and the current has a constant velocity and is thus time-independent. Values of parameters used in the following equations are accessible in tables 4.1 and 4.2. The forces are mitigated by environmental damping, which is included by taking the velocity of the support structure relative to the waves, current and wind as input velocity of the forces. This relative velocity is depicted in equations 4.47, 4.54 and 4.56.

Wave force

Equation 4.47 returns a time-dependent wave force, consisting of an inertia and a drag force. The current and wind forces consist only of drag forces.

$$\begin{aligned} F_{wave}(t) = F_{wave,inertia}(t) + F_{wave,drag}(t) = \frac{\pi}{4}\rho_{water}\, C_{M,water}\, D_1^2\, a_{wave}(t) + \\ \frac{1}{2}\,\rho_{water}\, C_{D,water}\, D_1 \left(U_{wave}(t) - U_{support}(t)\right) \left|U_{wave}(t) - U_{support}(t)\right| \end{aligned} \tag{4.47}$$

Equation 4.47 contains two time-dependent variables, the wave velocity and the wave acceleration in x-direction. The origin of both variables is clarified below in equations 4.48 and 4.49. The wave velocity and acceleration are integrated over water depth z.

$$U_{wave}(t) = \omega_i \, A_i \, \frac{cosh[k(d+z)]}{sinh(kd)} \cdot sin(\omega t) \tag{4.48}$$

$$a_{wave}(t) = \omega_i^2 \, A_i \, \frac{cosh[k(d+z)]}{sinh(kd)} \cdot cos(\omega t) \tag{4.49}$$

$$k = \frac{2\pi}{\lambda_{wave}} \tag{4.50}$$

The wave frequency is ω_i and k is the corresponding wave number calculated with equation 4.50. The local water depth is d and z is the vertical position with respect to the mean sea level. The wave velocity $U_{wave}(t)$ relative to the support structure velocity $U_{support}(t)$ is squared to derive the wave drag force $F_{wave,drag}$. Both velocities are determined in the point of action of the wind force, at $2/3^{rd}$ the monopile height. Squaring the relative velocity changes the sine in equation 4.48 into a cosine, equation 4.51 elaborates on this.

$$sin^2(t) = \frac{1 - cos(2t)}{2} \tag{4.51}$$

Before the wave velocities and accelerations and therefore the time-dependent force can be established, the wave amplitude A_i per wave frequency needs to be determined, after which it can be inserted in equations 4.48 and 4.49. The amplitude of a single sine wave can be calculated with the spectral density and equation 4.52 [62].

$$A_i = \sqrt{2 \, S_\zeta(\omega_i) \, \delta\omega_i} \tag{4.52}$$

An advantage of a unidirectional force is that an irregular wave force can be constructed in the time domain through the principle of superposition of waves. Sine waves combined create a wave elevation time series. An unidirectional irregular wave is a wave with one degree of freedom, in which the wave elevation is the single degree of freedom that changes over time.

An irregular wave consisting of 30 stochastic sine waves is used for excitation. Equation 4.53 demonstrates how the wave elevation in figure 4.6 is constructed. Figure 4.6 is the result of an in-plane wave elevation rendered from a calm sea-state with a significant wave height of 1 meter and a corresponding spectral peak period of 6 seconds. Figure 4.7 is the corresponding force profile of the wave elevation in figure 4.6. This method of approaching a wave profile in time is only applicable if the force is unidirectional.

$$\overline{\zeta_{sea-state}} = \sum_{i=1}^{30} A_i \, sin(\omega_i t + \epsilon) \tag{4.53}$$

It is possible to create a pattern that has the same total variance and closely resembles the record from which the spectrum was obtained by superimposing 15 to 20 component waves [62]. For this research, 30 components are used, which enlarges the accuracy. All 30 waves have a stochastic value for the phase angle ϵ between zero and 2π. The Amplitudes are determined with the help of the JONSWAP spectrum. Referring back to figure 3.2, the range between zero en 2 rad/s is divided in 30 randomly sized bins. These bins have an average value, the frequency ω_i and an average height, the spectral density S. $\delta\omega_i$ also varies per wave as the width or bin size is randomly sized.

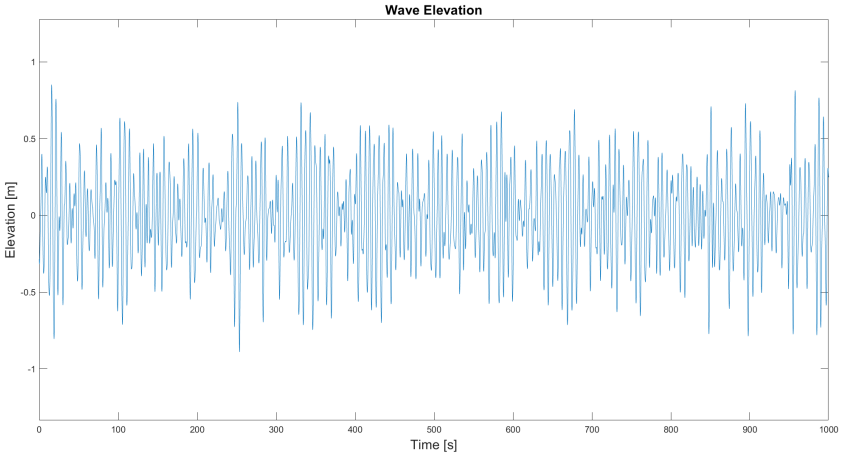

Figure 4.6: Unidirectional wave elevation of calm sea-sate.

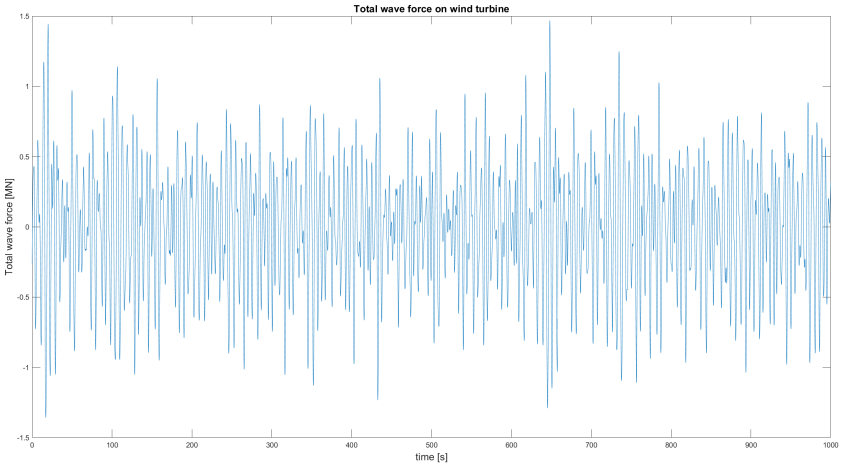

Figure 4.7: Unidirectional wave force of calm sea-sate.

Current force

As mentioned in equation 4.25, the matrix contains time-independent forces as well. The time period considered does not last long enough to take large tide amplitudes into account, therefore the current force is constant and calculated with equation 4.54. Again the velocity of the current relative to the support structure is used when determining the current force. The parameters are listed in table 4.1. The velocities depicted in equation 4.54 are determined at mid-length of the monopile height.

$$F_{current}(t) = \frac{1}{2}\,\rho_{water}\,C_{D,water}\,A_{waves}\,\left(U_{current} - U_{support}(t)\right)\left|U_{current} - U_{support}(t)\right| \tag{4.54}$$

Wind force

Equation 4.25 includes two wind forces. This is because the tower is divided in two equivalent lengths and thus consists of two members with two centers of gravity. The wind velocity is conducted similarly to the wave elevation, but consisting of 60 component waves. The determined irregular wave has a mean wind velocity of 11 m/s. The wind velocity is composed by creating a wind spectrum from measured data provided by Allseas. This wind spectrum is used to create an wind velocity time series with equation 4.55, where A_i is the value on the y-axis of figure 4.9. The wind spectrum of the measured time series provided by Allseas Engineering and the wind spectrum of the created time series can be seen in figure 4.9 and the corresponding wind velocity time series in figure 4.8. The wind velocities displayed in figure 4.8 are at hub height. The average wind velocity is excluded from both wind spectra

for a better understanding of the figure. In the results of this chapter, a sensitivity analysis of the impact of varying average wind velocities is conducted.

$$\overline{\zeta_{wind}} = \sum_{i=1}^{60} A_i \, sin(\omega_i t + \epsilon) \tag{4.55}$$

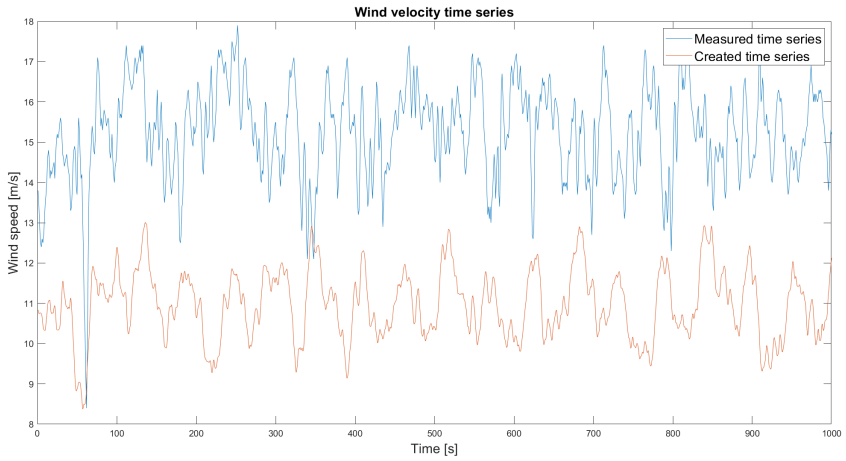

Figure 4.8: Wind velocity time series used in the research.

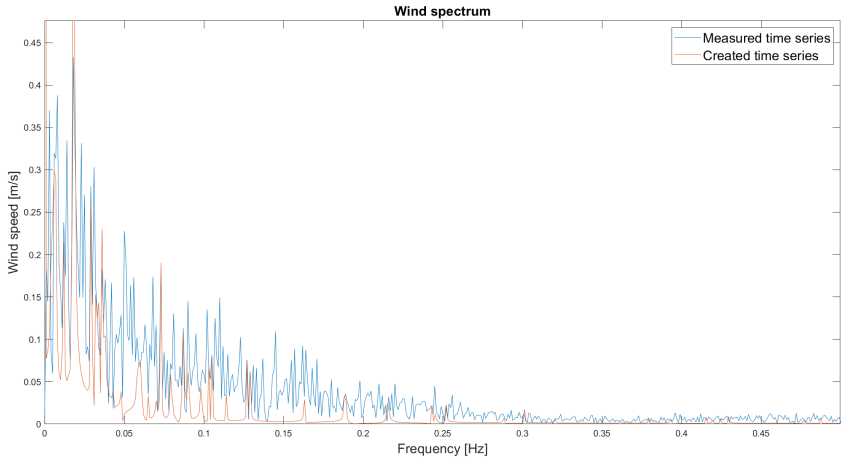

Figure 4.9: Wind spectra of a measured wind velocity time series and the created time series.

As mentioned above, the wind velocities displayed in figure 4.8 are at hub height. The points of leverage of the two wind forces are at the centers of gravity of the two upper segments, 73.68 m and 151.03 m. Equations 3.3 and 3.2 are used to define a wind speed scale factor, which is incorporated in the wind force equation as a factor. The factor is squared as it accompanies the squared wind velocity. For 38.68 m, the factor is 0.884 and for 116.03 m, the factor is 0.969. Equation 4.56 is used to convert the wind velocity into a wind force. The area of the pile is the length of a segment multiplied with the diameter of a segment, which is uniform over the height of one segment. Again the velocity of the wind is taken relative to the velocity of the support structure at the points of action of a force, that is the centers of gravity of the middle and upper segment.

$$F_{wind}(t) = factor^2 \, \frac{1}{2} \, \rho_{wind} \, C_{D,wind} \, A_{wind} \, \left(U_{wind}(t) - U_{support}(t)\right) \left|U_{wind}(t) - U_{support}(t)\right| \tag{4.56}$$

Table 4.7 contains the maxima of the separate forces mentioned in this section. The area parameter A_{wind} decrease from the middle segment to the upper segment is greater than the increase of the wind

velocity squared due to the height difference. The area of the nacelle is not included as the nacelle-hub assembly is modelled as a point mass. This creates a situation where the wind force on the middle segment with a lower wind velocity but a bigger surface area is the larger force, and wind the force acting on the upper segment is smaller. This is also shown in table 4.7. The calm, normal and rough sea-states are accompanied with different average wind velocities. This is listed in table 4.5. The angle of incidence of the forces is alternated to conduct a sensitivity analysis and for a visualisation of these forces and angles, section 3.3 should be consulted.

4.8. Support Structure Results and Sensitivity Analysis

The output of the support structure model is motions. The deflections and velocities determined can differ due to different input parameters and variables. Firstly, various metocean input data is used. Secondly, the damping is alternated. Thirdly, the impact of changing the nacelle mass is analysed. Lastly, the dimensions of the wind turbine are altered.

Every simulations lasts 1000 seconds. At that point, the steady-state regime is achieved for some time. When determining the maximum values given in this section, only the second half of the simulation is taken into account to exclude the transient-state motions from the results.

Some results are plotted in appendix E to support the results listed in this section.

4.8.1. Metocean data

In this section, the varying metocean data is the wave spectrum and thus wave force. First the significant wave height and matching spectral peak periods are varied. The spectral peak period is calculated with the help of equation 4.57. The equation gives a range, therefore a random value above the average is assumed. The following combinations that are used as input are listed in table 4.5. The maximum wave heights are calculated with equation 4.29. The mean wind velocities were determined with the help of the website Windy.com by looking up the values of significant wave height and using the corresponding wind velocities provided by Windy.com [63].

Table 4.5: Different metocean conditions used as input parameters.

Parameter	Unit	Calm	Normal	Rough
Significant wave height	[m]	1	2.5	7
Spectral peak period	[s]	6	7.8	13
Maximum wave height	[m]	1.86	4.65	13.02
Current velocity	[m/s]	0.7	0.7	0.7
Mean wind velocity	[m/s]	7	11	20

$$\sqrt{13H_s} < T_p < \sqrt{30H_s} \tag{4.57}$$

The wave profiles created in section 4.7 are an approach of the wave spectra with the characteristics listed in table 4.5. The data of the obtained irregular wave profiles were converted into a wave spectrum, which resulted in the significant wave heights, the spectral peak periods and the maximum wave heights as listed in table 4.6. These deviate slightly from the values in table 4.5 as the spectra are an approach of the JONSWAP spectra.

Table 4.6: Different metocean conditions used as input parameters.

Parameter	Unit	Calm	Normal	Rough
Significant wave height	[m]	1.15	2.87	7.61
Spectral peak period	[s]	5.75	8.77	12.99
Maximum wave height	[m]	1.74	4.94	11.71
Current velocity	[m/s]	0.7	0.7	0.7
Mean wind velocity	[m/s]	7	11	20

The maximum environmental forces of multiple sea-states are listed in table 4.7. The maximum total force is not the sum of the listed maximum forces as the maximum wind and wave forces do not

necessarily occur simultaneously. For a calm, normal and rough sea-state, the input parameters H_s and T_p differ and therefore different wave forces emerge. The same can be said about the wind forces. The dimensions of the wind turbine used to determine these forces can be found in table 4.1.

Table 4.7: Magnitudes of maximum excitation forces acting on wind turbine support structure.

	Unit	Calm	Normal	Rough
Max wave force	[MN]	1.70	3.95	9.85
Current drag	[kN]	67.7	67.7	67.7
Max wind force lower part	[kN]	21.0	43.9	125.5
Max wind force upper part	[kN]	20.5	42.7	122.2
Max total force	[MN]	1.78	4.08	10.1

Table 4.8 has the equivalent moments of the forces acting on the wind turbine support structure. Again, the maximum overturning moment is not the sum of the listed maximum moments as the maximum wind and wave moments do not necessarily occur simultaneously.

Table 4.8: Magnitudes of maximum excitation moments acting on wind turbine support structure.

	Unit	Calm	Normal	Rough
Max wave moment	[MNm]	39.6	92.3	229.7
Max current moment	[MNm]	1.18	1.18	1.18
Max wind moment	[MNm]	4.61	9.68	27.7
Max total overturning moment	[MNm]	42.9	99.9	252.2

Table 4.9 contains the maximum deflections and velocities of simulations of 1000 seconds for three sea-states. The unidirectional wave, current and wind forces have the same orientation in inflict the maximum possible deflection, this is a conservative assumption because the forces will most likely not have the same orientations. This is only done for the purpose of this sensitivity analysis section to investigate the impact of the different weather conditions, damping, top masses and dimensions. The deflections and velocities over time are plotted in appendix E.

Table 4.9: Maximum deflections and velocities of support structure in different sea-states.

	Unit	Calm	Normal	Rough
Deflection	[m]	0.155	0.397	0.478
Ratio	[-]	-	+156.1%	+208.4%
Velocity	[m/s]	0.160	0.416	0.444
Ratio	[-]	-	+160.0%	+177.5%

The increase from a calm to a normal sea-state has a large impact on the deflection and velocity of the hub, but the increase from a normal to a rough sea-state is not significant. This is due to the amount of energy that a sea-state has at the resonance frequency, which is not significantly increasing either. The peaks that are closest to the first resonance frequency in both planes can be viewed in appendix C. In these figures, the difference in spectral energy can be observed between the normal en rough sea-state.

4.8.2. Force angles

In this section, different combinations of angle of incidence of the waves, current and wind are examined. It is assumed that the worst possible combination occurs with equal angles. This analysis could be used to determine the angle with the wind in the horizontal plane at which blade installation is preferable.

Table 4.10: Force angle of incidence variation sensitivity analysis of support structure.

Wave and current angle [-]	Wind angle [-]	Max Deflection [m]	Max Velocity [m/s]
0°	0°	0.155	0.160
0°	45°	0.153	0.160
0°	90°	0.149	0.161
45°	0°	0.153	0.160
30°	90°	0.152	0.161
30°	45°	0.155	0.160

4.8.3. Damping

In this section, the influence of damping is investigated by varying the damping coefficient associated with the 1^{st} and 2^{nd} damped natural frequencies. A calm sea-state is assumed. The remaining four wet mode shapes of the support structure have a damping coefficient of 0.5% throughout the sensitivity analysis of this chapter.

The environmental damping of the 1^{st} and 2^{nd} wet mode shape, respectively also referred to as the 1^{st} wet mode shape in the $z-x$ and the $z-y$ plane, is varied and the impact of a tuned mass damper is investigated as well. A rough sea-state is assumed. The damping coefficient without a tuned mass damper is 0.5%, which is solely material damping. Environmental damping is achieved by implementing the relative velocities and cannot be affected. Additionally, a relative damping ratio that can be achieved with a tuned mass damper is implemented. To emphasise the effect of the tuned mass damper, multiple tuned mass dampers with increased damping coefficients are tested.

Table 4.11: Maximum deflections and velocities of support structure for varying damping coefficients.

Damping Coefficient [-]	Deflection [m]	Ratio [-]	Velocity [m/s]	Ratio [-]
0.005	0.155	-	0.160	-
0.02	0.103	-33.5%	0.104	-35.0%
0.03	0.085	-45.2%	0.084	-47.5%
0.055	0.062	-60.0%	0.062	-61.3%

Damping has a lot of effect on the support structure. The use of a tuned mass damper is remarkably enhancing blade behaviour when set to at least 2.5%, summing up to a total damping coefficient of 3%. Additional damping is more difficult to achieve and does not result in significant improvement of blade behaviour unless the damping is greatly increased. It is assumed that a tuned mass damper with a damping coefficient of 2.5% is feasible [31, 64]. A different study conducted on the effect of a passive tuned mass damper on blade root impacts during the offshore mating process resulted in a total damping ratio of 5.6% by adding a tuned mass damper to a monopile [65]. The research focused on the 10 MW DTU reference offshore wind turbine [30]. Hence, the total damping coefficient is set at 5.5%, creating an attenuation of % for the velocity, which will be the important parameter when the kinetic energy is taken into account.

4.8.4. Nacelle mass

This section examines the variation of weight on top of the support structure. For instance, the motions without any top mass are investigated.

The scaled wind turbine in this research features three blades. During the installation of the second blade, the nacelle mass increases with the mass of one blade that is already installed and during the installation of the third blade, the nacelle mass increases with the mass of two blades that are already installed. A blade has a mass of 89.42 tonnes, this is discussed in chapter 5. The assumption was made that the nacelle is modelled as a point mass, so there is no aerodynamic behaviour of the installed blade(s). If the aerodynamic profile of the blade is included, the wind load increases, as the load area increases.

It is also possible that the scaled weight of the nacelle, 1000 tonnes, is an overestimation. Therefore less mass is also examined in the amount of 800 tonnes.

Table 4.12: Maximum deflections and velocities of support structure for varying top mass.

Blades	Mass [t]	Frequency [Hz]	Deflection [m]	Ratio [-]	Velocity [m/s]	Ratio [-]
0	0	0.3541	0.061	-60.6%	0.112	-30.0%
0	1000	0.1749	0.155	-	0.160	-
1	1089.42	0.1690	0.176	+13.5%	0.179	+11.9%
2	1178.84	0.1635	0.177	+14.2%	0.174	+8.8%
3	1250	0.1595	0.188	+21.3%	0.188	+17.5%

The deflections and velocities increase as expected when mass is added to the top of a structure. The top mass has a destabilising effect on the support structure. The first resonance frequency of the support structure is greatly affected by a varying top mass. The peak frequencies of the irregular wind and wave spectra do not all have the same spectral density. A large change in resonance frequency could have a big impact in the amount of energy that excites the support structure. This explains the inconsistent pattern of maximum deflections and velocities.

4.8.5. Monopile Diameters and Wall Thickness

Another important aspect of the support structure model are the dimensions. The impact of change in monopile diameter and monopile wall thickness is researched in this section. Firstly, the monopile is varied, with the input parameters from table 4.1 as a baseline. The baseline is a support structure with a monopile diameter of 11 meters. The results are shown in table 4.13.

Table 4.13: Maximum deflections and velocities of support structure for varying monopile diameters.

Diameter [m]	Deflection [m]	Ratio [-]	Velocity [m/s]	Ratio [-]
10	0.224	+44.5%	0.234	+46.3%
11	0.155	-	0.160	-
12	0.084	-45.8%	0.085	-46.9%

Secondly, the wall thickness of the monopile is varied, with the input parameters from table 4.1 as a baseline.

Table 4.14: Maximum deflections and velocities of support structure for varying monopile wall thicknesses.

Thickness [m]	Deflection [m]	Ratio [-]	Velocity [m/s]	Ratio [-]
0.06	0.268	+72.9%	0.281	+75.6%
0.08	0.155	-	0.160	-
0.10	0.078	-49.7%	0.079	-50.6%

As expected, a stiffer support structure deflects less and a less stiffer support structure deflects more. The velocities trace the same trajectory. A softer support structure has a lower first resonance frequency, shifting closer to the peak frequencies of the calm, normal and rough sea-states used as input, which is not convenient when designing a wind turbine.

4.8.6. Z-component

In this section, the motions of the support structure including nacelle and hub in the three weather conditions are observed again. Table 4.15 lists the deflections compared to the initial position and velocities in z-direction.

Table 4.15: Maximum deflections and velocities in z-direction of nacelle and hub in different sea-states.

	Unit	Calm	Normal	Rough
Deflection	[m]	$3.71 * 10^{-9}$	$3.22 * 10^{-8}$	$4.80 * 10^{-7}$
Velocity	[m/s]	$8.90 * 10^{-5}$	$5.94 * 10^{-4}$	$7.78 * 10^{-4}$

The results show that the influence of the z-deflection and velocity is insignificant. This means that the motions of the hub are examined in the horizontal plane from here on.

5

Blade dynamic modelling

The behaviour of a wind turbine blade is in this chapter approached using the Lagrangian method. Firstly, the model layout is described. Secondly, a sensitivity analysis of the support structure is conducted. Fundamentally, the Lagrangian method's principle is equal for all models discussed in this thesis. For a detailed explanation of the Lagrangian method, see section 4.1.

5.1. Assumptions

Similar to the previous wind turbine tower model, the model describing the behaviour of the wind turbine blade is in 3D.

To delineate the problem, assumptions have been made anew. The assumptions are listed below.

1. The model is constructed in 3D.
2. Small angle approximation is applied, 2^{nd}-order Taylor polynomial is taken into account.
3. The system consists of one cable and three rigid beam segments interconnected by rotational springs, which together form a blade suspended from a crane.
4. The cable is a longitudinal and rotational spring.
5. The hoist crane is located on a floating vessel, causing crane boom tip motions.
6. The gripper or blade yoke is modelled as a point mass at the center of gravity of the blade.
7. Aerodynamic damping is introduced by incorporating the wind velocity relative to the blade velocities.
8. Material damping is introduced as modal damping.
9. The wind velocity is modelled as a group of sine waves based on a wind spectrum with a low frequency range.
10. Any torsional motion of the blade is disregarded.
11. An angle is added as initial condition to imitate prebend, but real prebend is achieved later in steady-state.

5.2. Model introduction

The model configuration of the wind turbine blade suspended from a crane in motion is in 3D. For illustration purposes, figure 5.1 depicts the 3D blade model in the $z-x$ plane and figure 5.2 shows the 3D blade model in the $x-y$ plane. Multiple coordinates can be observed from both figures, the subscripts taken as a distinction. The subscript 0 is the crane boom tip, 1 is the center of gravity of the entire blade and the subscripts 2, 3 and 4 indicate the centers of gravity of the three separate

rigid beams. The system's nine degrees of freedom are enumerated below. The crane boom tip motions are pre-known motions provided by Allseas Engineering and therefore do not provide any degrees of freedom.

1. The longitudinal deflection of the hoist cable u.
2. The rotation θ_1 allowing the pendulum motion around the crane boom tip in the $z-x$ plane.
3. The rotation θ_5 allowing the pendulum motion around the crane boom tip in the $z-y$ plane.
4. θ_2 is the pitch rotation of the blade around its center of gravity.
5. θ_6 is the yaw rotation in the $x-y$ of the blade around its center of gravity.
6. θ_3 and θ_4 allow the internal rotation of the blade in the $z-x$ plane.
7. θ_7 and θ_8 allow the internal rotation of the blade in the $x-y$ plane.

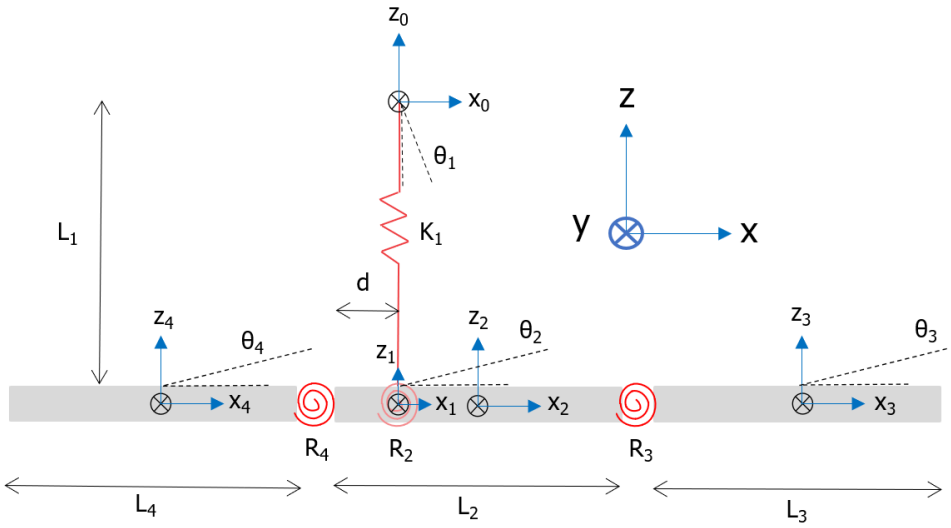

Figure 5.1: Free body diagram wind turbine blade in z-x plane.

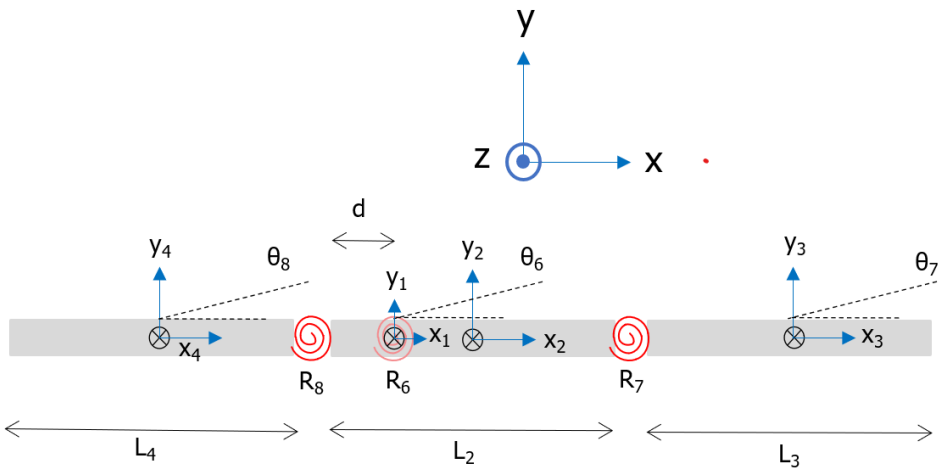

Figure 5.2: Free body diagram wind turbine blade in x-y plane.

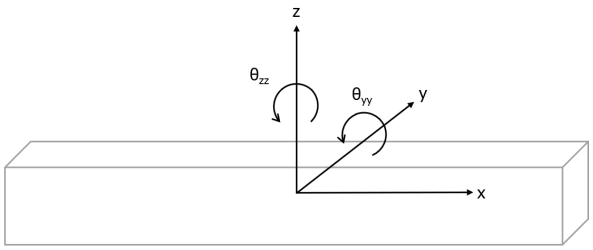

Figure 5.3: Degrees of freedom of a blade segment.

Figure 5.3 supports the free body diagrams with an illustration of the translations and rotations per segment allowed by the degrees of freedom enumerated above.

A large wind turbine blade has prebend, which is accounted for in the model. To prevent ambiguity, the prebend has been omitted from figures 5.1 and 5.2 and the subsequent equations 5.1, 5.2 and 5.3. These equations give the generalised coordinates of above mentioned centers of gravity. The subscripts $left$ and $right$ represent both tips of the blade. Especially the left tip, the blade root with a circular cross section, is critical in order to be able to describe the relative motion between wind turbine tower and blade. It should be noted that the small angle approximation is implemented, therefore $sin(\theta) = \theta$ and $cos(\theta) = 1 - \theta^2/2$. Furthermore, the parameter d has been created to define the distance between coordinate 1 and the left end of segment 2. The value of this parameter is calculated as such that coordinate 1 corresponds to the center of gravity of the blade. If the weight distribution of the blade shifts, coordinate 1 shifts as well.

$$
\begin{aligned}
x_1 &= x_0 + (L_1 + u)\,\theta_1\left(1 - \frac{\theta_5^2}{2}\right)\\
x_2 &= x_0 + (L_1 + u)\,\theta_1\left(1 - \frac{\theta_5^2}{2}\right) + \left(\frac{L_2}{2} - d\right)\left(1 - \frac{\theta_2^2}{2}\right)\left(1 - \frac{\theta_6^2}{2}\right)\\
x_3 &= x_0 + (L_1 + u)\,\theta_1\left(1 - \frac{\theta_5^2}{2}\right) + (L_2 - d)\left(1 - \frac{\theta_2^2}{2}\right)\left(1 - \frac{\theta_6^2}{2}\right) + \frac{L_3}{2}\left(1 - \frac{\theta_3^2}{2}\right)\left(1 - \frac{\theta_7^2}{2}\right)\\
x_4 &= x_0 + (L_1 + u)\,\theta_1\left(1 - \frac{\theta_5^2}{2}\right) - d\left(1 - \frac{\theta_2^2}{2}\right)\left(1 - \frac{\theta_6^2}{2}\right) - \frac{L_4}{2}\left(1 - \frac{\theta_4^2}{2}\right)\left(1 - \frac{\theta_8^2}{2}\right)\\
x_{right} &= x_0 + (L_1 + u)\,\theta_1\left(1 - \frac{\theta_5^2}{2}\right) + (L_2 - d)\left(1 - \frac{\theta_2^2}{2}\right) + L_3\left(1 - \frac{\theta_3^2}{2}\right)\left(1 - \frac{\theta_7^2}{2}\right)\\
x_{left} &= x_0 + (L_1 + u)\,\theta_1\left(1 - \frac{\theta_5^2}{2}\right) - d\left(1 - \frac{\theta_2^2}{2}\right)\left(1 - \frac{\theta_6^2}{2}\right) - L_4\left(1 - \frac{\theta_4^2}{2}\right)\left(1 - \frac{\theta_8^2}{2}\right)
\end{aligned}
\tag{5.1}
$$

$$
\begin{aligned}
y_1 &= y_0 + (L_1 + u)\,\theta_5\left(1 - \frac{\theta_1^2}{2}\right)\\
y_2 &= y_0 + (L_1 + u)\,\theta_5\left(1 - \frac{\theta_1^2}{2}\right) + \left(\frac{L_2}{2} - d\right)\left(1 - \frac{\theta_2^2}{2}\right)\theta_6\\
y_3 &= y_0 + (L_1 + u)\,\theta_5\left(1 - \frac{\theta_1^2}{2}\right) + (L_2 - d)\left(1 - \frac{\theta_2^2}{2}\right)\theta_6 + \frac{L_3}{2}\left(1 - \frac{\theta_3^2}{2}\right)\theta_7\\
y_4 &= y_0 + (L_1 + u)\,\theta_5\left(1 - \frac{\theta_1^2}{2}\right) - d\left(1 - \frac{\theta_2^2}{2}\right)\theta_6 - \frac{L_4}{2}\left(1 - \frac{\theta_4^2}{2}\right)\theta_8\\
y_{right} &= y_0 + (L_1 + u)\,\theta_5\left(1 - \frac{\theta_1^2}{2}\right) + (L_2 - d)\left(1 - \frac{\theta_2^2}{2}\right)\theta_6 + L_3\left(1 - \frac{\theta_3^2}{2}\right)\theta_7\\
y_{left} &= y_0 + (L_1 + u)\,\theta_5\left(1 - \frac{\theta_1^2}{2}\right) - d\left(1 - \frac{\theta_2^2}{2}\right)\theta_6 - L_4\left(1 - \frac{\theta_4^2}{2}\right)\theta_8
\end{aligned}
\tag{5.2}
$$

$$
\begin{aligned}
z_1 &= z_0 - (L_1+u)\left(1-\frac{\theta_1^2}{2}\right)\left(1-\frac{\theta_5^2}{2}\right)\\
z_2 &= z_0 - (L_1+u)\left(1-\frac{\theta_1^2}{2}\right)\left(1-\frac{\theta_5^2}{2}\right) + \left(\frac{L_2}{2}-d\right)\theta_2\\
z_3 &= z_0 - (L_1+u)\left(1-\frac{\theta_1^2}{2}\right)\left(1-\frac{\theta_5^2}{2}\right) + (L_2-d)\,\theta_2 + \frac{L_3}{2}\theta_3\\
z_4 &= z_0 - (L_1+u)\left(1-\frac{\theta_1^2}{2}\right)\left(1-\frac{\theta_5^2}{2}\right) - d\theta_2 - \frac{L_4}{2}\theta_4\\
z_{right} &= z_0 - (L_1+u)\left(1-\frac{\theta_1^2}{2}\right)\left(1-\frac{\theta_5^2}{2}\right) + (L_2-d)\,\theta_2 + L_3\theta_3\\
z_{left} &= z_0 - (L_1+u)\left(1-\frac{\theta_1^2}{2}\right)\left(1-\frac{\theta_5^2}{2}\right) - d\theta_2 - L_4\theta_4
\end{aligned}
\tag{5.3}
$$

If the derivative of above mentioned general coordinates is taken, the velocities of the certain coordinates are obtained.

$$
\begin{aligned}
\dot{x}_1 &= \dot{x}_0 + (L_1+u)\,\dot{\theta}_1 + \dot{u}\theta_1\\
\dot{x}_2 &= \dot{x}_0 + (L_1+u)\,\dot{\theta}_1 + \dot{u}\theta_1\\
\dot{x}_3 &= \dot{x}_0 + (L_1+u)\,\dot{\theta}_1 + \dot{u}\theta_1\\
\dot{x}_4 &= \dot{x}_0 + (L_1+u)\,\dot{\theta}_1 + \dot{u}\theta_1\\
\dot{x}_{right} &= \dot{x}_0 + (L_1+u)\,\dot{\theta}_1 + \dot{u}\theta_1\\
\dot{x}_{left} &= \dot{x}_0 + (L_1+u)\,\dot{\theta}_1 + \dot{u}\theta_1
\end{aligned}
\tag{5.4}
$$

$$
\begin{aligned}
\dot{y}_1 &= \dot{y}_0 + (L_1+u)\,\dot{\theta}_5 + \dot{u}\theta_5\\
\dot{y}_2 &= \dot{y}_0 + (L_1+u)\,\dot{\theta}_5 + \dot{u}\theta_5 + \left(\frac{L_2}{2}-d\right)\dot{\theta}_6\\
\dot{y}_3 &= \dot{y}_0 + (L_1+u)\,\dot{\theta}_5 + \dot{u}\theta_5 + (L_2-d)\dot{\theta}_6 + \frac{L_3}{2}\dot{\theta}_7\\
\dot{y}_4 &= \dot{y}_0 + (L_1+u)\,\dot{\theta}_5 + \dot{u}\theta_5 - d\dot{\theta}_6 - \frac{L_4}{2}\dot{\theta}_8\\
\dot{y}_{right} &= \dot{y}_0 + (L_1+u)\,\dot{\theta}_5 + \dot{u}\theta_5 + (L_2-d)\dot{\theta}_6 + L_3\dot{\theta}_7\\
\dot{y}_{left} &= \dot{y}_0 + (L_1+u)\,\dot{\theta}_5 + \dot{u}\theta_5 - d\dot{\theta}_6 - L_4\dot{\theta}_8
\end{aligned}
\tag{5.5}
$$

$$
\begin{aligned}
\dot{z}_1 &= \dot{z}_0 - \dot{u}\\
\dot{z}_2 &= \dot{z}_0 - \dot{u} + \left(\frac{L_2}{2}-d\right)\dot{\theta}_2\\
\dot{z}_3 &= \dot{z}_0 - \dot{u} + (L_2-d)\dot{\theta}_2 + \frac{L_3}{2}\dot{\theta}_3\\
\dot{z}_4 &= \dot{z}_0 - \dot{u} - d\dot{\theta}_2 - \frac{L_4}{2}\dot{\theta}_4\\
\dot{z}_{right} &= \dot{z}_0 - \dot{u} + (L_2-d)\dot{\theta}_2 + L_3\dot{\theta}_3\\
\dot{z}_{left} &= \dot{z}_0 - \dot{u} - d\dot{\theta}_2 - L_4\dot{\theta}_4
\end{aligned}
\tag{5.6}
$$

Equations 5.7 to 5.10 describe the complete motion of the wind turbine blade in 3D. Equation 5.7 is the kinetic energy and consists of two pendulum terms, the rotational inertia of the middle segment around the center of gravity of the blade as a whole in the two planes mentioned before, the translational motions of the two beam ends and the rotational inertia of the two rigid beam ends around their centers of gravity in those same planes. Equation 5.11 gives the rotational inertia of a beam around its center of gravity used in equation 5.7. M_G is used to denote the gripper or blade yoke mass.

$$\begin{aligned} T = {} & \frac{1}{2}M_G(\dot{u}_1^2 + (L_1+u_1)\dot{\theta}_1^2) + \frac{1}{2}M_G(\dot{u}_2^2 + (L_1+u_2)\dot{\theta}_5^2) + \frac{1}{2}M_2\begin{pmatrix}\dot{x}_2\\ \dot{z}_2\end{pmatrix}\bullet\begin{pmatrix}\dot{x}_2\\ \dot{z}_2\end{pmatrix} + \frac{1}{2}I_2\dot{\theta}_2 \\ & + \frac{1}{2}M_3\begin{pmatrix}\dot{x}_3\\ \dot{z}_3\end{pmatrix}\bullet\begin{pmatrix}\dot{x}_3\\ \dot{z}_3\end{pmatrix} + \frac{1}{2}I_3\dot{\theta}_3 + \frac{1}{2}M_4\begin{pmatrix}\dot{x}_4\\ \dot{z}_4\end{pmatrix}\bullet\begin{pmatrix}\dot{x}_4\\ \dot{z}_4\end{pmatrix} + \frac{1}{2}I_4\dot{\theta}_4 + \frac{1}{2}M_2\begin{pmatrix}\dot{x}_2\\ \dot{y}_2\end{pmatrix}\bullet\begin{pmatrix}\dot{x}_2\\ \dot{y}_2\end{pmatrix} + \frac{1}{2}I_2\dot{\theta}_6 \\ & + \frac{1}{2}M_3\begin{pmatrix}\dot{x}_3\\ \dot{y}_3\end{pmatrix}\bullet\begin{pmatrix}\dot{x}_3\\ \dot{y}_3\end{pmatrix} + \frac{1}{2}I_3\dot{\theta}_7 + \frac{1}{2}M_4\begin{pmatrix}\dot{x}_4\\ \dot{y}_4\end{pmatrix}\bullet\begin{pmatrix}\dot{x}_4\\ \dot{y}_4\end{pmatrix} + \frac{1}{2}I_4\dot{\theta}_8 \end{aligned} \tag{5.7}$$

Equation 5.8 is made up of potential energy due to gravity and a longitudinal spring and rotational springs. The longitudinal spring is allows cable elongation and the rotational springs allow the blade to make a pendulum, yaw, pitch or internal blade motion. The subscripts refer to the positions indicated in figure 5.1.

$$\begin{aligned} V = {} & M_G g(L_1+z_1) + \frac{1}{2}R_1\theta_1 + \frac{1}{2}K_1u^2 + M_2g(L_1+z_2) + \frac{1}{2}R_2(\theta_2-\theta_1)^2 \\ & + M_3g(L_1+z_3) + \frac{1}{2}R_3(\theta_3-\theta_2)^2 + M_4g(L_1+z_4) + \frac{1}{2}R_4(\theta_4-\theta_2)^2 \\ & + \frac{1}{2}R_5\theta_5 + \frac{1}{2}R_6\theta_6 + \frac{1}{2}R_7(\theta_6-\theta_7)^2 + \frac{1}{2}R_8(\theta_8-\theta_7)^2 \end{aligned} \tag{5.8}$$

Thereafter, damping is introduced. There are three types of damping present in this system. Aerodynamic and material damping. The damping is introduced as modal damping that focuses on the all natural frequencies of the wind turbine blade model. The damping is arbitrarily added with the Rayleigh dissipation function. Equation 5.9 is the damping in the support structure model. The vector $\dot{q}$ is displayed in equation 5.14.

$$R = \frac{1}{2}\dot{q}\begin{bmatrix} B_{11} & B_{12} & B_{13} & B_{14} & B_{15} & B_{16} & B_{17} & B_{18} & B_{19} \\ B_{21} & B_{22} & B_{23} & B_{24} & B_{25} & B_{26} & B_{27} & B_{28} & B_{29} \\ B_{31} & B_{32} & B_{33} & B_{34} & B_{35} & B_{36} & B_{37} & B_{38} & B_{39} \\ B_{41} & B_{42} & B_{43} & B_{44} & B_{45} & B_{46} & B_{47} & B_{48} & B_{49} \\ B_{51} & B_{52} & B_{53} & B_{54} & B_{55} & B_{56} & B_{57} & B_{58} & B_{59} \\ B_{61} & B_{62} & B_{63} & B_{64} & B_{65} & B_{66} & B_{67} & B_{68} & B_{69} \\ B_{71} & B_{72} & B_{73} & B_{74} & B_{75} & B_{76} & B_{77} & B_{78} & B_{79} \\ B_{81} & B_{82} & B_{83} & B_{84} & B_{85} & B_{86} & B_{87} & B_{88} & B_{89} \\ B_{91} & B_{92} & B_{93} & B_{94} & B_{95} & B_{96} & B_{97} & B_{98} & B_{99} \end{bmatrix}\dot{q}^T \tag{5.9}$$

In the model outlined above, three unidirectional forces are exerted in the horizontal plane as a point load with the point of contact at coordinates with subscript i being 1, 2 and 3, the centers of gravity of the three segments. Figure 5.1 can be notified in support of illustration of the coordinates. Figure 5.6 elaborates more on the forces itself. The forces are drag forces and consist of a x- and y-component. The drag coefficient in equation 5.10 is determined with the help of the Reynolds equation shown in equation 3.9. The surface A_i any force encounters is the area of an individual segment. As previously mentioned, the forces exerted on the blade depend on the relative velocity between wind and blade. The wind speed varies over time, this will be elaborated on in detail section 5.6. Ultimately, in the Lagrange equation, the work performed by a force is considered. Hence, the forces are multiplied by the distance covered in the either the x- or y-direction by coordinates 1, 2 and 3. The angle θ_j is to denote the angle with the x-axis in the horizontal plane the blade is subjected to, with subscript j being 6, 7 or 8.

$$W_i(t) = \frac{1}{2} C_D \rho_{air} A_{blade,i} \theta_j \left(U_{wind,x}(t) - U_{seg,x,i}(t)\right) \left|U_{wind}(t) - U_{seg,i}(t)\right| * x_i + \frac{1}{2} C_D \rho_{air} A_{blade,i} \left(1 - \frac{\theta_j^2}{2}\right) \left(U_{wind,y}(t) - U_{seg,y,i}(t)\right) \left|U_{wind}(t) - U_{seg,i}(t)\right| * y_i \tag{5.10}$$

Equation 5.11 describes the aforementioned rotational inertia of each beam, with the subscripts again referring to figure 5.1. I_2, I_3 and I_4 consist of the basic equation for the mass moment of inertia around the center of gravity of a rod.

$$\begin{aligned} I_2 &= \frac{M_2 L_2^2}{12} \\ I_3 &= \frac{M_3 L_3^2}{12} \\ I_4 &= \frac{M_4 L_4^2}{12} \end{aligned} \tag{5.11}$$

5.3. Equations of motion

Currently, all information is known to be able to create equations of motion of the blade in a 3D configuration. This is the exact same procedure as described in 4.1, with the Lagrangian in equation 4.5 being the principal issue to consider.

$$\vec{M}\ddot{\vec{q}} + \vec{B}\dot{\vec{q}}_j + \vec{K}\vec{q}_j = \vec{Moment} \tag{5.12}$$

Equation 5.12 is constructed for nine degrees of freedom, with q being addressed in equation 5.13 and the derivative $\dot{q}$ in equation 5.14. After the Lagrangian is compiled and the partial derivatives of this Lagrangian for every variable in equations 5.13 and 5.14 is taken, nine equations of motion remain. These equations of motions are depicted in matrix form below. Given that the system has nine degrees of freedom, the mass, stiffness and damping matrix end up being $9x9$ matrices.

$$\vec{q} = \begin{bmatrix} u \\ \theta_1 \\ \theta_2 \\ \theta_3 \\ \theta_4 \\ \theta_5 \\ \theta_6 \\ \theta_7 \\ \theta_8 \end{bmatrix} \tag{5.13}$$

$$\dot{\vec{q}} = \begin{bmatrix} \dot{u} \\ \dot{\theta}_1 \\ \dot{\theta}_2 \\ \dot{\theta}_3 \\ \dot{\theta}_4 \\ \dot{\theta}_5 \\ \dot{\theta}_6 \\ \dot{\theta}_7 \\ \dot{\theta}_8 \end{bmatrix} \tag{5.14}$$

$$
\vec{M} = \begin{bmatrix}
2M_2 + 2M_3 + 2M_4 + M_G & 0 & 2M_4d - M_2(L_2 - 2d) - M_3(2L_2 - 2d) & -L_3M_3 & L_4M_4 & 0 & 0 & 0 & 0 & 0 \\
0 & L_1^2(M_2 + M_3 + M_4 + M_G) & 0 & 0 & 0 & 0 & 0 & 0 & 0 & 0 \\
2M_4d - M_2(L_2 - 2d) - M_3(2L_2 - 2d) & 0 & (L_2^2M_2)/12 + 2M_4d^2 + 2M_3(L_2 - d)^2 + 2M_2(L_2/2 - d)^2 & L_3M_3(L_2 - d) & L_4M_4d & L_1M_3(L_2 - d) - L_1M_4d + L_1M_2(L_2/2 - d) & (L_2^2M_2)/12 + M_4d^2 + M_3(L_2 - d)^2 + M_2(L_2/2 - d)^2 & L_1L_3M_3/2 - L_1L_4M_4/2 & (L_3M_3(L_2 - d))/2 & (L_4M_4d)/2 \\
-L_3M_3 & 0 & L_3M_3(L_2 - d) & (7L_3^2M_3)/12 & 0 & (L_1L_3M_3)/2 & (L_3M_3(L_2 - d))/2 & (7L_3^2M_3)/12 & 0 & 0 \\
L_4M_4 & 0 & L_4M_4d & 0 & (7L_4^2M_4)/12 & -(L_1L_4M_4)/2 & (L_4M_4d)/2 & 0 & 0 & (L_4^2M_4)/3
\end{bmatrix}
\tag{5.15}
$$

$$
\vec{K} = \begin{bmatrix}
K_1 \\
0 \\
0 \\
0 \\
0 \\
0 \\
0 \\
0 \\
0
\end{bmatrix}
\begin{bmatrix}
0 \\
R_1 + R_2 + L_1g(M_2 + M_3 + M_4 + M_G) \\
-R_2 \\
0 \\
0 \\
0 \\
0 \\
0 \\
0
\end{bmatrix}
\begin{bmatrix}
0 \\
-R_2 \\
R_2 + R_3 + R_4 \\
-R_3 \\
-R_4 \\
0 \\
0 \\
0 \\
0
\end{bmatrix}
\begin{bmatrix}
0 \\
0 \\
-R_3 \\
R_3 \\
0 \\
0 \\
0 \\
0 \\
0
\end{bmatrix}
\begin{bmatrix}
0 \\
0 \\
-R_4 \\
0 \\
R_4 \\
0 \\
0 \\
0 \\
0
\end{bmatrix}
\begin{bmatrix}
0 \\
0 \\
0 \\
0 \\
0 \\
R_5 + L_1g(M_2 + M_3 + M_4 + M_G) \\
0 \\
0 \\
0
\end{bmatrix}
\begin{bmatrix}
0 \\
0 \\
0 \\
0 \\
0 \\
0 \\
R_6 + R_7 + R_8 \\
-R_7 \\
-R_8
\end{bmatrix}
\begin{bmatrix}
0 \\
0 \\
0 \\
0 \\
0 \\
0 \\
-R_7 \\
R_7 \\
0R_8
\end{bmatrix}
\begin{bmatrix}
0 \\
0 \\
0 \\
0 \\
0 \\
0 \\
-R_8 \\
0 \\
\end{bmatrix}
\tag{5.16}
$$

$$\vec{B} = \begin{bmatrix} B_{11} & B_{12} & B_{13} & B_{14} & B_{15} & B_{16} & B_{17} & B_{18} & B_{19} \\ B_{21} & B_{22} & B_{23} & B_{24} & B_{25} & B_{26} & B_{27} & B_{28} & B_{29} \\ B_{31} & B_{32} & B_{33} & B_{34} & B_{35} & B_{36} & B_{37} & B_{38} & B_{39} \\ B_{41} & B_{42} & B_{43} & B_{44} & B_{45} & B_{46} & B_{47} & B_{48} & B_{49} \\ B_{51} & B_{52} & B_{53} & B_{54} & B_{55} & B_{56} & B_{57} & B_{58} & B_{59} \\ B_{61} & B_{62} & B_{63} & B_{64} & B_{65} & B_{66} & B_{67} & B_{68} & B_{69} \\ B_{71} & B_{72} & B_{73} & B_{74} & B_{75} & B_{76} & B_{77} & B_{78} & B_{79} \\ B_{81} & B_{82} & B_{83} & B_{84} & B_{85} & B_{86} & B_{87} & B_{88} & B_{89} \\ B_{91} & B_{92} & B_{93} & B_{94} & B_{95} & B_{96} & B_{97} & B_{98} & B_{99} \end{bmatrix} \quad (5.17)$$

$$\vec{Moment} = \begin{bmatrix} \frac{\partial W}{\partial u} \\ \frac{\partial W}{\partial \theta_1} \\ \frac{\partial W}{\partial \theta_2} \\ \frac{\partial W}{\partial \theta_3} \\ \frac{\partial W}{\partial \theta_4} \\ \frac{\partial W}{\partial \theta_5} \\ \frac{\partial W}{\partial \theta_6} \\ \frac{\partial W}{\partial \theta_7} \\ \frac{\partial W}{\partial \theta_8} \end{bmatrix} \quad (5.18)$$

The forces conducting the work in the blade model is a combination of three forces in the horizontal plane. These forces are subdivided in their x- and y-components. The summation of the work done by these six components is too long to display. The partial derivatives of the work over the degrees of freedom q_i will result in a moment matrix to complete the equations of motion as depicted in equation 5.12 and these are likewise the total work equation too long to display. Therefore the moment matrix in equation 5.18 is rendered differently.

5.4. Parameters

The blade segment characteristics in table 5.1 are obtained by the scaling assessment conducted in section 3.2.1 and by taking the DTU FFA-W3 blade series mentioned in literature of the IEA as a reference [29]. The total blade length was determined at 131.5 m. IEA did not give accurate information on blade characteristics of local coordinates but provided graphs of blade stiffness, mass density and prebend on a global scale, in which the blade root is depicted on the left of the chart. These graphs were analysed with as much precision as possible. Because the blade is divided in three segments, the graphs were similarly analysed in three segments. To make the analysis as accurate as possible, the graphs were divided in reasonably linear sections. The first section extends from the blade root to r/R-ratio of 0.2, the second section stretches from r/R-ratio 0.2 to 0.6 and the third section spans between r/R-ratio 0.6 and 1. The distributions result in the values for length, stiffness and mass per section shown in table 5.1. Summing up the masses of all segments delivers a total blade mass of 89.42 tonnes. As mentioned in section 2.7.3, the blade yoke or gripper connected to the blade has an estimated weight of twice the blade mass [37]. The blade yoke has a weight of around 179 tonnes.

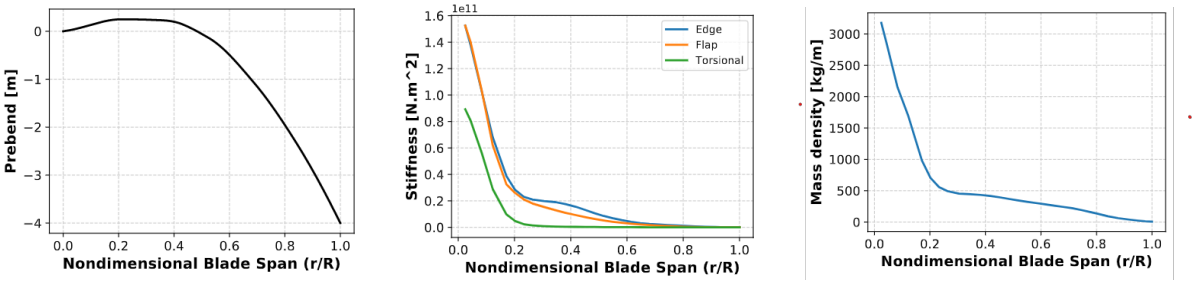

(a) (b) (c)

Figure 5.4: Global blade characteristics.

It must be noted that the scale on the graphs is small and therefore misreading the curves by a millimeter can cause large deviations from the actual value plotted. This is another apparent limitation of the model and a recommendation regarding this is provided in section 7.2.

After establishing the length, stiffness and mass density per section, the values of the rotational springs should be specified. Similarly to section 4.5, this was accomplished by a simplified wind turbine blade model resembling a conventional beam model with acquainted deflection and natural frequency equations. Figure 5.5a represents this simplified wind turbine blade model as a free-free beam hinged in coordinate 1.

The system is examined at steady-state and the forces F_{left} and F_{right} are balanced as such that the system is in equilibrium. This is accompanied by the fact that the angle the beam measures with the horizontal and the deflection are zero in coordinate 1.

This coincides with the properties of a cantilever beam as in figure 5.5b. When a model like the free body diagram depicted in figure 5.5a is in steady-state condition, it can be paralleled by two cantilever beams. One cantilever beam, a mirrored copy of figure 5.5b, stretches from coordinate 1 to the left tip, the other from coordinate 1 to the right tip, each with the boundary conditions of a cantilever beam at coordinate 1. The boundary conditions at coordinate x_1 are displayed in equations 5.19 and 5.20.

$$u(x_1) = 0 \tag{5.19}$$

$$u'(x_1) = \theta(x_1) = 0 \tag{5.20}$$

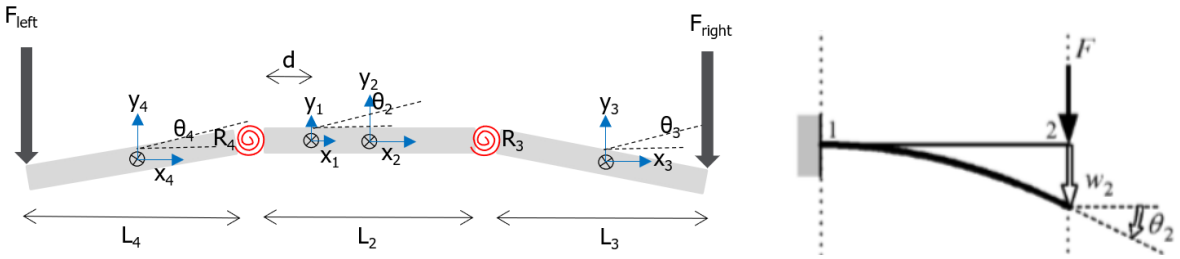

(a) Free body diagram of system being measured against conventional cantilever beam.

(b) Cantilever beam.

Figure 5.5: Wind turbine blade stiffness check configuration.

A necessary simplification of the wind turbine blade model is a uniform cross-section along the full length of the beam. This also results in a uniform stiffness. The deflection of both beam endings in the simplified beam model should correspond to the results of equation 5.21.

$$\begin{aligned} u(x_{tip}) &= \frac{F_{right}\,(L_2 + L_3 - d)^3}{3EI} \\ u(x_{root}) &= \frac{F_{left}\,(L_4 + d)^3}{3EI} \end{aligned} \tag{5.21}$$

Since the beams are rigid and coordinate 1 is hinged which prevents vertical displacement, the deflection is constrained by the rotational stiffness of the spring. The rotational stiffness of both springs shown in figure 5.5a is EI/L multiplied with a factor, in which the factor is the only adjustable parameter. The factor is numerically determined until the deflection and first natural frequency of both cantilever beams correspond to all parameters of the blade model.

This so-called fudge-factor is numerically determined and is 0.589 and 1.641 for respectively R_3 and R_4. R_2 is a rotational stiffness and represents the stiffness of the cable-blade connection, also know as a gripper or lifting yoke, counteracting a pitch motion. It can be retrieved from figure 5.1 where the spring is positioned, namely the center of gravity of the entire blade. The rotational stiffnesses R_3 and R_4 determined above are in the flapwise plane, it is assumed that the determined fudge-factors are the same for the edgewise rotational stiffnesses. The resulting stiffnesses in edgewise and flapwise direction differ because the graph in figure 5.4b shows different values of stiffness per unit length of the blade in the two planes. Section 2.7 elaborates more on the properties of several lifting yokes and taglines.

A problem that has surfaced is the failure to achieve equal natural frequencies when comparing the frequencies of the model to those of a cantilever beam. This may be due to incorrect assumptions in simplifying the model or because the comparison with a cantilever beam is incorrect. This problem was abandoned because the final rotational stiffness of the blade depends on so many assumptions, including

the reading of small graphs shown in figure 5.4. It is also expected that the internal rotational stiffness of the blade will not contribute to large rotations and deflections of the blade in the steady-state regime.

Table 5.1 also contains the cable characteristics with subscript 1, not to be confused with coordinate 1. The cable characteristics are obtained from the Allseas Engineering database [66]. The length of the cable varies a lot during a lift operation, as a blade is hoisted from a deck to hub height. This thesis focuses on the mating process only and therefore the distance between the crane boom tip and the center of gravity of the blade is a constant during modelling, namely L_1.

However, the cable length is an important parameter since it determines the natural frequency of the pendulum motion according to equation 5.22. Additionally, the rotational stiffness of the cable, R_6 is affected by the length of the hoist cable. This is shown in equation 5.23. The importance of these parameters is emphasised in section 5.7. In this section, the results of simulations with different cable lengths are listed.

$$\omega_n = \sqrt{\frac{g}{L_1}} \tag{5.22}$$

$$R_6 = \frac{G\,J}{L} \tag{5.23}$$

The material damping is introduced as modal damping. But the aerodynamic is implemented by taking the velocity of the wind relative to the blade. The Rayleigh dissipation function is used again for determining the material damping by applying equation 4.36 to 4.38. The difference is that the blade model consists of nine degrees of freedom, resulting in the matrices of the modal mass, the mass, the critical damping and the total damping being 9x9 matrices. The damping coefficients used are listed in table 5.1 if non-zero. Table 5.17 suggest that every entry is non-zero, but some entries certainly are. Matrix 5.24 elaborates on this, the entries that are non-zero alternate due to varying damping coefficient inputs.

For a more comprehensive explanation on how to determine the damping matrix, see section 4.5. The above mentioned aerodynamic damping should not be confused with the damping that comes from the rotor turning when the turbine is in operation as the wind turbine is not in operation yet and the blades are yet to be installed.

$$\vec{B} = \begin{bmatrix} B_{11} & 0 & 0 & 0 & 0 & 0 & 0 & 0 & 0 \\ 0 & B_{22} & B_{23} & B_{24} & B_{25} & 0 & 0 & 0 & 0 \\ 0 & B_{32} & B_{33} & B_{34} & B_{35} & 0 & 0 & 0 & 0 \\ 0 & B_{42} & B_{43} & B_{44} & B_{45} & 0 & 0 & 0 & 0 \\ 0 & B_{52} & B_{53} & B_{54} & B_{55} & 0 & 0 & 0 & 0 \\ 0 & 0 & 0 & 0 & 0 & B_{66} & B_{67} & B_{68} & B_{69} \\ 0 & 0 & 0 & 0 & 0 & B_{76} & B_{77} & B_{78} & B_{79} \\ 0 & 0 & 0 & 0 & 0 & B_{86} & B_{87} & B_{88} & B_{89} \\ 0 & 0 & 0 & 0 & 0 & B_{96} & B_{97} & B_{98} & B_{99} \end{bmatrix} \tag{5.24}$$

To make the models as much akin to reality as possible under current assumptions, the prebend characteristic of the blade is added. The initial condition of the degrees of freedom of the beam model is such that the prebend matches the blade described in section 3.2.4. Although, at this point, the gravitational force has not yet taken effect. Approaching the steady-state solution, after the gravitational force is enacted, the actual prebend of the blade during lift operation can be identified. The actual prebend of both tips (segments 3 and 4) can be found in table 5.1.

If the initial value of θ_6 is zero, the blade will have a significant angle with the x-axis in the steady-state regime. To counter this effect and ensure positioning between hub and blade root an initial angle of θ_6 is introduced. This initial angle depends the weather conditions, damping coefficients and rotational stiffnesses of the model. The value of θ_6 listed in table 5.1 is the value associated with most favourable circumstances resulting from the sensitivity analysis conducted in section 5.7.

Table 5.1: Parameters wind turbine blade model situation 1, figure 5.1.

Parameter	unit	Value		
g	m/s^2	9.81		
$U_{mean,\,wind}$	m/s	7 - 11 - 20		
β_3	-	45°		
L	m	131.5		
L_{cable}	m	10		
ρ_{air}	kg/m^3	1.225		
$C_{D,wind}$	-	0.7		
M_{blade}	kg	$89.42 * 10^3$		
M_G	kg	$179 * 10^3$		
K_1	Nm	$2.36 * 10^6$		
ζ_1	-	0		
ζ_2	-	0		
ζ_3	-	0		
ζ_4	-	0		
ζ_5	-	0.005		
ζ_6	-	0.005		
ζ_7	-	0.005		
ζ_8	-	0.005		
ζ_9	-	0.005		
R_1	Nm	0		
R_2	kNm	100		
R_5	Nm	0		
R_6	kNm	157		
Blade segment characteristics				
j	-	2	3	4
L_j	m	52.6	52.6	26.3
$Blade\ height_j$	m	1.75	0.56	3.75
A_j	m^2	98.63	92.05	29.46
M_j	kg	$26.3 * 10^3$	$10.52 * 10^3$	$52.6 * 10^3$
$Prebend_j$	m	-	5.62	0.19
$flapwise\ R_j$	Nm/rad	-	$6.72 * 10^7$	$3.74 * 10^9$
$edgewise\ R_j$	Nm/rad	-	$7.35 * 10^7$	$4.26 * 10^9$

5.5. Natural frequencies

After determining the matrices $\vec{K}$ and $\vec{M}$ for the blade in the configuration of situation one, the natural frequencies can be calculated once more with the help of equation 4.43. The results are listed below in table 5.2, including the types of mode shape. The mode shapes are plotted and displayed in appendix F by determining the Eigenvectors with the help of the Eigenvalue problem. The Eigenvectors are the entries of the degrees of freedom to create nine mode shapes. Applying the square root to the Eigenvalues is a different method to determine the natural frequencies.

Table 5.2: Natural frequencies of offshore wind turbine blade in $z-x$ plane.

-	ω	f	T	mode
$unit$	rad/s	Hz	s	-
1	0.0238	0.0038	263.63	pitch
2	0.0403	0.0064	155.81	yaw
3	0.9961	0.1585	6.31	$z-x$ pendulum
4	1.0009	0.1593	6.30	$z-y$ pendulum
5	2.99	0.48	2.10	1^{st} flapwise blade
6	6.69	1.07	0.94	cable elongation
7	14.47	2.30	0.43	1^{st} edgewise blade
8	25.66	4.08	0.24	2^{nd} flapwise blade
9	101.96	16.23	0.06	2^{nd} edgwise blade

5.6. Forcing vector

The force F_{wind} mentioned in equation 5.25 is time-dependent. The force exerted on the wind turbine blade depends on the wind velocity and the velocity of the blade, the relative velocity. The wind velocity used throughout this thesis is a time series function and is equal to the wind velocity the wind turbine support structure is subjected to. This is discussed in section 4.7. For the exact derivation of the wind velocity profile, view section 4.7.

$$F_{wind,i}(t) = \frac{1}{2}\, C_{drag}\, \rho_{air}\, A_{blade,i}(t)\, \left(U_{wind}(t) - U_{segment,i}(t)\right)\, \left|U_{wind}(t) - U_{segment,i}(t)\right| \tag{5.25}$$

The wind forces displayed in figure 5.6 are formulated as shown in equation 5.25. As mentioned in equation 5.10, the wind forces are subdivided in x- and y-components. The wind force is time-dependent because of its dependence on the wind velocity. The area of is determined by assuming that the individual segments are uniform and therefore have an equal cross-section over the length, thus the cross-section multiplied by the length of a segment results in the area $A_{blade,i}$. In the configuration below, the x-component of the force is parallel to the blade resulting in a drag force of zero. The y-component of the force is perpendicular to the blade, resulting in a drag force. If the blade rotates in the horizontal $x-y$ plane, the x-component of the force will become non-zero as it is not parallel to the blade anymore. The area subject by the force evolves along with the rotation, resulting in equations 5.26 and 5.27, respectively the areas seen by the x- and y- component of any wind force. These equations can also be distinguished in equation 5.10. In the equations below, the subscript i represents 1, 2 and 3 and the subscript j represents 6, 7 and 8.

$$A_{x,i}(t) = A_{blade,i}\, \theta_j \tag{5.26}$$

$$A_{y,i}(t) = A_{blade,i} \left(1 - \frac{\theta_j^2}{2}\right) \tag{5.27}$$

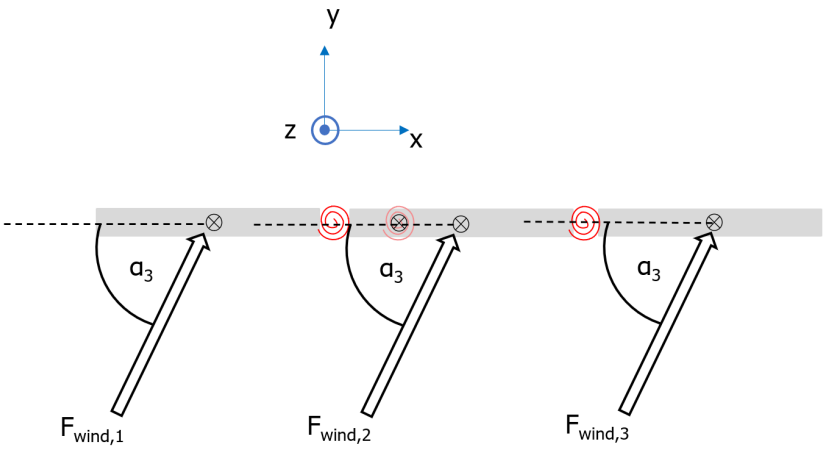

Figure 5.6: Wind forces acting on blade.

5.7. Blade Results and Sensitivity Analysis

In this section, the impact of some input parameters described in section 5.4 are investigated. The deflections and velocities mentioned in this section are associated with the blade root.

Some results are plotted in appendix F to support the results listed in this section.

5.7.1. Wind conditions

The three different sea-states investigated in previous chapter are accompanied with three different mean wind velocities. The mean wind input is altered similarly in this section. Table 5.3 lists the three different weather conditions used as input, together with the maximum value of the crane boom tip motions and velocities during the conducted simulations of 1000 seconds.

Table 5.3: Maximum deflections and velocities of support structure in different sea-states.

	Unit	Calm	Normal	Rough
Mean wind velocity	[m/s]	6.96	10.96	19.96
Standard deviation	[m/s]	0.85	0.85	0.85
Minimum wind velocity	[m/s]	4.38	8.38	17.38
Maximum wind velocity	[m/s]	9.0	13.0	22.0
Maximum wind force	[kN]	11.7	20.4	39.9
Maximum yaw moment	[kNm]	28.8	60.0	172.7

Table 5.4 contains the magnitude of the velocity of the blade root for varying input parameters listed in table 5.3. The determination of this mean wind velocity is elaborated on in section 4.8. No mitigations are applied to the model.

Table 5.4: Mean deflections and max velocities of wind turbine blade root excited by different mean wind velocities.

	Unit	Calm	Normal	Rough
Mean Deflection	[m]	8.61	16.46	25.28
Ratio	[-]	-	+91.2%	+193.6%
Velocity	[m/s]	0.124	0.112	0.147
Ratio	[-]	-	-9.7%	+18.5%
Mean Angle	[-]	13.77°	25.89°	38.74°

5.7.2. Wind angle

In this section, different angles of incidence of the wind on the blade are examined. This analysis could be used to determine the angle to the wind in the horizontal plane at which blade installation is preferable. The nacelle can rotate around the z-axis, therefore any angle in the horizontal plane could be achieved to provide favourable conditions during installation.

Table 5.5: Wind angle of incidence variation sensitivity analysis of blade root motions.

Incidence angle [-]	Mean Deflection [m]	Ratio [-]	Max Velocity [m]	Ratio [-]	Mean Angle [-]
0°	6.37	-26.0%	0.099	-20.2%	10.20°
45°	8.61	-	0.124	-	13.77°
90°	6.34	-26.4%	0.104	-16.1%	10.18°

5.7.3. Drag coefficient

In this section, the drag coefficient of the wind force is alternated. The range is based on possible Reynolds numbers that result in different drag coefficients. Small wind turbines usually operate at a Reynolds number less than $5 * 10^5$, but the FFA-W3 aerofoil used for both reference wind turbines discussed in this report operate at a Reynolds number of approximate 10^7 [67, 29]. Appendix C.4 elaborates on the dependence of the drag coefficient on the Reynolds number. It is concluded that a Reynolds number of 10^7 is accompanied by a varying drag coefficient of 0.6 up to 0.9.

Table 5.6: Drag coefficient variation sensitivity analysis of blade root motions.

C_D [-]	Mean Deflection [m]	Ratio [-]	Max Velocity [m]	Ratio [-]	Mean Angle [-]
0.6	7.54	-12.4%	0.117	-5.6%	12.08°
0.7	8.61	-	0.124	-	13.77°
0.8	9.62	+11.7%	0.130	+4.8%	15.35°
0.9	10.57	+22.8%	0.135	+8.9%	16.83°

For further simulations, a drag coefficient of 0.7 is assumed.

5.7.4. Cable length

A variation in hoist cable length is examined. The length of the cable determines the natural frequency of the pendulum motions of the blade, as shown in equation 5.22. When changing the cable length, only the pendulum motion frequency is significantly affected. Another parameter that is affected by the cable length is the rotational stiffness of the cable, equation 5.23 depicts this. Table 5.7 gives the result of varying the cable length. A cable length of 10 m is used as the base case and calm weather conditions are used throughout this analysis.

Table 5.7: Cable length variation sensitivity analysis of blade root motions.

Length [m]	Mean Deflection [m]	Ratio [-]	Max Velocity [m/s]	Ratio [-]	Mean Angle [-]
10	8.61	-	0.124	-	13.77°
15	11.88	+38.0%	0.160	+29.0%	18.83°
23	15.77	+83.2%	0.136	+9.7%	24.73°

It would be expected that for a longer cable, the deflections of a pendulum increase but the velocities increase. This cannot be concluded from the results in table 5.7, but the blade model is not solely a pendulum, as the yaw motion impacts the results greatly. To emphasise the effect of a longer cable on a pendulum motion, the maximum deflections and velocities of the center of gravity of the blade are listed as well in table 5.8. These results are as expected.

Table 5.8: Cable length variation sensitivity analysis of blade centre of gravity motions.

Length [m]	Mean Deflection [m]	Ratio [-]	Max Velocity [m/s]	Ratio [-]
10	0.063	-	0.007	-
15	0.113	+79.4%	0.006	-14.3%
23	0.125	+98.4%	0.004	-42.9%

It can be concluded that a shorter cable length is beneficial for decreasing the blade motions in this model. It is assumed that the cable length is 10 m in every following result.

5.7.5. Damping

In this section, impact of material damping is investigated. The aerodynamic damping cannot be adjusted as this type of damping originates from the wind velocity relative to the blade only. The material damping does mainly affect the mode shapes belonging to the cable elongation, second and third blade mode shapes. Adding damping to the system can be done by assuming taglines. A tagline does not have an impact on the aforementioned mode shapes, but it affects the yaw and pendulum mode shapes of the blade. To assess the influence of a tagline, damping coefficients ζ_2, ζ_3 and ζ_4 are alternated collectively. The other parameters considered are set at the base case values, listed in table 5.1.

Table 5.9: Damping coefficient variation sensitivity analysis of blade root motions.

Coefficient [-]	Mean Deflection [m]	Ratio [-]	Max Velocity [m]	Ratio [-]	Mean Angle [-]
0	8.61	-	0.124	-	13.77°
0.01	8.61	0%	0.121	-2.4%	13.76°
0.02	8.61	0%	0.119	-4.0%	13.76°
0.03	8.61	0%	0.117	-5.6%	13.75°
0.05	8.61	0%	0.112	-9.7%	13.72°

It is concluded that damping has an significant impact on the model simulated in this chapter.

5.7.6. Gripper mass

The gripper mass is varied to analyse its counter effect to wind. With a heavier gripper or blade yoke, the mean deflection of the blade caused by the wind is expected to decrease. The gripper mass was first established at two times the blade mass [37]. This gripper mass is varied with an amplitude of 20%.

Table 5.10: Gripper or blade yoke mass variation sensitivity analysis of blade root motions.

M_G [tonnes]	Mean Deflection [m]	Ratio [-]	Max Velocity [m]	Ratio [-]
0	8.59	-0.2%	0.129	+4.0%
143.2	8.61	0%	0.124	0%
179	8.61	-	0.124	-
214.8	8.61	0%	0.124	0%

It can be concluded that the gripper mass has little impact on the blade root motions. What isn't depicted in table 5.10 is the influence a varying gripper mass has on the blade's center of gravity motions, which are substantial, but not important for this research. Nevertheless, a table with the centre of gravity motions is included in this section to show the impact of a gripper or blade yoke.

Table 5.11: Gripper or blade yoke mass variation sensitivity analysis of blade centre of gravity motions.

M_G [t]	Mean Deflection [m]	Ratio [-]	Max Velocity [m]	Ratio [-]
0	0.098	%	0.017	+142.9%
143.2	0.065	+3.2%	0.008	+14.3%
179	0.063	-	0.007	-
214.8	0.060	-4.8%	0.007	0%

5.7.7. Initial angle

It can be concluded from all blade simulation results above, that the blade takes on a new mean angle relative to the x-axis. The sensitivity analysis in this section examines the results of a blade simulation with an initial yaw angle of the blade, which is the exact mean angle of the simulation with an blade alignment with the x-axis. The results in table 5.12 show that the equilibrium positions of the blade in different weather conditions are not affected significantly by an initial yaw angle. The small deviation in blade root mean deflection is negligible compared to the initial angle.

Table 5.12: Wind angle of incidence variation sensitivity analysis of blade root motions.

Weather conditions	Initial angle [-]	Mean Deflection [m]	Mean Angle [-]
Calm	0°	8.61	13.77°
Calm	13.77°	8.55	13.77°
Normal	0°	16.46	25.89°
Normal	25.89°	16.27	25.89°
Rough	0°	25.28	38.74°
Rough	38.74°	24.68	38.74°

5.7.8. Z-component

In this section, the motions of the blade root in the three weather conditions are observed again. Table 5.13 lists the deflections compared to the initial position and velocities in z-direction.

Table 5.13: Maximum deflections and velocities in z-direction of blade root in different sea-states.

	Unit	Calm	Normal	Rough
Velocity	[m/s]	0.062	0.043	0.093

The results show that the influence of the z-velocity cannot be disregarded during installation. The pitch motion of the blade, with a period of 263.6 seconds, is the main cause of the constantly changing z-position.

6

Combined Model

6.1. Model introduction

In this chapter, the results of the 3D blade model and the 3D support structure model are merged, resembling the third-to-last part of the blade installation phase, namely the positioning of the blade relative to the hub before mating and boltening the blade to the hub.

Figures 6.1 and 6.2 give an visual impression of this merger, where it must be noted that figure 6.1 does not indicate that the forces act only in the x-direction, as figure 6.2 supports. When positioning and mating a blade, the two objects are slowly brought towards each other from a small distance, thus an initial distance of 0.10 metres is assumed. However, this does not impact the actual result of this chapter, the relative velocity.

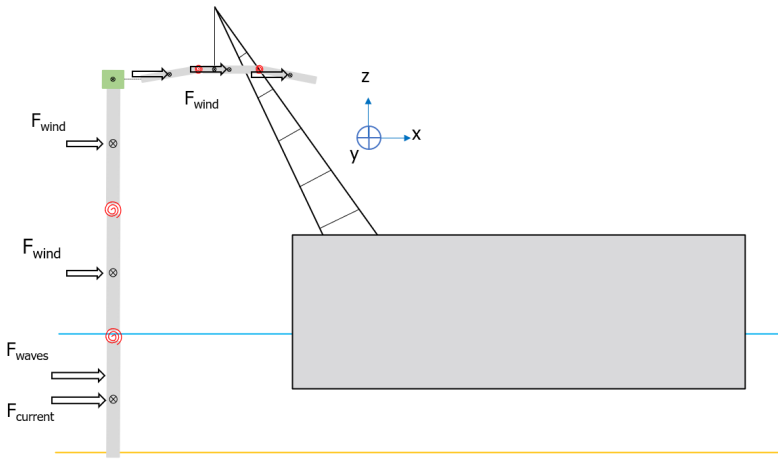

Figure 6.1: Blade installation with floating vessel overview in the $z-x$ plane (side view).

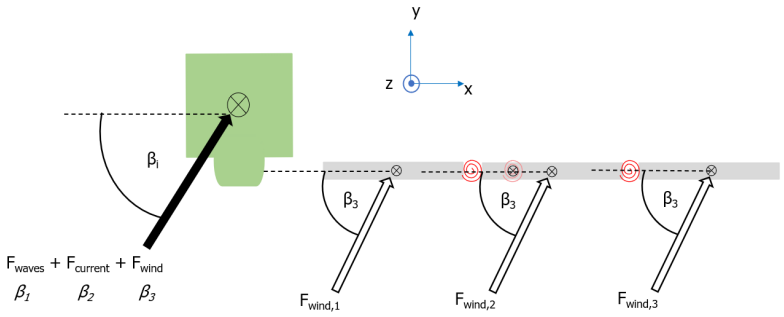

Figure 6.2: Top view of forces acting on wind turbine support structure and blade.

Figures 6.1 and 6.2 indicate where the point of action of the forces are located. A very important parameter of these forces are the angle of incidence of the forces. β_1 belongs to the time-dependent unidirectional wave force, β_2 belongs to the unidirectional current force and β_3 belongs to the unidirectional time-dependent wind force. The value of β_1 and β_2 is 30°and the value of β_3 is 90°. This is visualised in figure 6.3.

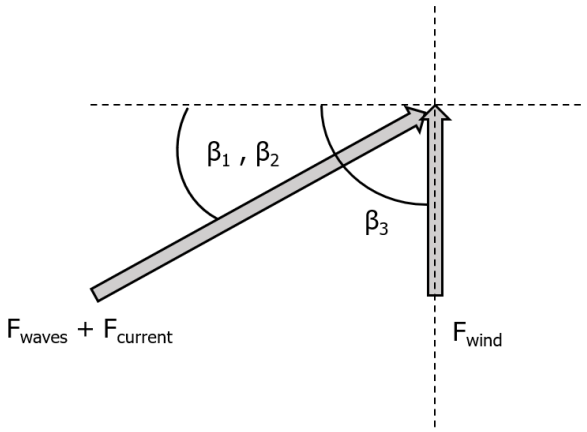

Figure 6.3: All forces acting on wind turbine support structure and blade with their independent angles.

6.2. Case studies

Several case studies have been established to investigate the impact of optimising some parameters on the relative motions. In the previous chapters, the velocity of a structure relative to environmental forces was discussed. In this chapter, the relative motions indicate the blade motion relative to the support structure motion, more specifically the hub motions. The case studies are determined by taking into account the sensitivity analyses of the previous chapters. All parameters discussed in the sensitivity analyses are mentioned in table 6.1. The damping coefficient of the support structure that is varied, strictly focuses on the two 1^{st} support structure mode shapes. The damping coefficient of the blade model that is varied, strictly focuses on the yaw mode shape and the two pendulum modeshapes. All other mode shapes are unaffected. The other parameters that are not alternated in the sensitivity analyses are located in tables 4.1 and 5.1. Case 1 is the base case, identical to the base cases used in the sensitivity analyses, apart from the angle of incidence on the support structure. Case 2 includes achievable mitigations, which consists of damping. The remaining four cases emphasise the effect of the mitigations on normal and rough weather conditions.

The case studies are listed in table 6.1 and the results of the various simulations can be found in table 6.2. The characteristics of calm, normal and rough weather conditions are shown in table 4.6.

Table 6.1: Case studies of combined simulation model.

	Unit	Case 1	Case 2	Case 3	Case 4	Case 5	Case 6
Weather conditions	[-]	Calm	Calm	Normal	Normal	Rough	Rough
Wind angle	[-]	45°	45°	45°	45°	45°	45°
Wave and current angle	[-]	30°	30°	30°	30°	30°	30°
Drag coefficient	[-]	0.7	0.7	0.7	0.7	0.7	0.7
Cable length	[m]	10	10	10	10	10	10
$\zeta_{damping}$ support structure	[-]	0.005	0.055	0.005	0.055	0.005	0.055
$\zeta_{damping}$ blade	[-]	0	0.03	0	0.03	0	0.03
R_6 (blade yaw)	$[kNm/rad]$	157	157	157	157	157	157
Nacelle mass	[tonnes]	1000	1000	1000	1000	1000	1000
Gripper mass	[tonnes]	179	179	179	179	179	179
Monopile diameter	[m]	11	11	11	11	11	11
Monopile wall thickness	[m]	0.08	0.08	0.08	0.08	0.08	0.08

6.3. Results: relative velocity

The relative motions per case are determined. The maximum relative velocity is assumed to be the potential maximum impact velocity between blade and hub and is displayed per case in table 6.2.

Table 6.2: Maximum relative impact velocities of blade and hub.

	Max impact velocity [m/s]	Ratio [-]
Case 1	0.207	-
Case 2	0.135	-34.8%
Case 3	0.476	-
Case 4	0.183	-61.6%
Case 5	0.534	-
Case 6	0.215	-59.7%

The damping that is added to the support structure and blade model resulted in a decrease of the blade root velocity and has a greater impact on more severe weather conditions. The decrease depicted as a percentage in table 6.2 supports this. It is concluded that installation cannot be accomplished in cases 1, 3, 5 and 6. The results of case 2 show that under certain normal circumstances installation might be feasible and the results of case 3 show that installation is very likely to be feasible in calm weather conditions. The relative velocities in x- and y-direction of the blade root in the mitigated cases 2, 4 and 6 are shown in figures 6.4, 6.5 and 6.6. It is difficult to define an exact value that cannot be exceeded to maintain installation feasibility. It is common practice to determine whether installation is still possible based on an evaluation of an on site engineer. An approximation of excessive blade behaviour is to determine how much energy is allowed in the relative motion between hub and blade, before any component becomes susceptible to damage. The kinetic energy of the blade root during a simulation is not determined in this study.

The values in the legends of the three figures below are the maximum velocities of the second half of the simulation, since then the simulation is in the steady-state regime. The first half is irrelevant when determining the maximum value during blade installation, because it is the transient-state of the simulation. Normally, the installation of a blade has a longer duration than the steady-state duration of the simulations displayed above. After 1000 seconds, the velocity profiles will become slightly repetitive and to display the profiles properly, a shorter time span was chosen.

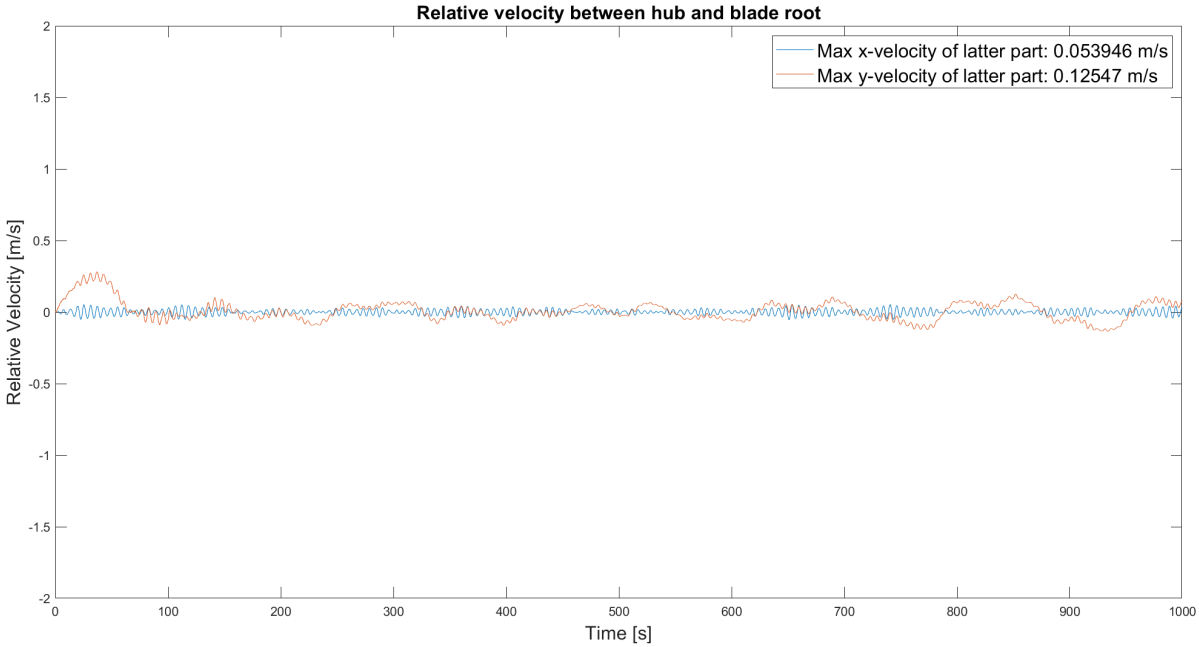

Figure 6.4: Case 2 results: x- and y-components of relative velocity between hub and blade root.

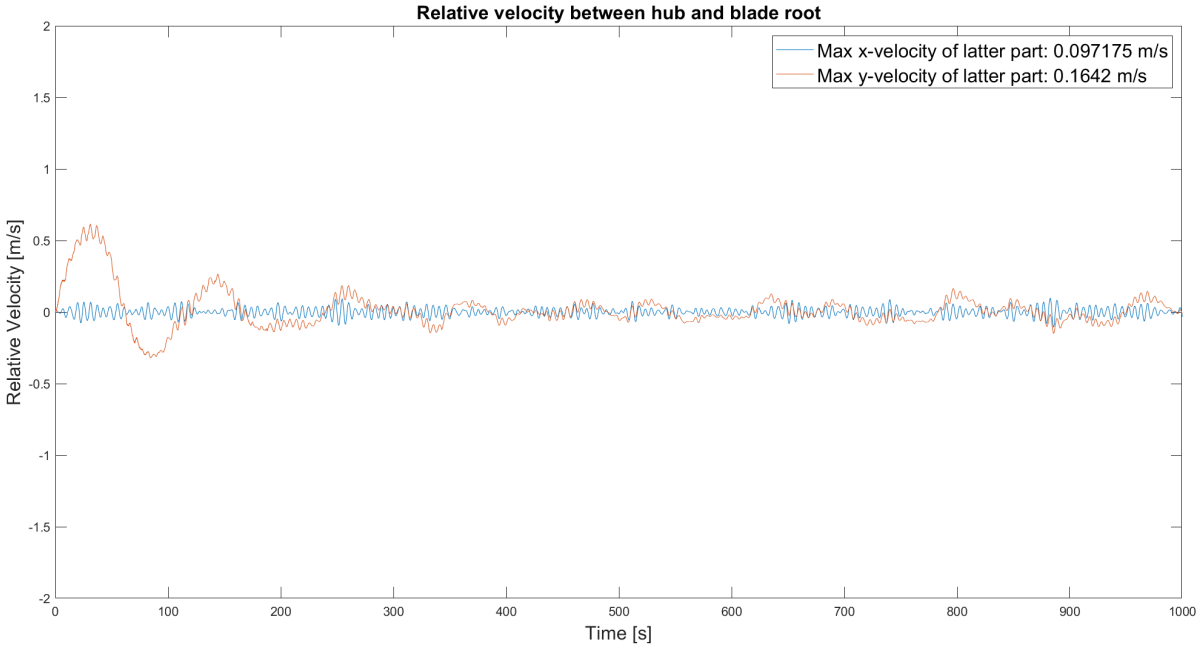

Figure 6.5: Case 4 results: x- and y-components of relative velocity between hub and blade root.

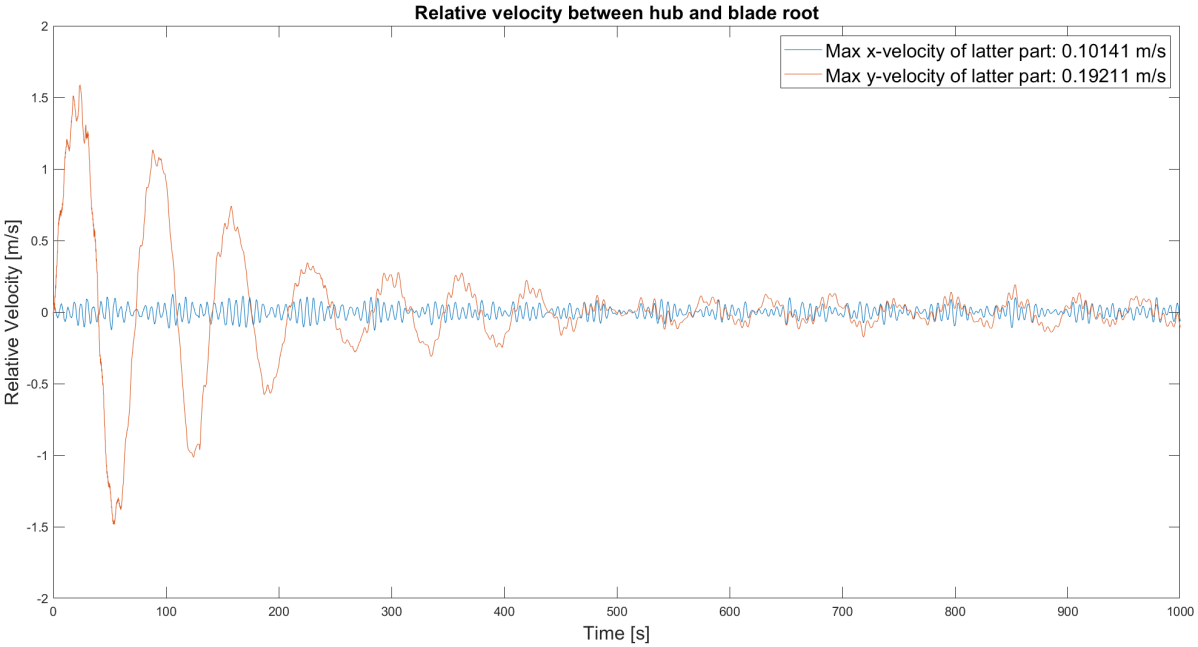

Figure 6.6: Case 6 results: x- and y-components of relative velocity between hub and blade root.

The x- and y-axis of the figures are equal, to properly reflect the increase of the velocity components when weather conditions worsen. It is concluded that the x-motion of the blade root is mainly the pendulum motion. The y-velocity is both the pendulum and yaw motion, which explains the greater values in the y-direction.

6.4. Results: relative motions

This research focuses on the positioning phase of a blade relative to the hub right before the mating phase starts. It is crucial that the components are aligned, but the yaw motion of the blade prevents this from happening. After the mitigations are applied, there will be an angle of the blade in the horizontal plane with the x-axis. This angle is mainly due to a force equilibrium and slightly due to the rotational resistance of the cable. This research helps to evaluate the angle of the blade under certain conditions. It is not possible to obtain an initial yaw angle to counter the deviation of the blade during the simulation, because the equilibrium of the resulting yaw angle is not affected by the initial angle, although it might be reached with a slight delay.

The yaw motion of the blade creates larger deflections than a pendulum motion only. The aforementioned mean angle in equilibrium has a corresponding mean blade root deflection. The mean deflections and angles are listed in table 6.3.

Table 6.3: Mean values of relative motions and angles.

	Mean distance [m]	Mean blade angle [-]
Case 1	8.39	13.16
Case 2	8.42	13.21
Case 3	16.34	25.86
Case 4	16.34	25.85
Case 5	25.28	38.80
Case 6	25.27	38.81

It is concluded that damping has no impact on the mean deflection and angle of the blade root. The mean angles and deflections do not pose an issue for installation feasibility. To accomplish the installation of a blade, the nacelle can yaw to achieve an alignment between the hub and blade and the position of the ship and crane could factor in the mean distance between the blade root and hub.

However, it must be considered that the blade may hit the crane by rotating into the crane boom. This must also be taken into account when positioning the ship with regard to the support structure before the installation phase begins. Figures 6.7, 6.8 and 6.9 display the distance between the hub and blade over time. The mean deflections are measured only in the latter half of the simulation.

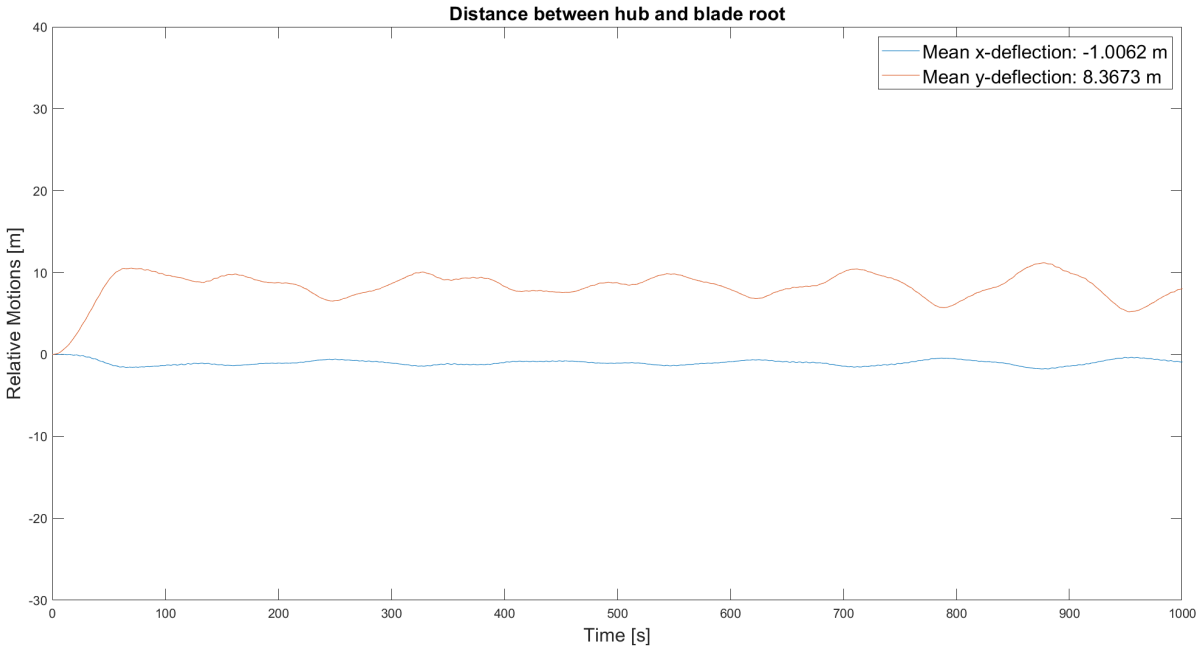

Figure 6.7: Case 2 results: x- and y-components of distance between hub and blade root.

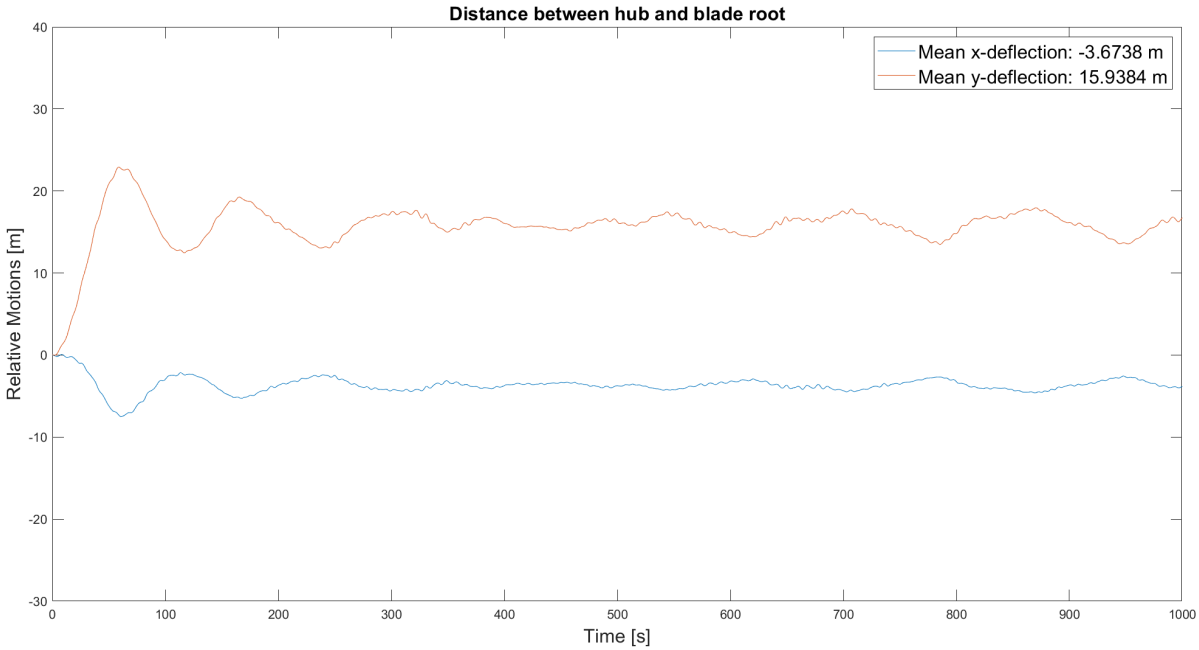

Figure 6.8: Case 4 results: x- and y-components of distance between hub and blade root.

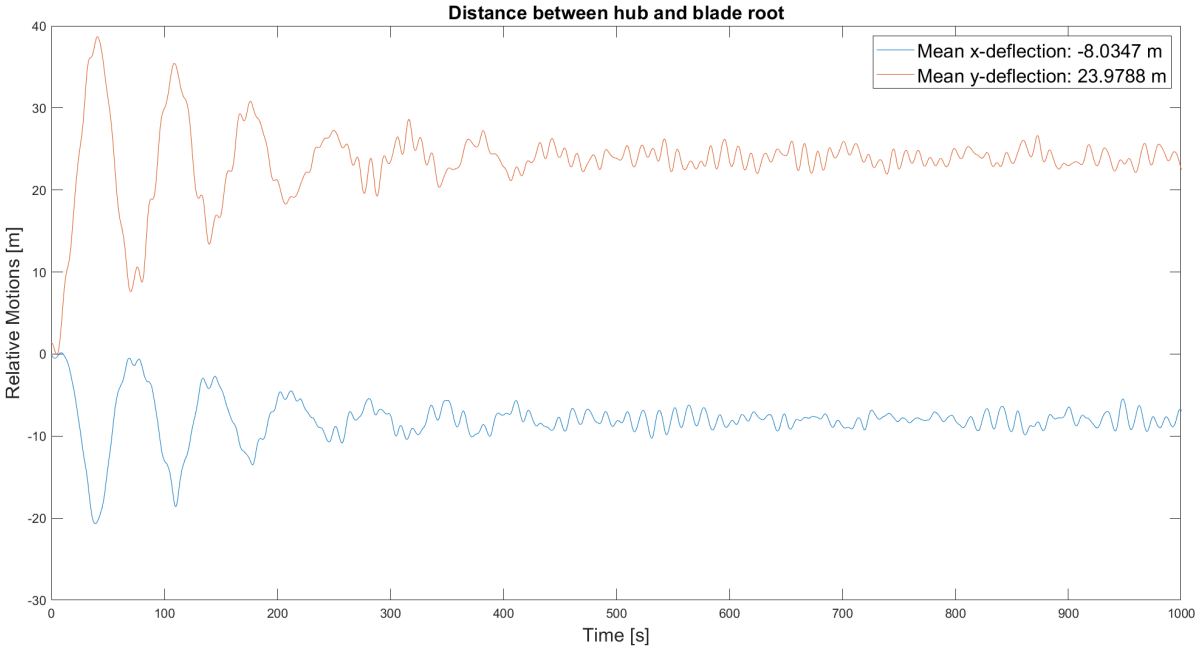

Figure 6.9: Case 6 results: x- and y-components of distance between hub and blade root.

The figures depict that in the transient-state, the blade quickly adapts to a mean deflection, the new equilibrium. A bit further in the simulation, a sinusoidal motion is clearly visible, representing the yaw motion of the blade. When the deflections become larger in more severe weather conditions, a static noise becomes visible. This is an effect caused by the crane boom tip motions.

7

Conclusions and Recommendations

7.1. Conclusions

The demand for renewable energy has expanded to the sea. Offshore wind turbines have significantly increased in size and power rating over the last decades to meet the energy demand. It is expected that in the near future a 20 MW wind turbine will be installed offshore. But first, the challenges associated with this growth must be overcome. To address some of the challenges, the following research question is addressed in this research:

"How can the motions of an offshore wind turbine nacelle-hub assembly and a rotor blade during installation be modelled and managed as to maximize weather workability?"

In the near future, projections show offshore wind turbines to scale up to 20 MW. After a scaling assessment was conducted, it could be concluded that the 20 MW wind turbine used in this study is estimated to have a hub height of 154.7 m and a blade length of 131.5 m with an estimated weight of slightly less than 90 tonnes. Due to the offshore placement of the wind turbine, the length of the support structure is estimated to extend with a monopile length of 35 m, due to the water depth. The support structure has a circular cross-section with a point mass on top, equivalent to a combined nacelle and hub weight of 1000 tonnes.

The unidirectional forces used in the models are originating from the waves, current and wind. The waves are based upon JONSWAP spectra with varying characteristics, the wind force is based on a wind spectrum of measured wind data with a mean wind velocity and by assuming a short simulation time span, the current becomes a constant force. The wave and wind forces are composed of multiple sine waves according to the principle of superposition. An advantage of assuming the forces to be unidirectional is that it allows the construction of an irregular wave and wind force in the time domain through the principle of superposition. An omni-directional force can be applied to the support structure with the preference that the system is analysed in the frequency domain.

A support structure with nacelle-hub assembly is modelled as a multi-body system consisting of three segments of which the lower segment is attached to the seabed. The first resonance frequency of the support structure is in the range of the wave and wind spectra containing spectral density, where especially the wave affects the structure's motions, although the motions will unlikely become too excessive for the operational stage of the wind turbine. In addition, movements in the z-direction are insignificant and disregarded in any analysis. The motions are mainly initiated by the waves, contributing more than 90% to the total overturning moment in the calm, normal and rough weather conditions considered in this thesis. The top mass has an unstable effect on the support structure, as it counteracts the restoring forces by pulling it out of the equilibrium position and causing additional deflection. The weight of the nacelle and hub decreases the first resonance frequency of the support structure, shifting it closer to the peak frequencies considered in the calm, normal and rough sea-states.

The second model discussed in this thesis is a multi-body system in which a blade is suspended from a crane mounted on a floating vessel. The blade is subjected to a wind velocity equal to the wind profile used in the support structure model. It is found that the dominant motion of the blade is the yaw motion around its centre of gravity, resulting in a constantly varying blade surface acted on by the varying wind force. Additionally, the pendulum motions of the blade cause minimal extra motions. The constant mean force component of the varying wind force, creates a new equilibrium position, reached in the steady-state regime of the simulation. The equilibrium is predominantly determined by the angle of incidence of the wind. The varying component of the wind force ensures that the blade continues to make a yaw motion. The crane boom tip is moving during the entire simulation, enhancing the blade motions. The movements of the crane are caused by it being located on a floating vessel, making the crane more susceptible to waves.

It is concluded that the motion of the centre of gravity of the blade is affected the most by the pendulum mode shapes of multi-body system. However, the motions of the blade root are of real importance, as the positioning of this component relative to the hub is an essential step during the blade installation.

After analysing the motions of both the support structure model and the blade model it was concluded that the z-motions are insignificant, although they are present. The most significant relative motions occur in the horizontal plane of the 3D simulations. The dominant yaw motions of the blade indicate that if an impact between hub an blade occurs, it will likely be in the lateral, not longitudinal, direction. That is precisely the type of impact a bolt attached to the blade root cannot cope with. If calm weather conditions are assumed and no mitigations have been applied to the multi-body systems, a maximum potential impact velocity of 0.207 m/s was detected. With the appropriate mitigations applied, this could be reduced by 34.8% to 0.135 m/s. The angle of the blade in equilibrium relative to the initial position is compensated by rotating the nacelle around the z-axis, to achieve alignment of blade and hub.

After considering five case studies, it was concluded that only the case study in which calm weather conditions are assumed, single blade installation may be possible, only if sufficient mitigation has been applied. Initial environmental and structural damping insufficiently attenuate the motions of both structures. Possible mitigations that are introduced to maximise installation feasibility are a tuned mass damper in the support structure model and tugger lines in the blade-crane model, both reducing mechanical vibrations. The tugger lines are modelled as additional modal damping of the multi-body system, decreasing the velocity of the blade, but the deflections remain unaffected. The damping specifically targets the first wet mode shape of the support structure and the two pendulum and yaw mode shapes of the blade suspended from a crane.

The results appear to be in line with observations on some offshore wind farms, where significant motions of the hub and blade may prevent blade installation, even during acceptably low wind velocities.

7.2. Recommendations

Several assumptions and delineations have been made during the scoping of this research. The blade is modelled with a straightforward method by simplifying the blade properties, due to the unavailability of a blade aerodynamic profile. A computer-aided design (CAD) program can be used to approach the blade more accurately by designing a blade and determining the surface area and other relevant properties like the mass moment of inertia and the area moment of inertia. An aerodynamic profile implies that lift and drag forces are both included. The lift and drag forces on the blade depend on the pitch angle, the angle of attack and the area of the blade during installation. If the three parameters are determined over the length of the blade, a more accurate force profile acting on the blade can be determined.

To further improve the multi-body blade model, a variety of systems with tugger lines acting on the blade could be introduced. A tugger line is primarily effective when used as a dampener, as can be concluded from the sensitivity analysis of the blade model. Tugger lines are known to counteract a yaw motion of the blade while suspended from a crane and additionally the pendulum motions are mitigated. In this thesis, the damping of a tugger line is added by adjusting the damping coefficient of specific mode shapes. The damping coefficients do not depend on the characteristics of a tugger line

in this thesis and therefore no conclusion can be drawn as to what tugger line is sufficient to safely complete the installation of a blade, even though it is known which damping coefficient is sufficient. Different configurations of a blade suspended from a crane including tugger lines need to be established, in which longitudinal degrees of freedom are introduced to represent a tugger line. Hereby, the tugger line will operate as a damper system and the characteristics of a tugger line can be included. It can be concluded from the yaw motion that at least two tugger lines are needed to counteract clockwise and anticlockwise yaw motions.

With the motions determined in this research, follow-up research can be conducted on how much damage the blade impact on the hub could cause. The behaviour of the blade relative to the hub is predominantly in the y-direction. This would be a sideways motion of the blade, leading to a lateral impact force on the bolts attached to the blade. If the kinetic energy of the blade when impact is imminent is determined, the results of this thesis could be the foundation of the follow-up research.

The multi-body systems composed in this thesis are solved in the time domain. Another approach would be to solve the models in the frequency domain. A frequency-domain graph will indicate how much of the signal is contained inside each specific frequency band throughout a variety of frequencies whereas a time-domain graph will illustrate how a signal varies over time. Although a time domain signal permits a better understanding of the structural changes of a system, the use of a frequency domain analysis will simplify the computational expense of the time domain. By converting the differential equation of a time domain analysis into an algebraic equation, the problem can be solved much more easily. The advantage of finding a solution in the frequency domain is that the system performance and stability can be tuned and optimized efficiently, resulting in very fast simulations. This would be very useful when an enormous number of simulations are required in a more extensive research, instead of the couple dozen simulations conducted to obtain the results of this thesis.

A

Design Requirements

The design requirements of the blade installation phase are compiled in this appendix. These requirements describe the parameters in which the project's scope shall be carried out, specifying the minimal acceptable technical standards. These requirements were compiled in the beginning of this project to establish an overview of the knowledge necessary for understanding the installation process of a blade. Figure A.1 is a breakdown of installation process of a blade. The principal features are set in orange, the blue branches are sub-requirements on a scale that you can compare designs with one another and check them for their safety, feasibility and possible improvement [38]. The scope of this research is reduced to the green area.

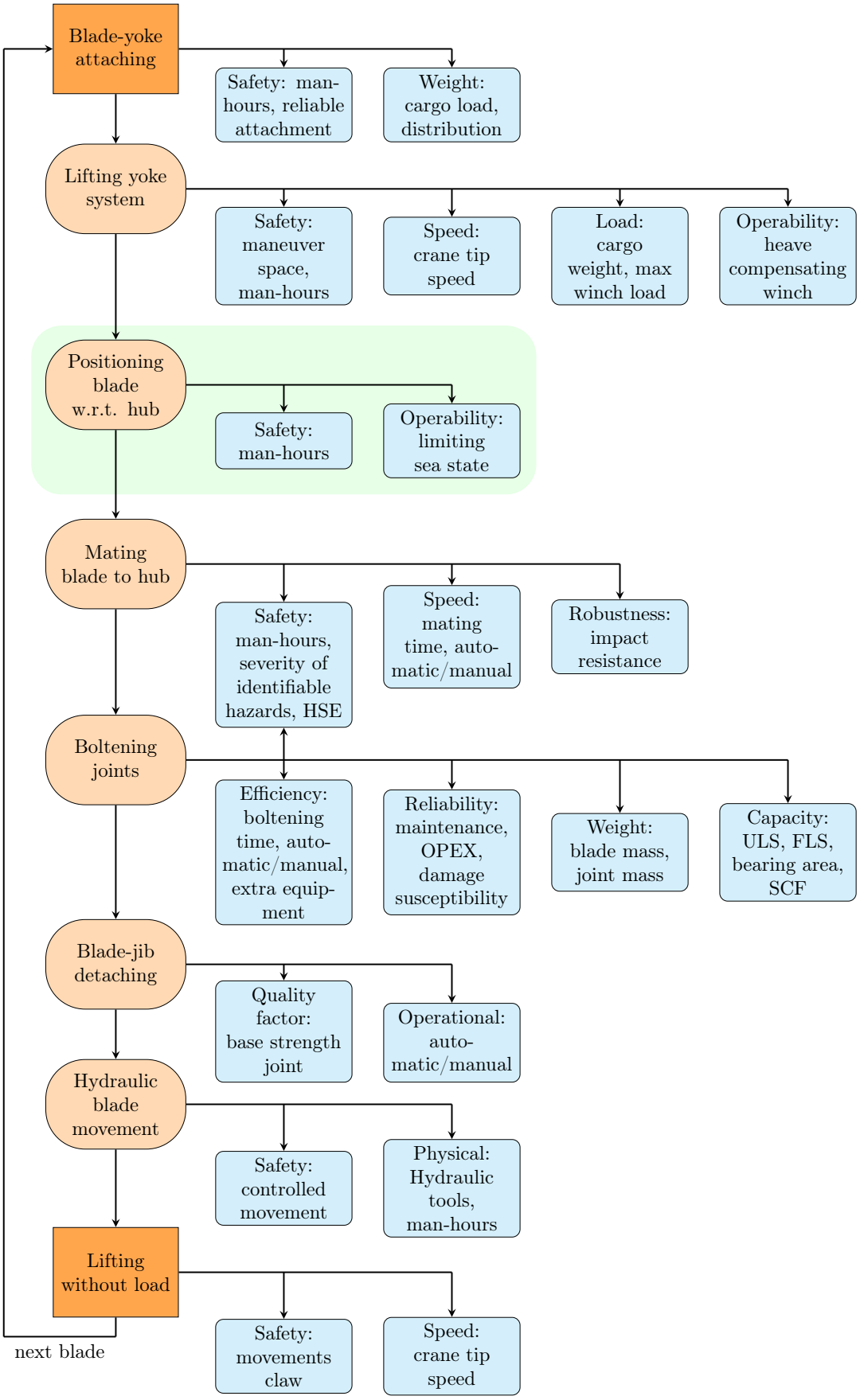

Figure A.1: Requirement breakdown for lift operation and installation of wind turbine blade

B

Existing Wind Turbine Characteristics

B.1. Dimensions

Existing wind turbines are also used as a baseline in this research. Manufacturers disclose little information about their wind turbines, but sufficient information is available for this study. Table B.1 provides characteristics on some of the larger wind turbines developed. Only the properties required for this thesis are summarised in both tables.

Table B.1: Characteristics of installed wind turbines

Type	Unit	MHI Vestas V236 [47]	SG 14-222 DD [28]	GE Haliade-X [46]	SG 11.0-200 DD [68]
Power	$[MW]$	15	14	12 / 14	11
Hub height	$[m]$	148	141	135	130
Roter diameter	$[m]$	236	222	220	200
Blade length	$[m]$	115.5	108	107	97
Hub diameter	$[m]$	5	6	6	6
Power density	$[W/m^2]$	342.9	361.7	315.7 / 368.3	350.1
Blade root diameter	$[m]$	-	-	5.5	-
Blade mass	$[t]$	64	-	55 - 62	-
Rotor nacelle assembly mass	$[t]$	892	-	825 / 965	-

B.2. Blade-hub interfaces

Figures 1.6a and 1.6b contain multiple parameters, these parameters are discussed an determined in this appendix. The variables that can be retrieved from figure 1.6a can be estimated with the equations below [23]. th is defined independently of the blade root design and is not included in this equation.

$$\begin{aligned} d/D &= 0.5 \\ w/D &= 2 \\ e &= 2.5D \\ t &= 1.5D \end{aligned} \tag{B.1}$$

The w/D ratio given is a common value for the T-bolt joint. There are no published works available during the writing of this thesis on experimental tests confirming a good method for extrapolating this value. So the common design value for the ratio is about 2, regardless the scaling. The larger wind turbines utilise circa M40 for a screw of the T-bolt joint. With the dimension approximations given above, this would give:

- $d = 40mm$
- $D = 80mm$
- $w = 160mm$
- $e = 200mm$
- $t = 120mm$

The approximation above can be expanded with an estimation of the amount of bolts needed. The scaling assessment in section 3.2.4 scales the blade root diameter of the 20 MW wind turbine to 5.84 m. This gives a circumference of 18.3 m. Taking a width of 160 mm between the center axis of the bolts results in 114 bolts. Decreasing the number of bolts would decrease the amount of actions during the mating and boltening phase, saving valuable time. The overall blade installation duration could reduce drastically.

B.2.1. Bonded insert joint

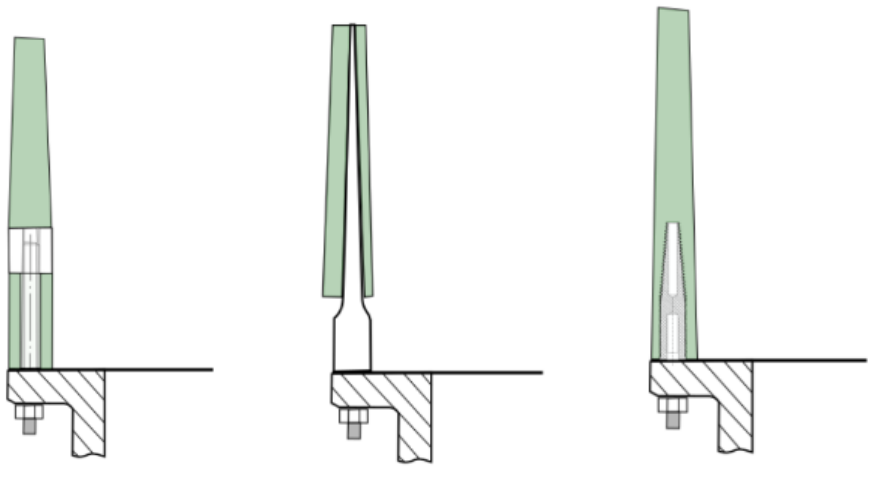

(a) T-bolt (b) Hub type (c) Stud type

Figure B.1: Different type of conventional cylindrical blade root connections used in the wind turbine industry [10].

A bonded insert joint has similar specifications as the T-bolt joint. Both types were the most commonly used composite blade connectors in 2012 [11]. Figure B.1 is a good reference to compare bonded inserts to the T-bolt. There are two bonded insert joints, which are demonstrated in figures B.1b and B.1c. A metal part is bonded inside (B.1b) or to (B.1c) the blade root. For additional guidance, figure B.2 is a segment comparison between a T-bolt and a hub type connection.

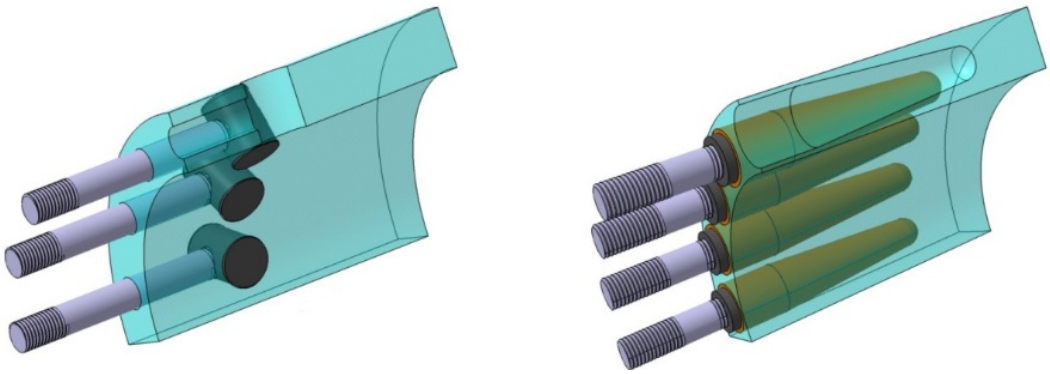

Figure B.2: T-bolt joints (left) compared to bonded insert joints (right) for a similar blade root segment [11].

The bearing strength of the blade root increases due to the absence of holes in the fabric, which are the holes needed to install the barrel nuts of the t-bolt. The resulting benefit is that the bolts can be positioned closer together when using the bonded inserts and that no drilling in the laminate is required. About 35% more bolts can be implemented due to the increased bearing strength of the blade root. On the contrary, it should be noted that more bolts in turn result in reduced bearing strength [10].

B.2.2. C1 Wedge Connection

The C1 Wedge Connection is a familiar concept in the wind energy sector. It is integrated into tower assemblies as a test. As dimensions of wind turbines increase, the towers reach lengths that cannot be transported in one piece, which could result in multiple tower members that need to be assembled at the designated location of the wind turbine.

The traditional L-flange connection used in towers starts to pose problems during lift operations and due to increasing operational loads. The traditional bolted L-flange scales poorly with increasing loads [69]. The issues accompanied with the traditional flange resulted in the development of the C1 Wedge Connection.

The C1 Wedge Connection is a symmetrical connection between two tubular sections, as shown in figure B.3. The cylindrical fork-shaped upper flange slides over the cylindrical lower flange such that holes located along the perimeter are aligned. After the flanges are fitted together, C1 fasteners are pushed in these holes to force the two flanges together. The C1 fasteners are the members that hold the connections in place, replacing the conventional bolts. By tightening the bolt, the inner and outer wedge are pulled towards each other. This in turn has the effect of pushing the upper block up and the lower block down. This way, a larger preload is reached by pulling the flanges together with help of the fasteners. With the notion that offshore wind turbines are growing, loads increase as well. The scalability of the C1 Wedge Connection makes it suitable for larger loads [69]. There are no damage susceptible bolts present in this design. Although the inner and outer wedge are pulled together through a force exerted by a M36 bolt, as can be seen in figure B.3, it is not a critical member and not a critical failure load that the bolt is subjected to.

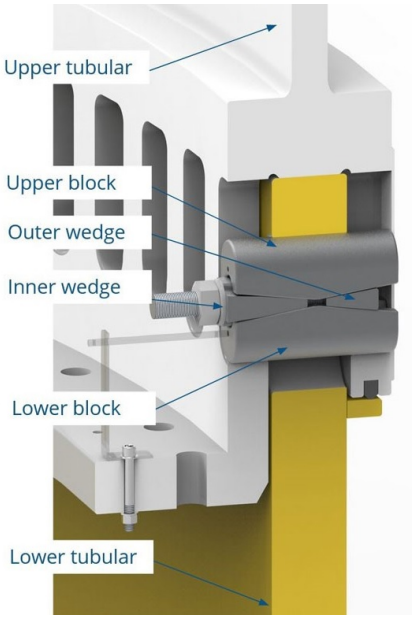

Figure B.3: Main components of C1 Wedge Connection.

The design of this connection eliminates the safety liability of a worker needed on the outside of the connection when mating, as there is only one person needed on the inside of the wind turbine to push the C1 fasteners in place and secure the bolts. This can also be achieved by an automated system.

B.2.3. T-bolt vs. C1 wedge connection

The approximation of the T-bolt joint dimensions in section B.2 gave an insight on the amount of bolts that need to be secured before detaching the blade from the jib. Decreasing the number of actions during the mating and boltening phase would decrease the overall blade installation duration drastically. The scaling assessment in chapter 3.2 scales the blade root diameter of the 2030 wind turbine to 5.84 m. This gives a circumference of 18.3 m. The length of a segment is a multiplication of the C1 fastener diameter: $l_{seg} = 2.02 * D_{fastener}$. One segment of 202 mm results in a plane of influence of one C1 fastener of typically 100 mm. The circumference of 18.3 m needs around 91 C1 fasteners. Compared to the 114 bolts needed in the T-bolt joint, you need 20% less bolts in the C1 wedge connection. Taking into account that tightening the bolts in the C1 connection is less delicate than tightening T-bolts would reduce the boltening time even more.

A C1 joint is similar to a T-bolt joint without a hole for the screw, which allows for a higher load in your laminate shear area and bearing area. A lower stress concentration factor is achieved due to the slot hole in the flanges that the C1 wedge connection has compared to a rounded hole with a higher stress concentration factor. The load path of a slot hole is slightly better due to the reduced gradient of the load path lines [70]. The better load management of the C1 wedge connection is a factor that reduces the number of joints needed.

The mating phase is a delicate phase in which a lot of damage can be inflected on the blade. Initially, damage to the blade root bolts, followed by the delay of the installation time frame. If figure B.3 is viewed again, it can be argued that there are less impact sensitive components in the connection and a small impact might not damage the blade root.

So far three full-scale connections with diameters ranging from 3.5 m to 7 m have been manufactured by the company producing the C1 Wedge Connection [69] and implemented in tower structures for tests. The C1 wedge connection is added to this thesis, as it may act as a connection between hub and blade in the future. Typical blade root diameters of the largest wind turbines in operation are between 5 m and 6 m, but loads will differ compared to a support structure. Therefore, additional testing will be necessary to conduct before implementing the C1 wedge connection as a blade-hub connection.

C

Metocean Data

C.1. JONSWAP sea-states: wave elevation

Figures C.1 and C.4 describe the energy per frequency of a JONSWAP spectrum in respectively a normal and rough sea-state. Figure C.2 and C.5 depict the corresponding wave elevation of the two sea-states.

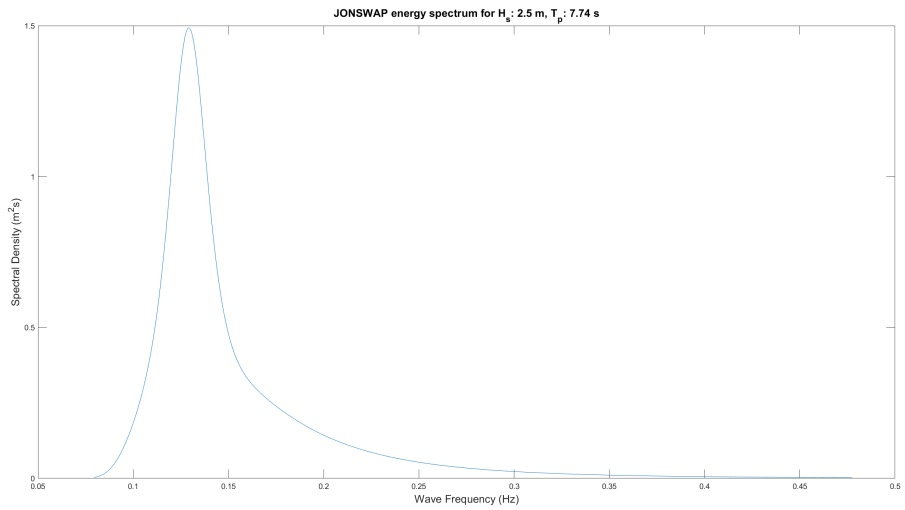

Figure C.1: JONSWAP spectrum of normal sea-state, $H_s = 2.5$ m and $T_p = 7.74$ s.

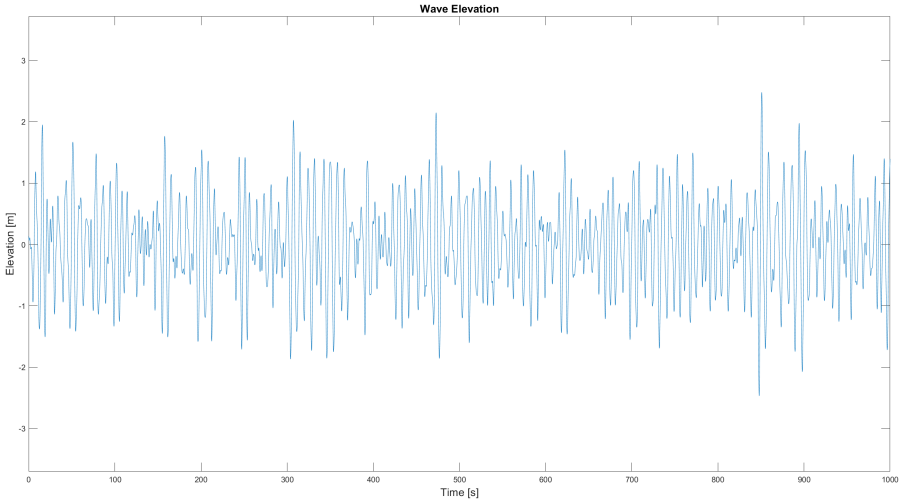

Figure C.2: Wave elevation of normal sea-state, $H_s = 2.5$ m and $T_p = 7.74$ s.

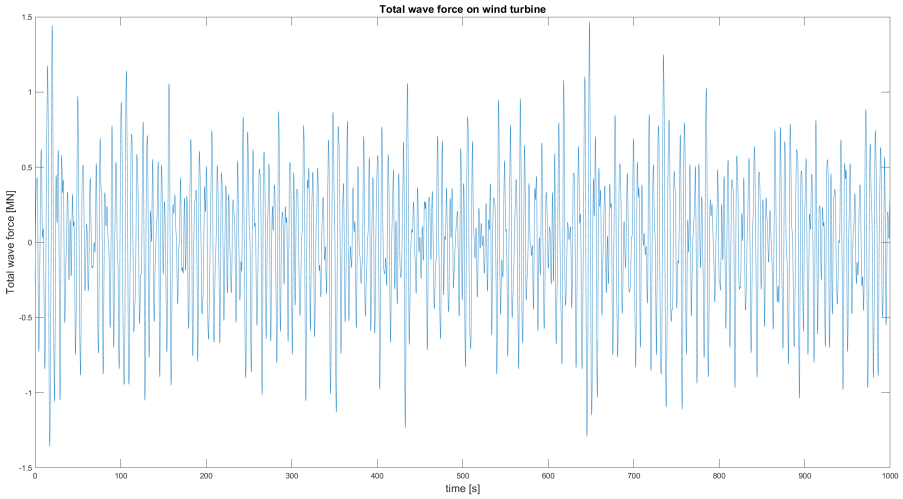

Figure C.3: Wave force of normal sea-state, $H_s = 2.5$ m and $T_p = 7.74$ s.

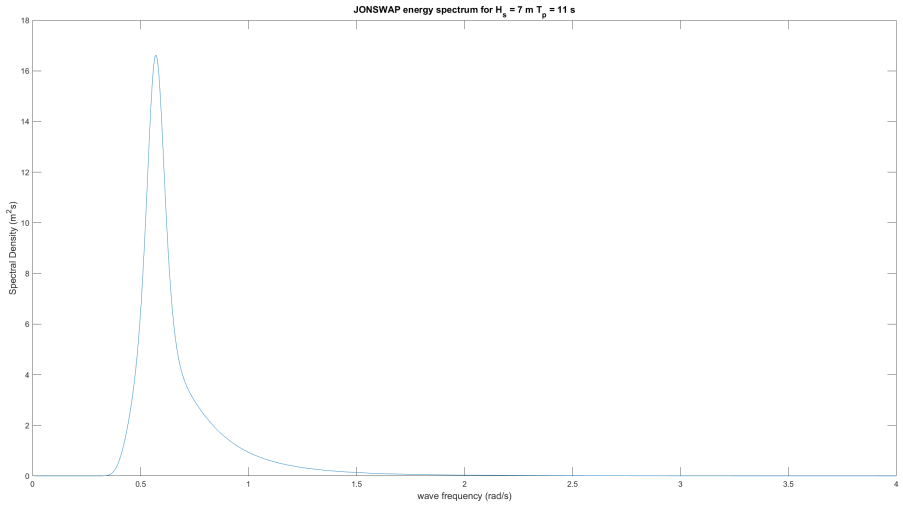

Figure C.4: JONSWAP spectrum of rough sea-state, $H_s = 7$ m and $T_p = 11$ s.

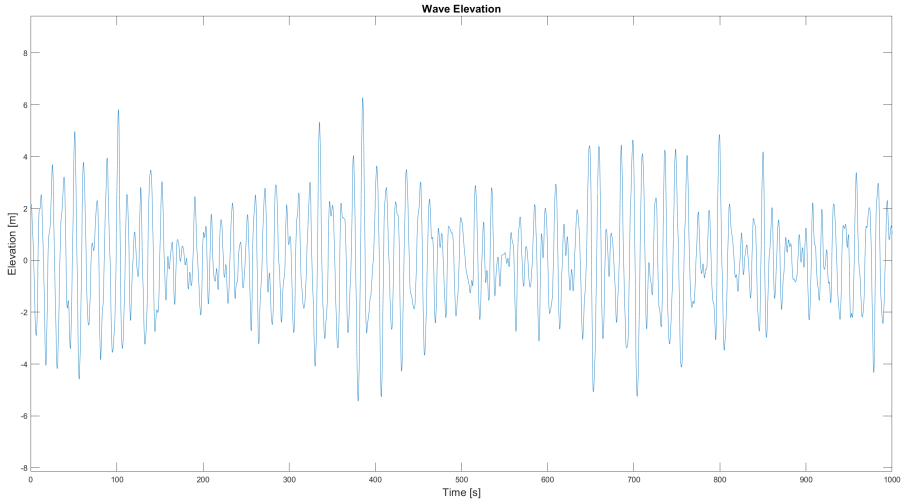

Figure C.5: Wave elevation of rough sea-state, $H_s = 7$ m and $T_p = 11$ s.

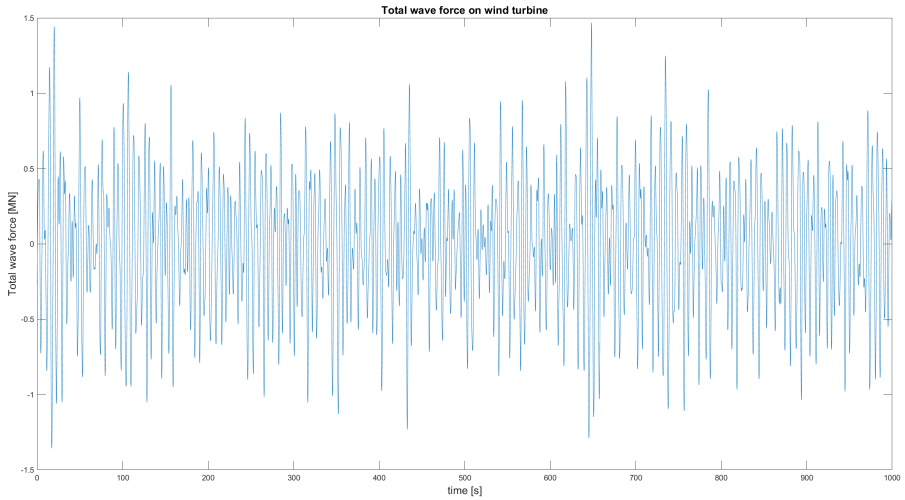

Figure C.6: Wave force of rough sea-state, $H_s = 7$ m and $T_p = 11$ s.

C.1.1. Wave and Wind Frequency

Multiple sine waves are superimposed to create the irregular waves representing the wave elevations with the help of equation C.1. An extensive explanation on these irregular waves can be found in section 4.7. Figures C.7, C.8, and C.9 are the fast Fourier transforms of the wave elevations displayed in figures 4.6, C.2, and C.5.

The amount of sine waves used for the support structure model is 20 for the water waves and 7 for the wind waves, but the are not all visible in the Fourier transform because some frequencies have very low excitation energy. The amount of sine waves used for the blade model in the $z - x$ plane is 13 and the sine waves used for the blade model in the $x - y$ plane are the first 7. These numbers are limited due to a number of maximum characters that can be used in an Ordinary Differential Equation of MATLAB.

$$\overline{\zeta} = \sum_{1}^{k} A \, sin(\omega_n t + \epsilon) \tag{C.1}$$

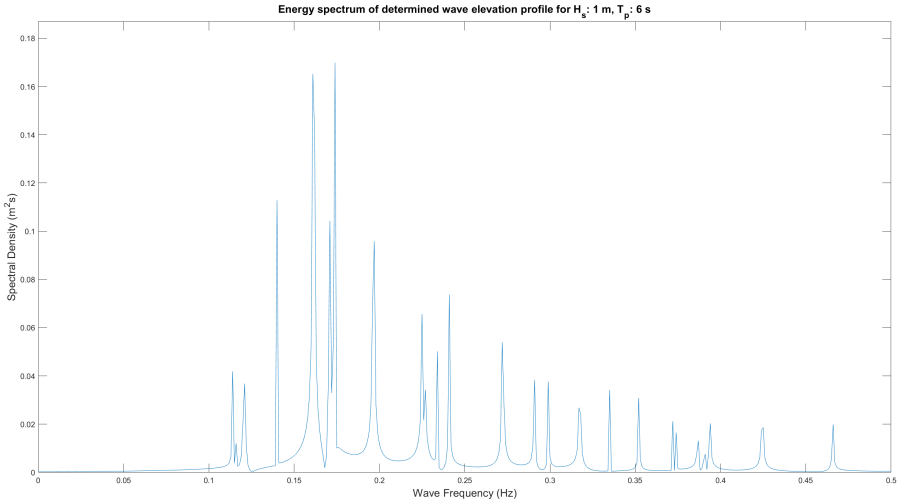

Figure C.7: Fast Fourier transform of wave elevation time series in calm sea-state.

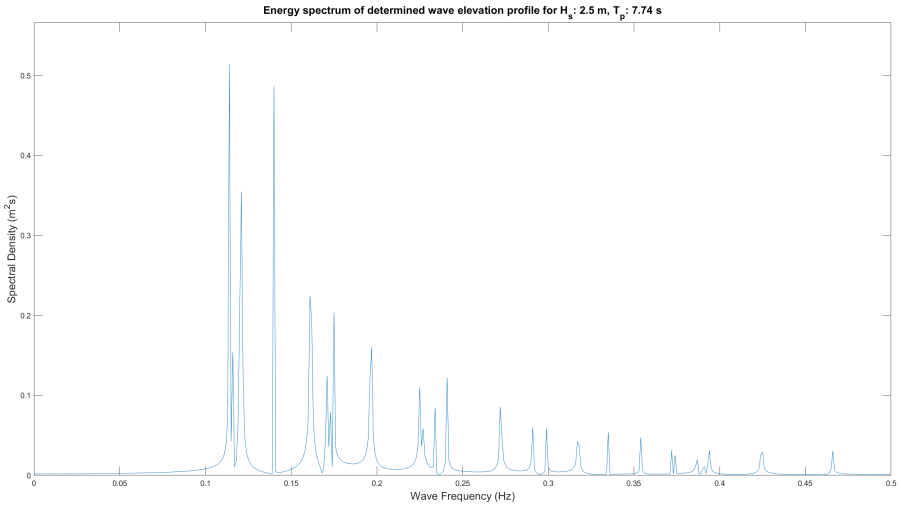

Figure C.8: Fast Fourier transform of wave elevation time series in normal sea-state.

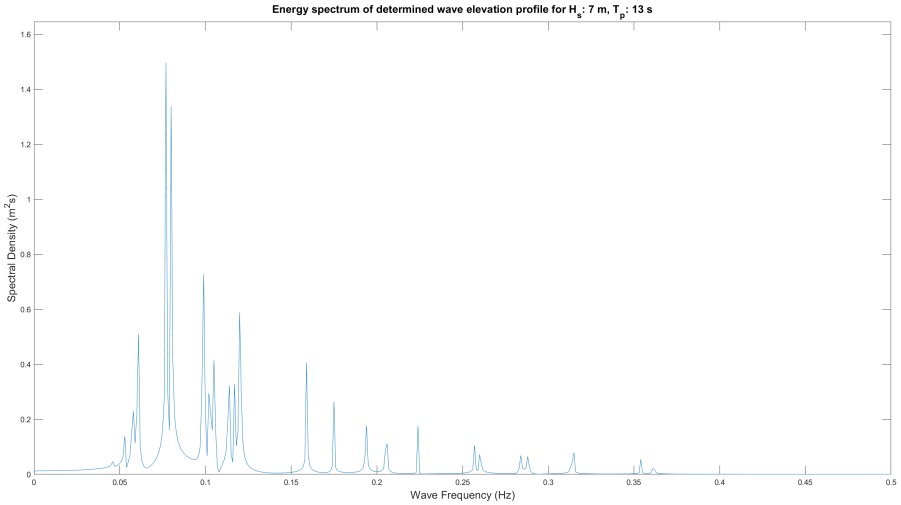

Figure C.9: Fast Fourier transform of wave elevation time series in rough sea-state.

C.2. Wind velocity scaling

Figure C.10 provides an inside into how much wind one might expect in the Dutch designated wind farm Nederwiek. The data of certain coordinates is retrieved from the website Metoceanview [71]. It shows that during winter months, wind velocities are more detrimental to installing wind turbines if a limit of 8-12 m/s for blade installation is used. Table C.1 shows the actual values plotted in figure C.10 per percentile for the Dutch areas Nederwiek and Doordewind. The percentile graph for Doordewind was left out of this appendix due to redundancy.

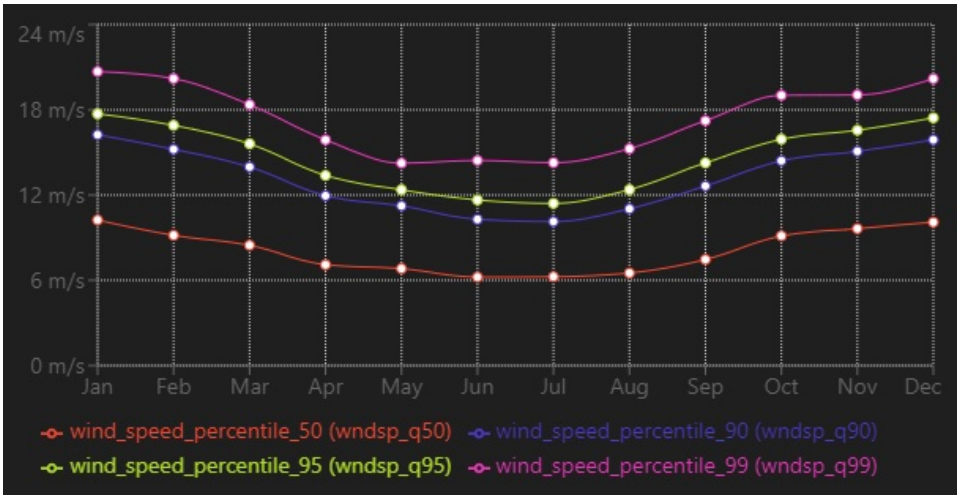

Figure C.10: Wind percentile graph Nederwiek [12].

The 75th percentile in table C.1 was not data that was provided by the internet source, but it was determined by taking the ratio $\frac{75}{50}$ of the 50th percentile value. This assumption was made to fill the gap of data between the 50th and 90th percentile.

Table C.1: Wind velocity percentiles per month at 10 m height [12].

	Nederwiek maximum wind velocity $[m/s]$					Doordewind maximum wind velocity $[m/s]$				
Percentile	50 %	75 %	90 %	95 %	99 %	50 %	75 %	90 %	95 %	99 %
January	10.24	15.36	16.24	17.71	20.69	10.28	20.99	16.31	17.93	21.10
February	9.16	13.74	15.22	16.90	20.19	9.15	18.68	15.28	16.87	20.29
March	8.47	12.71	13.98	15.61	18.36	8.74	17.84	14.17	15.68	18.44
April	7.09	10.64	11.95	13.37	15.88	7.05	14.39	11.77	13.19	15.94
May	6.82	10.23	11.24	12.37	14.24	6.83	13.94	11.05	12.12	14.04
June	6.22	9.33	10.29	11.65	14.43	6.55	13.37	10.70	11.84	14.37
July	6.25	9.38	10.13	11.41	14.28	6.63	13.53	10.47	11.64	14.30
August	6.51	9.77	11.03	12.38	15.26	6.81	13.90	11.13	12.46	15.13
September	7.46	11.19	12.64	14.26	17.23	7.85	16.02	12.73	14.29	17.08
October	9.12	13.68	14.41	15.93	19.01	9.26	18.90	14.64	15.98	19.16
November	9.63	14.45	15.08	16.56	19.05	9.85	20.11	15.24	16.79	19.61
December	10.09	15.14	15.89	17.43	20.18	10.08	20.58	16.03	17.59	20.32
Mean	8.09	12.13	13.18	14.63	17.40	8.26	16.86	13.29	14.70	17.48

With help of equations 3.2 and 3.3, respectively the logarithmic profile and the power law profile, the wind velocities at hub height, 154.7 m, were determined. Every wind velocity mentioned in table C.1 was scaled, which resulted in table C.2.

Table C.2: Wind velocity percentiles per month at hub height.

	Nederwiek maximum wind velocity $[m/s]$					Doordewind maximum wind velocity $[m/s]$				
Percentile	50 %	70 %	90 %	95 %	99 %	50 %	70 %	90 %	95 %	99 %
January	13.34	18.67	21.15	23.07	26.95	13.39	18.75	21.24	23.35	27.48
February	11.93	16.70	19.82	22.01	26.30	11.92	16.69	19.90	21.97	26.43
March	11.03	15.45	18.21	20.33	23.91	11.38	15.94	18.46	20.42	24.02
April	9.23	12.93	15.57	17.41	20.68	9.18	12.86	15.33	17.18	20.76
May	8.88	12.44	14.64	16.11	18.55	8.90	12.45	14.39	15.79	18.29
June	8.10	11.34	13.40	15.17	18.80	8.53	11.94	13.94	15.42	18.72
July	8.14	11.40	13.19	14.86	18.60	8.64	12.09	13.64	15.16	18.63
August	8.48	11.87	14.37	16.13	19.88	8.87	12.42	14.50	16.23	19.71
September	9.72	13.60	16.46	18.57	22.44	10.22	14.31	16.58	18.61	22.25
October	11.88	16.63	18.77	20.75	24.76	12.06	16.89	19.07	20.81	24.96
November	12.54	17.56	19.64	21.57	24.81	12.83	17.96	19.85	21.87	25.54
December	13.14	18.40	20.70	22.70	26.29	13.13	18.38	20.88	22.91	26.47
Mean	10.54	14.75	17.16	19.06	22.66	10.75	15.06	17.32	19.15	22.77

Trivially, the 75th percentile means that for about 6 hours per day installation is not possible. This results in a weather window of 18 hours in which installation can be conducted, which could be long enough to install at least one wind turbine. To get a better sense of whether the data is favorable or unfavorable, workabilities of the blade install operation are estimated. For workability purposes it is now assumed that the workability is 75 percent during any given month in which the dynamic system can operate when looking at the maximum wind velocity in that specific month for the 75th percentile. This means that if the operable limit lies above 12.70 m/s, an installation is possible in June for the 75th percentile and thus the workability for June is 75%. Table C.3 lists the workabilities of different dynamic system limits for both locations. These new workabilities, which are less accurate due to the aforementioned assumptions, have a smaller bin size than the wind states in table C.4 and are scaled to Zephyros' hub height.

Table C.3: Workability if 70th percentile of the wind data is taken. Maximum workabitlity can thus become 70 percent per month.

	Nederwiek		Doordewind	
Dynamic system boundary	Operable months	Workability	Operable months	Workability
12 m/s	May - August	23.3 %	May - August	23.3 %
13 m/s	April - August	29.2 %	April - August	29.2 %
14 m/s	April - September	35.0 %	April - September	35.0 %
15 m/s	March - September	40.8 %	April - September	35.0 %
16 m/s	March - September	40.8 %	March - September	40.8 %
17 m/s	February - October	52.5 %	February - October	52.5 %
18 m/s	February - December	64.2 %	February - December	64.2 %
19 m/s	January - December	70.0 %	January - December	70.0 %

The workabilities in table C.3 indicate that a high dynamic system boundary is needed to make the operation profitable. This boundary is identified as a velocity and to find out if these velocities are achievable, the forces affecting the blade while installing are considered. These forces, such as lift and drag, scale with velocity squared. In the research, it is stated that the current dynamic boundary limit is somewhere in the range of 8 to 12 m/s. If an improvement from 12 m/s to 18 m/s is going to be made, this will result in $6^2 = 36$ times more force exerted on the blade. If not handled correctly, this could be catastrophic.

C.3. Workability

Workability is a ratio of hours with conditions in which an operation can take place to total hours in that same period, hence a percentage. Increased workability means that more labour can be done over a period of time, this can be achieved either because conditions are better or because an operation can withstand more severe conditions. A workability assessment combines the offshore environment, the marine dynamic behaviour and the operational procedure, which results in the environmental risk of the operation [72]. Important parameters are wave heights, wave headings, wave periods, wind velocities, and wind headings. It is common to make a scatter diagram of this metocean data, consisting of significant wave heights and peak periods. If the data is available then it can also be useful to make a scatter diagram of significant wave heights and mean wind velocities. For research purpose, it is chosen to use the hindcast data of two coordinates, both of which lie in aforementioned designated wind energy areas. The data for wind and waves used in this literature study is provided by a website called Metoceanview and is data from measurements taken between 1979-01-01 and 2016-01-01 [12]. Figures C.11 and C.12 are scatter diagrams of respectively Nederwiek and Doordewind.

Significant wave height m \ Relative peak period (smooth) s	0 - 1	1 - 2	2 - 3	3 - 4	4 - 5	5 - 6	6 - 7	7 - 8	8 - 9	9 - 10	10 - 11	11 - 12	12 - 13	13 - 14	14 - 15	15 - 16	16 - 17	17 - 18	18 - 19	19 - 20
0 - 0.5	0%	<0.1%	0.4%	2.2%	1.1%	0.4%	0.1%	0.2%	0.2%	0.1%	<0.1%	<0.1%	<0.1%	0.1%	0.1%	0.1%	<0.1%	<0.1%	<0.1%	<0.1%
0.5 - 1	0%	0%	<0.1%	3.9%	9.5%	5.1%	3%	1.8%	1.2%	1%	0.7%	0.3%	0.2%	0.2%	0.2%	0.2%	0.1%	0.1%	<0.1%	<0.1%
1 - 1.5	0%	0%	0%	<0.1%	4.4%	9.3%	3.8%	2.8%	1.7%	1.4%	1.5%	0.8%	0.3%	0.1%	<0.1%	<0.1%	<0.1%	<0.1%	<0.1%	<0.1%
1.5 - 2	0%	0%	0%	0%	<0.1%	6%	5.1%	2%	0.8%	0.5%	0.6%	0.6%	0.2%	0.2%	<0.1%	<0.1%	<0.1%	<0.1%	<0.1%	0%
2 - 2.5	0%	0%	0%	0%	0%	0.5%	6.2%	2.2%	0.6%	0.1%	<0.1%	0.1%	<0.1%	<0.1%	<0.1%	<0.1%	<0.1%	0%	0%	0%
2.5 - 3	0%	0%	0%	0%	0%	<0.1%	1.8%	3.7%	0.7%	<0.1%	<0.1%	<0.1%	<0.1%	<0.1%	<0.1%	0%	0%	0%	0%	0%
3 - 3.5	0%	0%	0%	0%	0%	0%	<0.1%	2.8%	0.9%	<0.1%	<0.1%	0%	0%	0%	0%	0%	0%	0%	0%	0%
3.5 - 4	0%	0%	0%	0%	0%	0%	0%	0.8%	1.4%	0.1%	<0.1%	0%	0%	0%	0%	0%	0%	0%	0%	0%
4 - 4.5	0%	0%	0%	0%	0%	0%	0%	<0.1%	1%	0.3%	<0.1%	0%	0%	0%	0%	0%	0%	0%	0%	0%
4.5 - 5	0%	0%	0%	0%	0%	0%	0%	0%	0.3%	0.3%	<0.1%	0%	0%	0%	0%	0%	0%	0%	0%	0%
5 - 5.5	0%	0%	0%	0%	0%	0%	0%	0%	<0.1%	0.2%	<0.1%	0%	0%	0%	0%	0%	0%	0%	0%	0%
5.5 - 6	0%	0%	0%	0%	0%	0%	0%	0%	0%	<0.1%	<0.1%	0%	0%	0%	0%	0%	0%	0%	0%	0%
6 - 6.5	0%	0%	0%	0%	0%	0%	0%	0%	0%	<0.1%	<0.1%	0%	0%	0%	0%	0%	0%	0%	0%	0%
6.5 - 7	0%	0%	0%	0%	0%	0%	0%	0%	0%	0%	<0.1%	0%	0%	0%	0%	0%	0%	0%	0%	0%

Figure C.11: Scatter diagram for workability purpose, Nederwiek [12]

Significant wave height m \ Relative peak period (smooth) s	0 - 1	1 - 2	2 - 3	3 - 4	4 - 5	5 - 6	6 - 7	7 - 8	8 - 9	9 - 10	10 - 11	11 - 12	12 - 13	13 - 14	14 - 15	15 - 16	16 - 17	17 - 18	18 - 19	19 - 20
0 - 0.5	0%	0%	0.3%	1.7%	1.1%	0.3%	<0.1%	0.1%	0.1%	<0.1%	<0.1%	0.1%	0.1%	0.2%	<0.1%	<0.1%	<0.1%	<0.1%	<0.1%	<0.1%
0.5 - 1	0%	0%	<0.1%	3.2%	7.9%	5.6%	2.7%	1.4%	1.1%	0.8%	0.4%	0.3%	0.2%	0.5%	0.5%	0.5%	0.2%	0.1%	<0.1%	<0.1%
1 - 1.5	0%	0%	0%	<0.1%	3.5%	8.2%	4.8%	3%	1.5%	1.3%	1.1%	0.5%	0.2%	0.2%	0.1%	0.1%	<0.1%	<0.1%	<0.1%	<0.1%
1.5 - 2	0%	0%	0%	0%	<0.1%	4.5%	5.3%	3.3%	1.3%	0.6%	0.8%	0.6%	0.3%	0.1%	<0.1%	<0.1%	<0.1%	<0.1%	<0.1%	<0.1%
2 - 2.5	0%	0%	0%	0%	0%	0.3%	4%	3.5%	1.2%	0.4%	0.3%	0.3%	0.2%	0.2%	<0.1%	<0.1%	<0.1%	0%	0%	<0.1%
2.5 - 3	0%	0%	0%	0%	0%	<0.1%	0.8%	3.6%	1.5%	0.3%	0.2%	<0.1%	<0.1%	<0.1%	<0.1%	<0.1%	0%	0%	0%	0%
3 - 3.5	0%	0%	0%	0%	0%	0%	<0.1%	1.7%	2%	0.4%	<0.1%	<0.1%	<0.1%	<0.1%	<0.1%	0%	0%	0%	0%	0%
3.5 - 4	0%	0%	0%	0%	0%	0%	0%	0.3%	1.9%	0.5%	<0.1%	<0.1%	<0.1%	<0.1%	0%	0%	0%	0%	0%	0%
4 - 4.5	0%	0%	0%	0%	0%	0%	0%	<0.1%	0.9%	0.8%	<0.1%	<0.1%	0%	0%	0%	0%	0%	0%	0%	0%
4.5 - 5	0%	0%	0%	0%	0%	0%	0%	0%	0.1%	0.8%	0.1%	<0.1%	0%	0%	0%	0%	0%	0%	0%	0%
5 - 5.5	0%	0%	0%	0%	0%	0%	0%	0%	<0.1%	0.4%	0.2%	<0.1%	0%	0%	0%	0%	0%	0%	0%	0%
5.5 - 6	0%	0%	0%	0%	0%	0%	0%	0%	0%	<0.1%	0.2%	<0.1%	<0.1%	0%	0%	0%	0%	0%	0%	0%
6 - 6.5	0%	0%	0%	0%	0%	0%	0%	0%	0%	<0.1%	0.1%	<0.1%	0%	0%	0%	0%	0%	0%	0%	0%
6.5 - 7	0%	0%	0%	0%	0%	0%	0%	0%	0%	0%	<0.1%	<0.1%	0%	0%	0%	0%	0%	0%	0%	0%
7 - 7.5	0%	0%	0%	0%	0%	0%	0%	0%	0%	0%	<0.1%	<0.1%	<0.1%	0%	0%	0%	0%	0%	0%	0%
7.5 - 8	0%	0%	0%	0%	0%	0%	0%	0%	0%	0%	0%	<0.1%	<0.1%	0%	0%	0%	0%	0%	0%	0%
8 - 8.5	0%	0%	0%	0%	0%	0%	0%	0%	0%	0%	0%	<0.1%	0%	0%	0%	0%	0%	0%	0%	0%

Figure C.12: Scatter diagram for workability purpose, Doordewind [12]

A vessel has limitations and based on these limits a workability can be determined. In table C.4, some limitations of a installation operation that could take place are estimated based on literature of Fred Olsen windcarrier Brave Tern [13]. The Brave Tern is a carrier on which reliable specifications are available, apart from the peak period, which is calculated with the help of formula C.2 [73]. After the selections for significant wave height (H_s) and peak period (T_p) were made, the workability was determined using figures C.11 and C.12. The tables consist of buckets with the probability of occurrence of a combination of significant wave heights and peak periods.

$$\sqrt{13H_s} < T_p < \sqrt{30H_s} \tag{C.2}$$

Table C.4: Workability of various classes of boundaries and the Brave Tern [13].

Limit class	Significant wave height $H_s[m]$	Peak period $T_p[s]$	Mean wind velocity limit $[m/s]$	Workability waves / wind Nederwiek	Workability waves / wind Doordewind
Brave Tern	1.8	4.84 - 7.35	16	22.0 % - 57.0 % / 93.9 %	18.0 % - 53.0 % / 93.7 %
Class 1.1	2.0	6.0	10	42.0 % / 69.2 %	36.0 % / 68.0 %
Class 1.2	2.0	6.0	15	42.0 % / 93.9 %	36.0 % / 93.7 %
Class 2.1	2.5	6.0	10	43.0 % / 69.2 %	37.0 % / 68.0 %
Class 2.2	2.5	6.0	15	43.0 % / 93.9 %	37.0 % / 93.7 %
Class 3.1	2.0	8.0	10	61.0 % / 69.2 %	57.0 % / 68.0 %
Class 3.2	2.0	8.0	15	61.0 % / 93.9 %	57.0 % / 93.7 %
Class 4.1	2.5	8.0	10	70.0 % / 69.2 %	65.0 % / 68.0 %
Class 4.2	2.5	8.0	15	70.0 % / 93.9 %	65.0 % / 93.7 %
Class 5.1	2.0	10.0	10	68.0 % / 69.2 %	63.6 % / 68.0 %
Class 5.2	2.0	10.0	15	68.0 % / 93.9 %	63.6 % / 93.7 %
Class 6.1	2.5	10.0	10	78.0 % / 69.2 %	73.0 % / 68.0 %
Class 6.2	2.5	10.0	15	78.0 % / 93.9 %	73.0 % / 93.7 %

It can be observed from table C.4 that especially the combinations of H_s and T_p are determining the maximum workability per class. There is in fact much more involved than just a significant wave height and peak period, for instance the angle of attack. But the assumption in this research is that a vessel can handle these values in table C.4 at any angle. The obtained hindcast wind data is reliable, but the downside of this data is that the bin size of the mean wind velocity is too large. Smaller intervals at mean wind velocity are needed, for instance 12-13 and 13-14. Especially the part between 10 and 15 m/s is interesting for research purpose to find new capabilities for single blade installation, as the limit is normally set at 12 m/s and any minimal improvement from this point on should be explored. However, it can be said that if there is a dynamic system which can handle 15 m/s, the mean wind velocity will be a less significant problem with single blade installation. However, gusts of wind can still cause problems and therefore the maximum wind velocity must also be accounted for and this is being carried out in the next paragraph. Also a downside of this wind hindcast data is that the measurements are probably done at a height of 10 m.

C.4. Wave and Current Force

C.4.1. Coefficients

The coefficients C_D and C_M in equations 4.47, 4.54 and 4.56 are determined based on the Reynolds number. The Reynolds numbers were calculated with the help of equation 3.9 and are listed below in table C.5. The velocities are taken as the mean over the height of one segment. The velocity and Reynolds number for the segment that is under mean sea level (segment 1) have a range as the wave frequency has a range on account of the JONSWAP spectrum.

Member subscript	Average velocity	Diameter	Kinematic viscosity	Reynolds number
1	1.09 - 0.42 m/s	11.0 m	1.004e-6 m^2/s	11.94e6 - 4.60e6
2	12.80 m/s	10.6 m	14.88e-6 m^2/s	9.12e6
3	14.51 m/s	8.0 m	14.88e-6 m^2/s	7.80e6

Table C.5: Reynolds number with necessary corresponding parameters and drag coefficients.

Figure C.13 describes the correlation between a Reynolds number and a drag coefficient [74]. If the Reynolds numbers of table C.5 are observed, it is noted that the three values have an order of magnitude of $10e7$. In relation with figure C.13, this gives a drag coefficient of 0.6 - 0.9 for every drag force calculation in this section.

Figure C.13: Correlation between Reynolds number and drag coefficient for different objects.

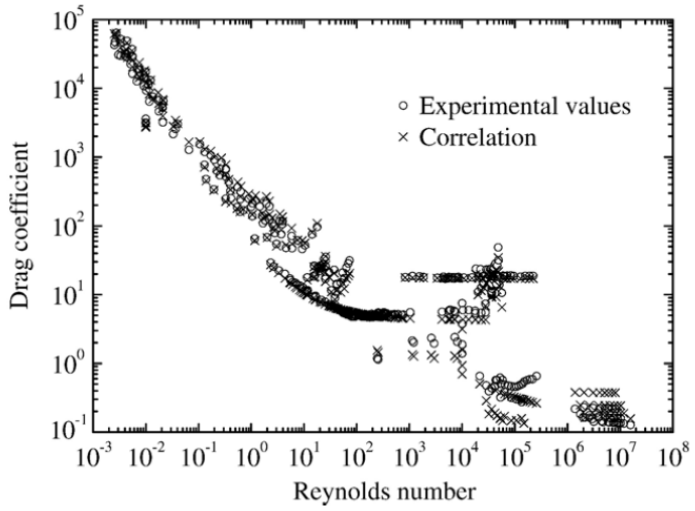

D

Euler-Bernoulli beam theory

The Euler-Bernoulli beam theory is a simplification of the linear theory of elasticity, which is based on Hooke's law. It enables the calculation of the load-carrying and deflection characteristics of beams and is based upon Newtonian mechanics. To define the mathematical problem several assumptions are made. These assumptions result into allowing the use of the Euler-Bernoulli beam theory [75].

1. Only small deflections are acceptable.
2. The beam is subjected to only lateral loads.
3. Shear deformation and rotatory inertia is ignored.
4. The material is linear elastic according to Hooke's law, EI is constant.

The wind turbine monopile and tower are modelled as one Euler-Bernoulli beam to get a first impression of the output parameters of the subsequent model which will be constructed at a later stage in this thesis. The third item specifies that the deadweight of the nacelle and the beam should be neglected. If the fourth item above is not applicable to the model, then it would concern the Timoshenko beam theory, but as shear deformation is not of significant influence in a simplified wind turbine model, the theory for this model can be simplified to the Euler-Bernoulli beam theory. Normally, the material of a wind turbine would not be linear elastic according to Hooke's law. As the elasticity and inertia of the beam changes over height. Several dimensions can create a multitude of the equations being used in a model. This involves more extensive labour when solving the equations [75].

To better understand a structural vibration problem, the resonances of a structure needs to be characterised. A common and useful way of doing this is to define its modes of vibration. Each mode is defined by a modal frequency, modal damping, and a mode shape [76]. The Euler-Bernoulli beam consists of one degree of freedom with one equation of motion and therefore can only be approached with one single mode shape and natural frequency. A mode shape tells how the structure tends to deform at a specific natural frequency. Even when this is a dominant mode shape, it will not describe the behaviour of the beam in full. But as aforementioned, it does provide a good indication of a potential beam deflection.

The following steps were conducted to conclude with a structural response. First, apply the equations of equilibrium as in equation D.1 and determine the reactions of the beam. Second, generate a function for bending moment along the beam center axis. Third, use equation D.2 to establish an equation of slope and deflection by integrating the equation respectively once and twice, which will result in equations D.3 and D.4. It is a definite integral. The integration constants that result from integrating can be defined by applying the boundary conditions [77].

$$\begin{aligned} \sum M &= 0 \\ \sum F_{x,y,z} &= 0 \end{aligned} \tag{D.1}$$

$$EI\frac{d^2y}{dx^2} = M(x) \tag{D.2}$$

$$\frac{dy}{dx} = \frac{1}{EI}\left(\int_a^b M(x) + C_1\right) \tag{D.3}$$

$$y = \frac{1}{EI}\left(\int_a^b \int_a^b M(x) + C_1 x + C_2\right) \tag{D.4}$$

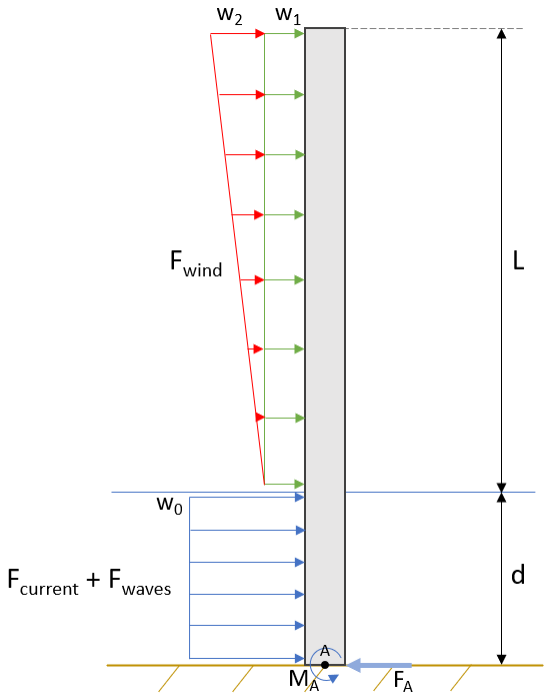

Figure D.1: Euler-Bernoulli beam with simplified force excitation.

The figure on the left depicts a simplified model used to obtain a comparative value for the angle and deflection of an offshore wind turbine. Forces due to wind, waves and current are simplified to forces that partly consist of a rectangular (constant) distributed load and a triangular (decreasing) distributed load. Normally, waves increase exponentially from seabed to MSL and wind decreases exponentially from hub height to MSL.

The wind force on the beam is purely a drag force as the lift forces on the beam are negligible. If the wind turbine blades are taken into account as well, lift will be of significant influence. The inertia force is also not included as the wind is modelled with constant velocity and therefore without an acceleration.

The wave force contains both drag and inertia forces, in which the current force is drag and the wave force is drag and inertia. M_A and F_A are the reaction force and moment of the distributed loads around the origin A.

Because it did not work to model the waves with a rectangular and a triangular part due to unidentified fourth-order modelling problems, the waves and current are modelled as only a rectangular part, that corresponds to the total moment and force excited by the rectangular and triangular sections combined. This is also reflected in the figure on the left.

Referring to the conditions of an Euler-Bernoulli beam, there may only be one degree of freedom and thus one moment line that is substituted in equation D.2. Problems occur when trying to derive a moment line as often multiple moment lines are used to describe a system as in figure D.1. In this case, the Macaulay method must be used. Macaulay uses the singularity function to describe the system with one moment line [77]. The determining of this function is explained by means of figure D.2 and equation D.5 in which the figure is not a representation of the offshore wind turbine under loading.

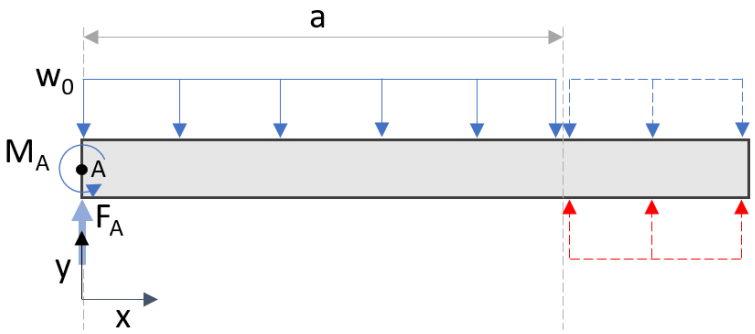

Figure D.2: Macaulay's method illustrated.

What one should know about figure D.2 is that the continuous lines are the real load and the dotted lines are the loads that are added to be able to compose the singularity function. Load w_0 starts at the origin of the beam but must be switched off at $x = a$. If $x > a$, the load should be zero. This is achieved by extending the load w_0 to the end of the beam (blue dotted lines) and then adding the counterpart of the load (red dotted lines). This will result in a net load of zero. This is referred to as superposition and is only possible in problems without second order terms.

$$\langle x-a\rangle^n = \begin{cases} 0 \text{ for } (x-a) < 0 \text{ or } x < a \\ (x-a)^n \text{ for } x-a \geq 0 \text{ or } x \geq a \end{cases} \quad [77] \tag{D.5}$$

Referring to equation D.5, n = 0 for point moment, n = 1 for point force, n = 2 for uniformly distributed load and n = 3 for triangular distributed load. The three uniformly distributed loads mentioned above, combined with the terms in equation D.5, result into the moment line presented in equation D.6. For clarity, the blue term refers to both continuous and dotted loads (figure above) and the red term refers to the red dotted load.

$$M(x) = F_A\langle x-0\rangle^1 - M_A\langle x-0\rangle^0 - \frac{w_0}{2}\langle x-0\rangle^2 + \frac{w_0}{2}\langle x-a\rangle^2 \tag{D.6}$$

The parameter a in equation D.5 is the coordinate at which the force is nonzero looking in positive x-direction. Taking equation D.6 into account, the force, moment and blue distributed load start at $x = 0$ and the red distributed load at $x = a$. The moment line in equation D.7 describes the model that is depicted in figure D.1. Again, colour coding is used to point out which term in equation D.7 refers to which load in figure D.1. A triangular distributed load is incorporated into the singularity function as the slope of this distributed load: $\frac{w_2}{L}$.

$$M(x) = F_A\langle x-0\rangle^1 - M_A\langle x-0\rangle^0 - \frac{w_0}{2}\langle x-0\rangle^2 + \frac{w_0}{2}\langle x-d\rangle^2 - \frac{w_1}{2}\langle x-d\rangle^2 - \frac{w_2}{6L}\langle x-d\rangle^3 \tag{D.7}$$

Equations D.2, D.3 and D.4 are applied on equation D.7 for a subsequent calculation. This then results in equations D.8 and D.9, respectively the slope and deflection equation.

$$\frac{dy}{dx} = \frac{1}{EI}\left(\frac{F_A}{2}\langle x-0\rangle^2 - M_A\langle x-0\rangle^1 - \frac{w_0}{6}\langle x-0\rangle^3 + \frac{w_0}{6}\langle x-d\rangle^3 - \frac{w_1}{6}\langle x-d\rangle^3 - \frac{w_2}{24L}\langle x-d\rangle^4 + C_1\right) \tag{D.8}$$

$$y = \frac{1}{EI}\left(\frac{F_A}{6}\langle x-0\rangle^3 - \frac{M_A}{2}\langle x-0\rangle^2 - \frac{w_0}{24}\langle x-0\rangle^4 + \frac{w_0}{24}\langle x-d\rangle^4 - \frac{w_1}{24}\langle x-d\rangle^4 - \frac{w_2}{120L}\langle x-d\rangle^5 + C_1x + C_2\right) \tag{D.9}$$

The boundary conditions of the model depicted in figure D.1 are as follows:

1. $\frac{dy}{dx} = 0$ at x = 0
2. y = 0 at x = 0

Boundary condition 1 combined with equation D.8 results in $C_1 = 0$. Boundary condition 1 combined with equation D.9 results in $C_2 = 0$. Both equations are plotted in Matlab and the results can be observed in subfigures D.3b and D.3a.

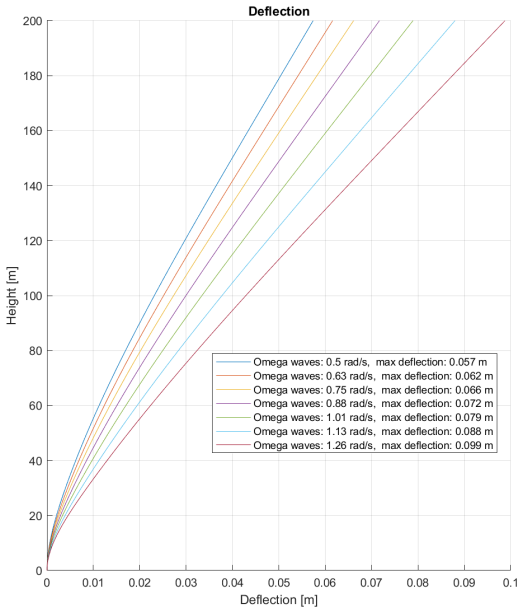

(a) Deflection of Euler-Bernoulli beam over height.

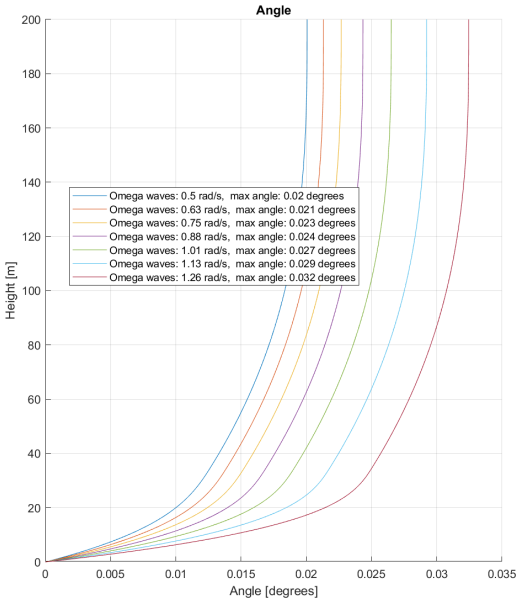

(b) Angle of Euler-Bernoulli beam over height.

For metocean input parameters of the beam model, moderate weather conditions were considered in which a ship like the Pioneering Spirit could still be operational. Other important input parameters together with the weather conditions are summed up below.

1. $H_s = 2.5\,m$
2. $T_p = 7.74\,s$
3. $U_{wind} = 16\,m/s$
4. $d = 35\,m$
5. $L = 165\,m$
6. $D_{outer} = 8.5\,m$
7. $wall\ thickness = 0.10\,m$
8. $Wave\ frequency\ spectrum = 0.08 - 0.20\,Hz$

It can be concluded that under these weather conditions and with aforementioned assumptions the deflection is somewhere between 5 to 10 centimeters in the absence of a nacelle under moderate weather conditions. The difference in deflection is caused by a varying wave frequency input parameter. The wave frequency spectrum is derived from the JONSWAP frequency spectrum, which is a never fully developed wave spectrum. When analytically solving a system with one degree of freedom, the achieved mode shape will automatically be the first mode shape of a cantilever beam [76]. Figure D.3a, when normalised, corresponds to this first mode shape. This carefully modelled deflection allows something to be said about subsequent models. If for instance a mass is placed on top of the beam, the deflection will be significantly larger.

The maximum angle related to the maximum deflection in section D is approximately 0.03 degrees or $5.2 * 10^{-4}$ radians. So it is safe to assume the small-angle approximation as demonstrated in equations 4.7 and 4.8.

E

Support structure extra results

E.1. Mode Shapes

Three modeshapes of the wind turbine support structure in the $z-x$ plane are plotted below. The mode shapes are identical in the $z-y$ plane.

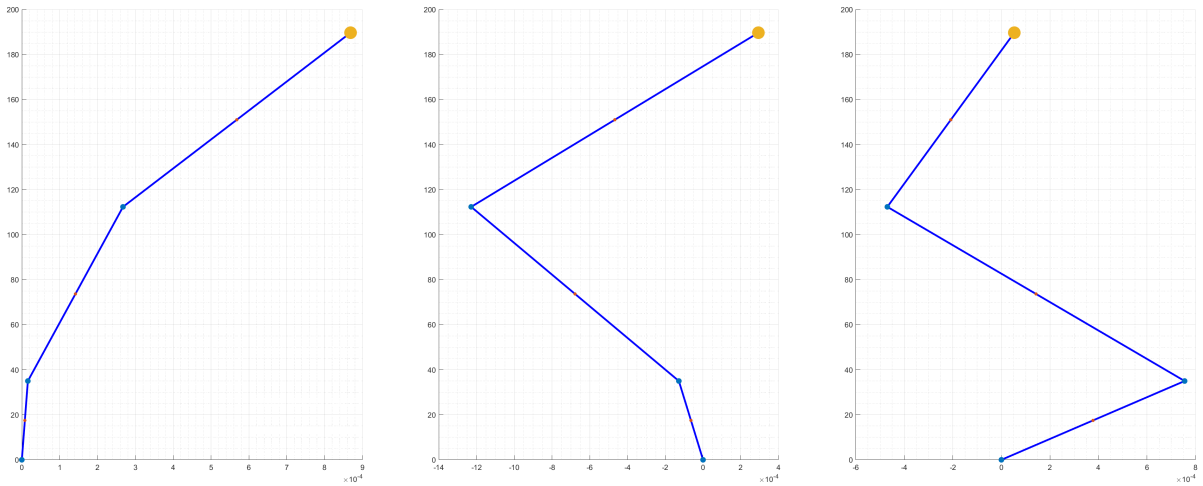

(a) First mode shape (b) Second mode shape (c) Third mode shape

Figure E.1: Support structure mode shapes.

E.2. Extra results

This section contains the results of the support structure multi-body model of two case studies. The case studies are discussed in 6. Firstly, the results of the case study 1 are shown below. Secondly, the results of case study 3 are depicted.

E.2.1. Case study 1

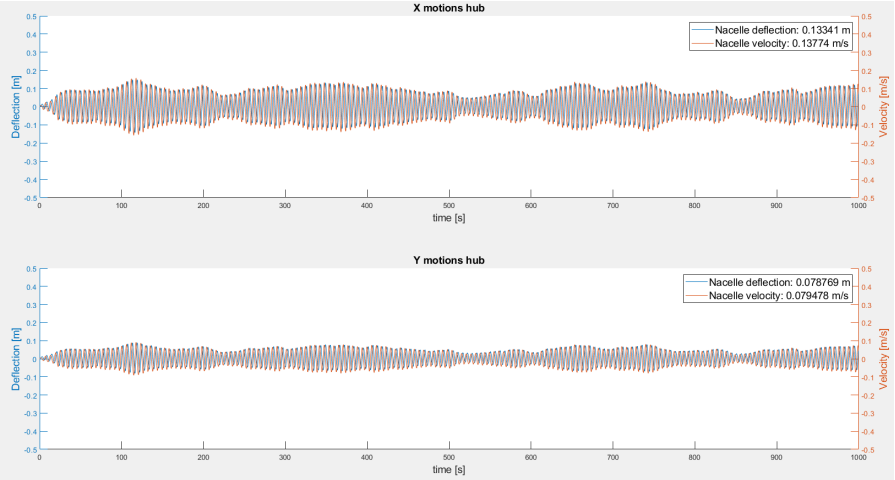

Figure E.2: X- and y-motions of the nacelle of the first case study.

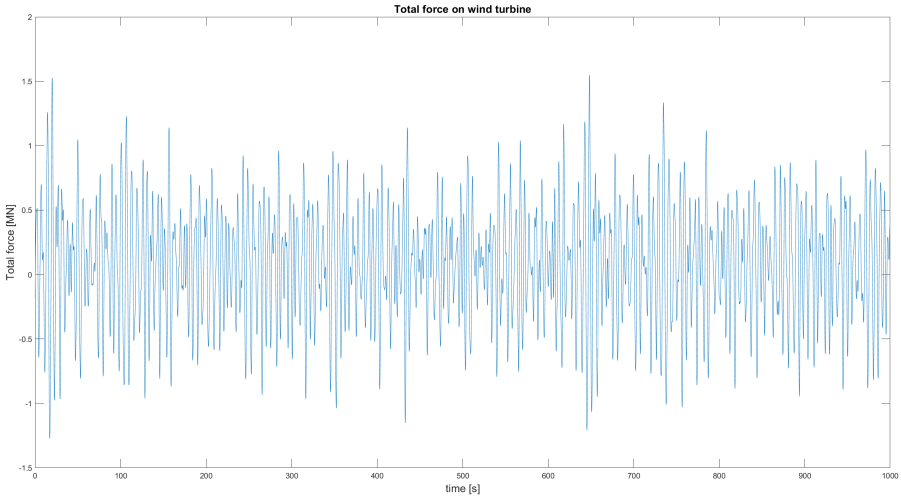

Figure E.3: Total force on support structure of the first case study.

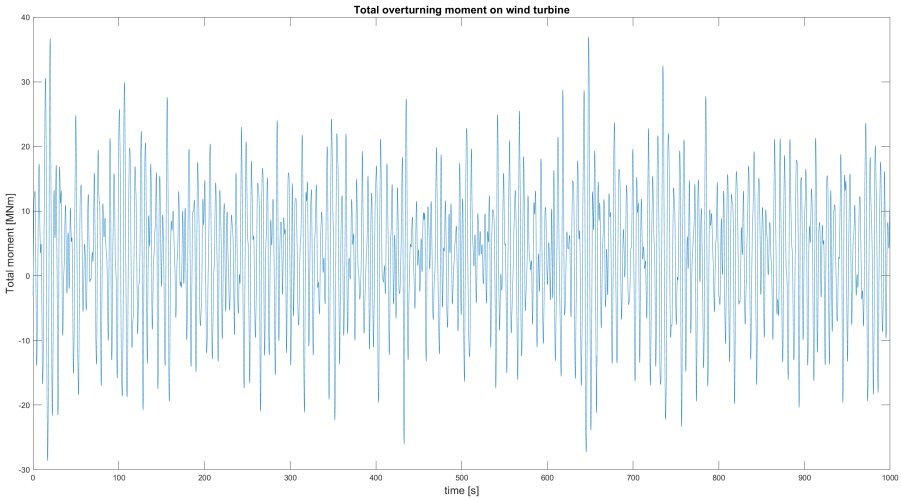

Figure E.4: Total overturning moment on support structure of the first case study.

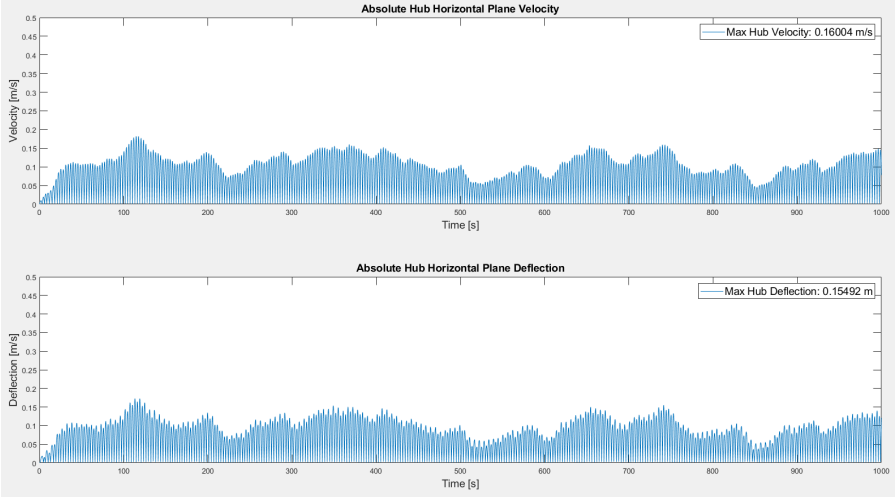

Figure E.5: Absolute values of horizontal nacelle motions of the first case study.

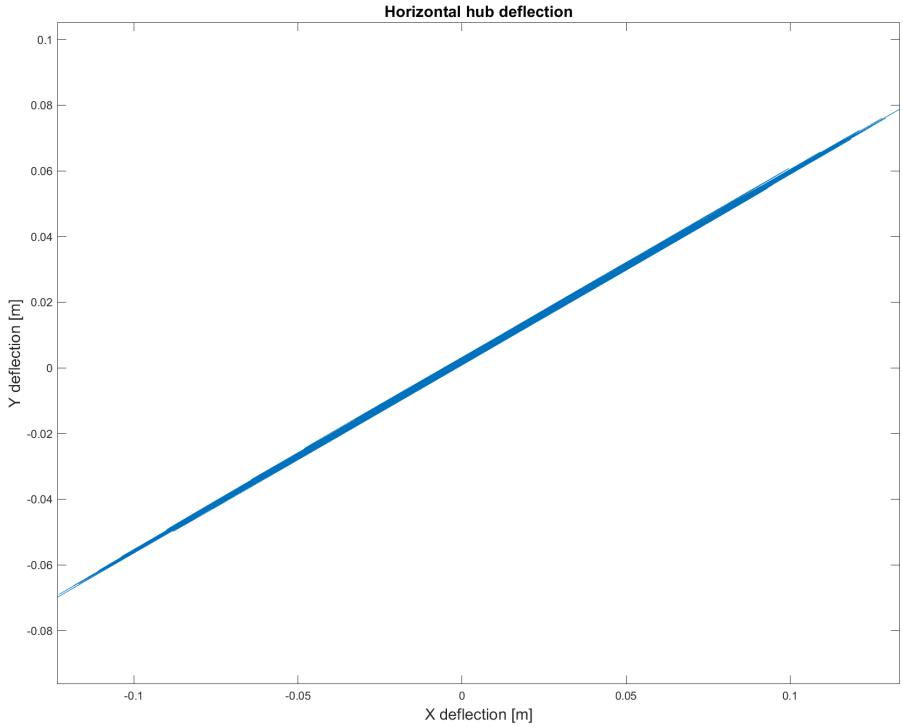

Figure E.6: Nacelle deflection with the input parameters of the first case study.

E.2.2. Case study 2

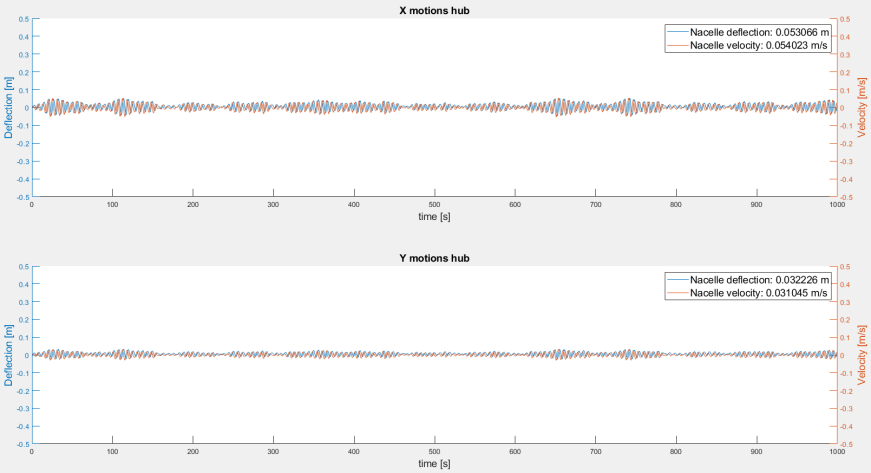

Figure E.7: X- and y-motions of the nacelle of the second case study.

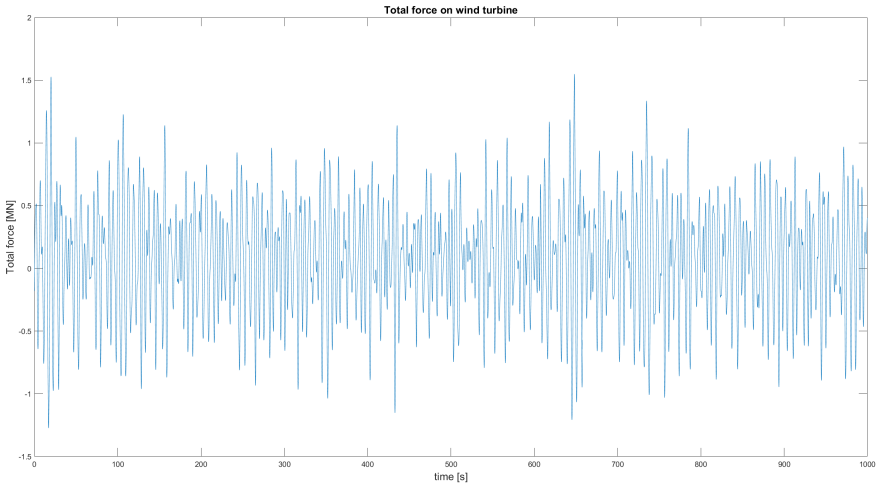

Figure E.8: Total force on support structure of the second case study.

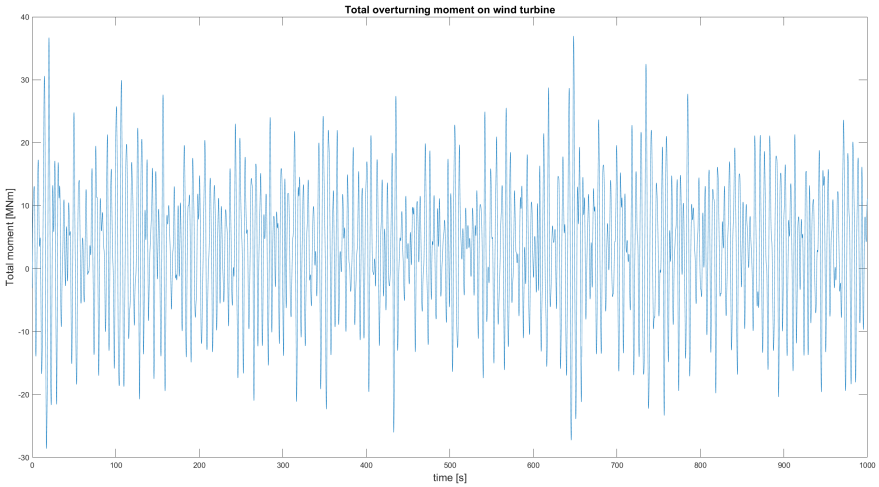

Figure E.9: Total overturning moment on support structure of the second case study.

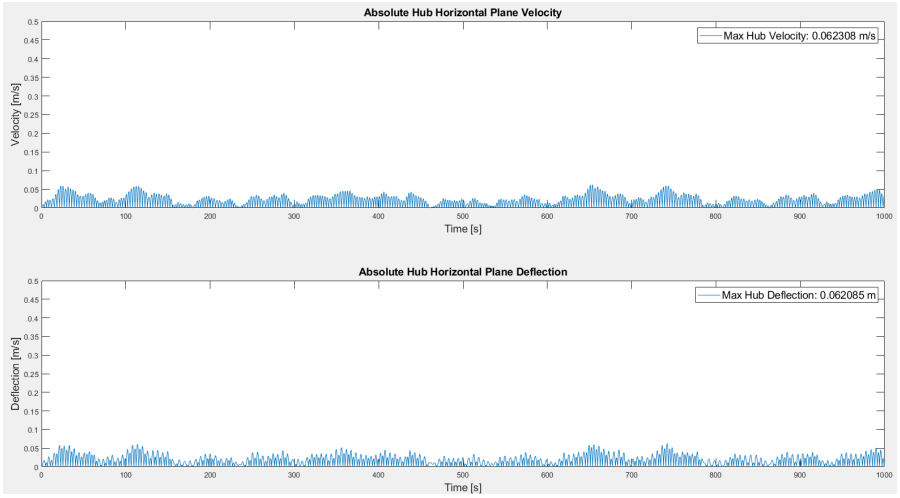

Figure E.10: Absolute values of horizontal nacelle motions of the second case study.

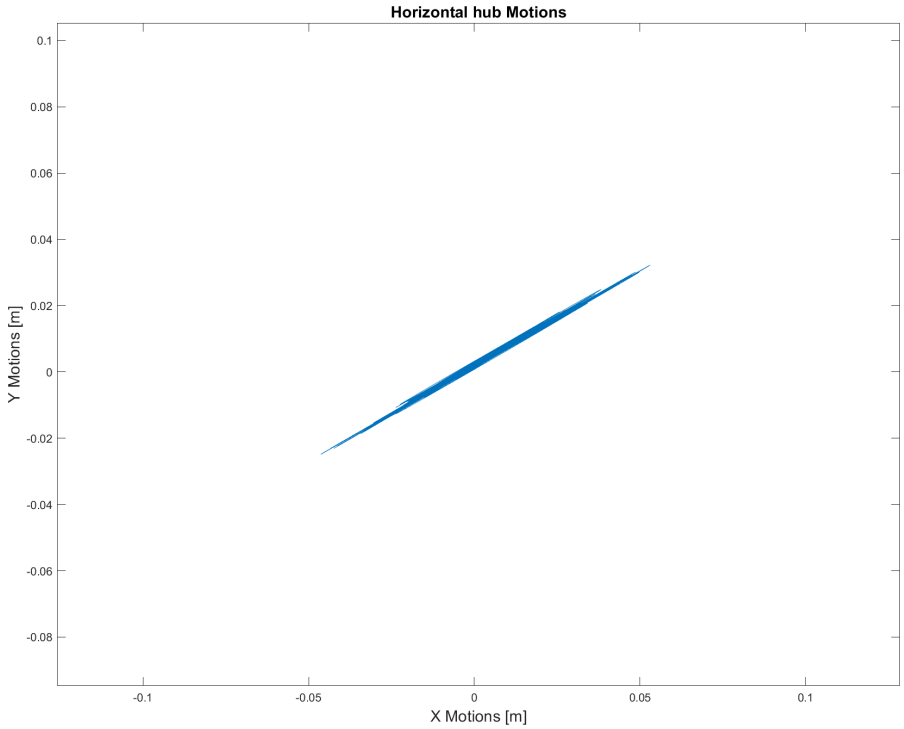

Figure E.11: Nacelle deflection with the input parameters of the second case study.

F

Blade extra results

F.1. Mode Shapes

The nine modeshapes of the wind turbine blade of simulation one are plotted below. In figure F.1, the pitch motion of the blade is displayed. In figure F.2, the yaw motion of the blade is displayed. In figure F.3 the pendulum motion of the blade in the $z-x$ is depicted. In figure F.4 the pendulum motion of the blade in the $z-y$ is depicted. In figure F.5, the 1^{st} modeshape of the blade in the $z-x$ plane is shown. In figure F.6, the cable elongation modeshape can be seen. In figure F.7, the 1^{st} modeshape of the blade in the $x-y$ plane is displayed. In figure F.8, the 2^{nd} modeshape of the blade in the $z-x$ plane is shown. In figure F.9, the 2^{nd} modeshape of the blade in the $x-y$ plane can be seen.

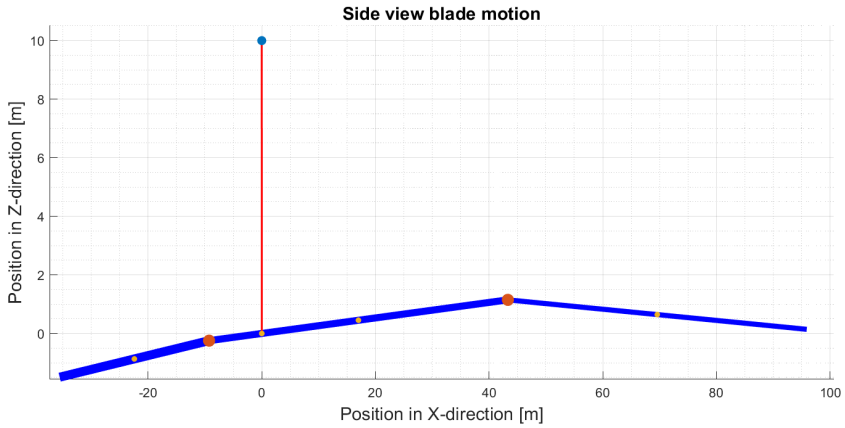

Figure F.1: 1^{st} modeshape of blade multi-body system.

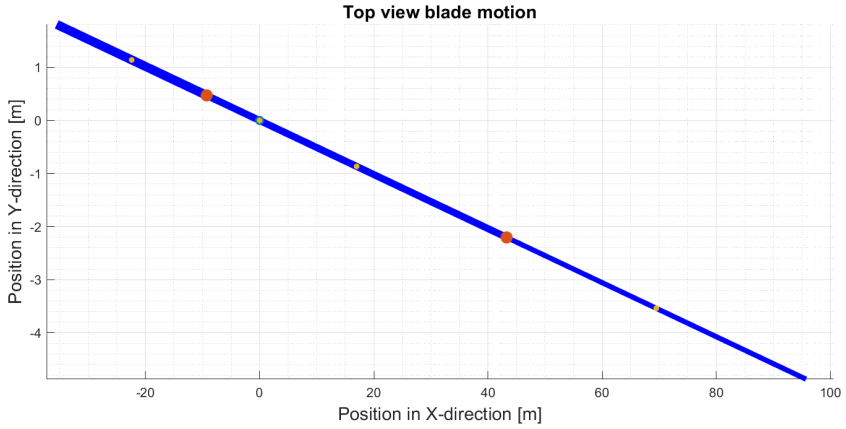

Figure F.2: 2^{nd} modeshape of blade multi-body system.

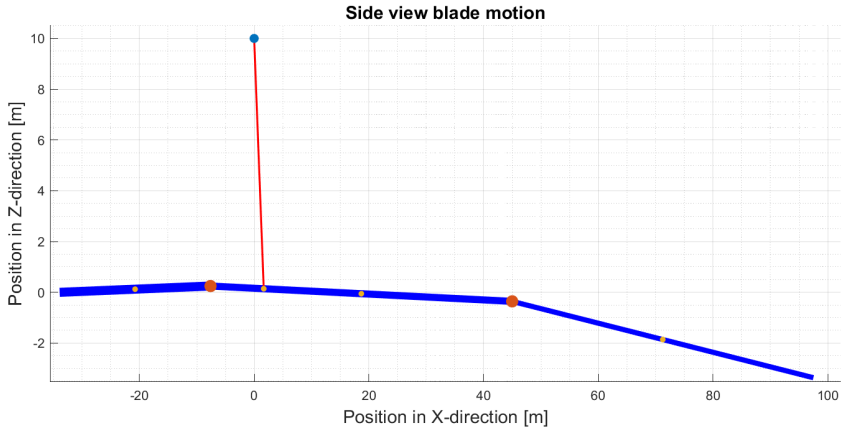

Figure F.3: 3^{rd} modeshape of blade multi-body system.

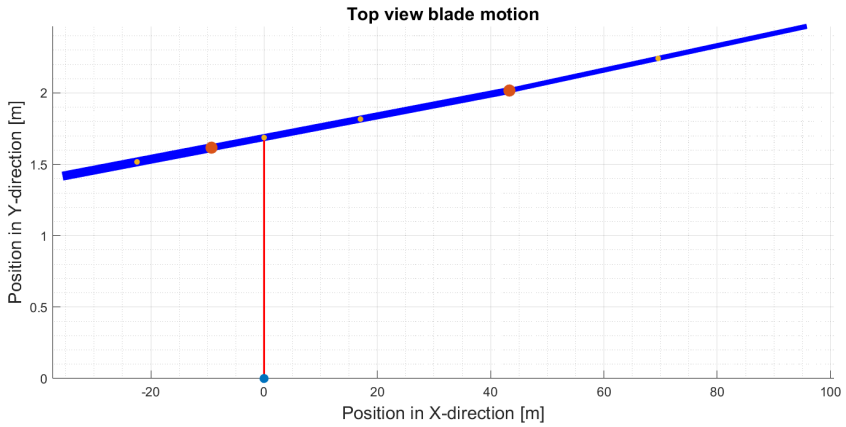

Figure F.4: 4^{th} modeshape of blade multi-body system.

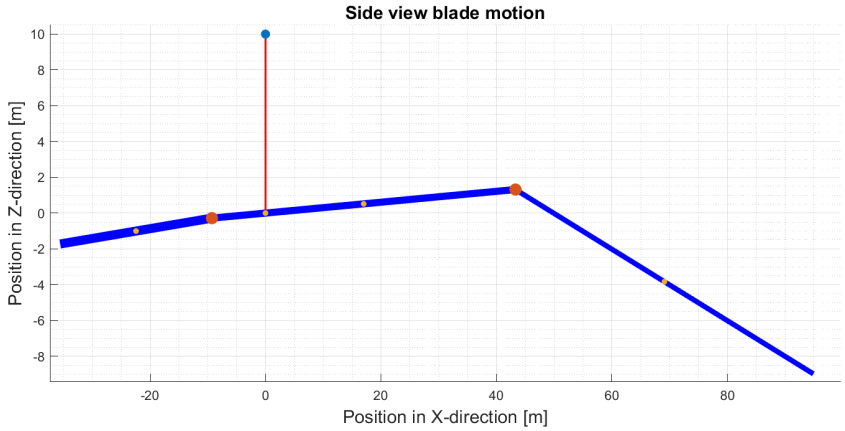

Figure F.5: 5^{th} modeshape of blade multi-body system.

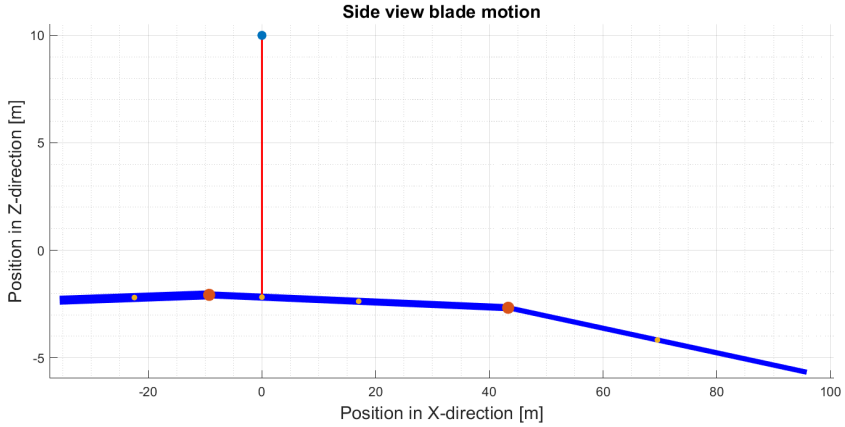

Figure F.6: 6^{th} modeshape of blade multi-body system.

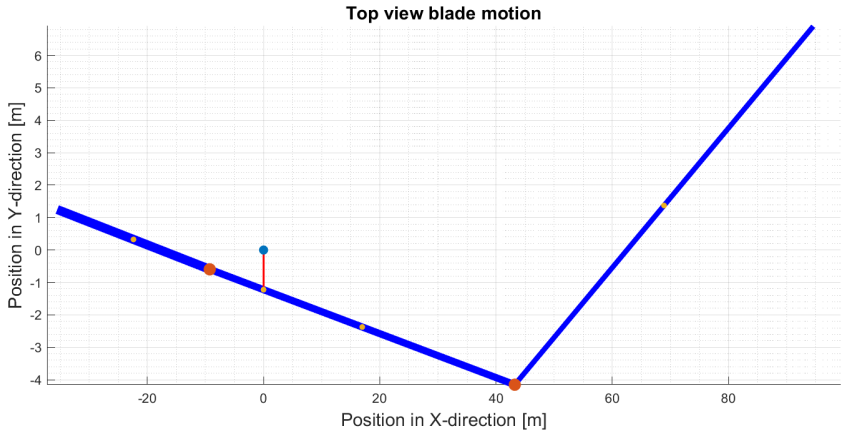

Figure F.7: 6^{th} modeshape of blade multi-body system.

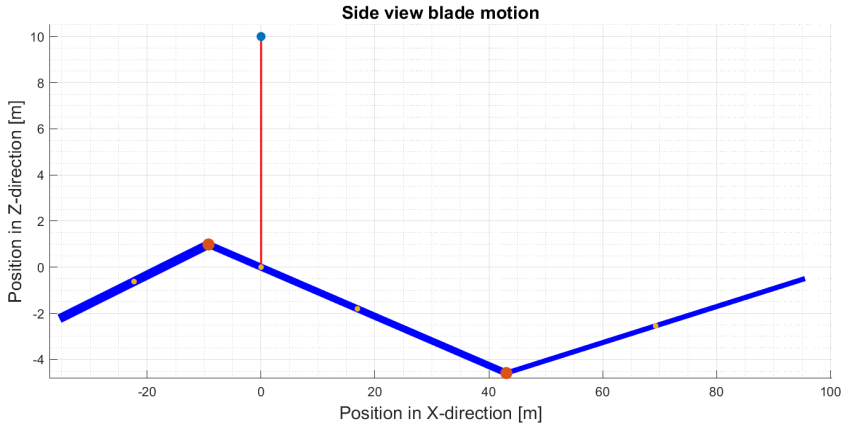

Figure F.8: 8^{th} modeshape of blade multi-body system.

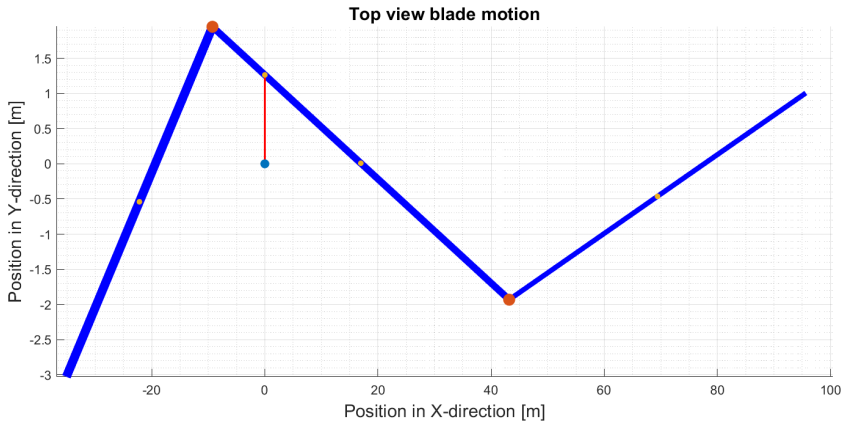

Figure F.9: 9^{th} modeshape of blade multi-body system.

F.2. Extra Results

This section contains the results of two case studies of the multi-body blade model. The case studies are discussed in 6. Firstly, the results of the case study 1 are shown below. Secondly, the results of case study 3 are depicted.

F.2.1. Case study 1

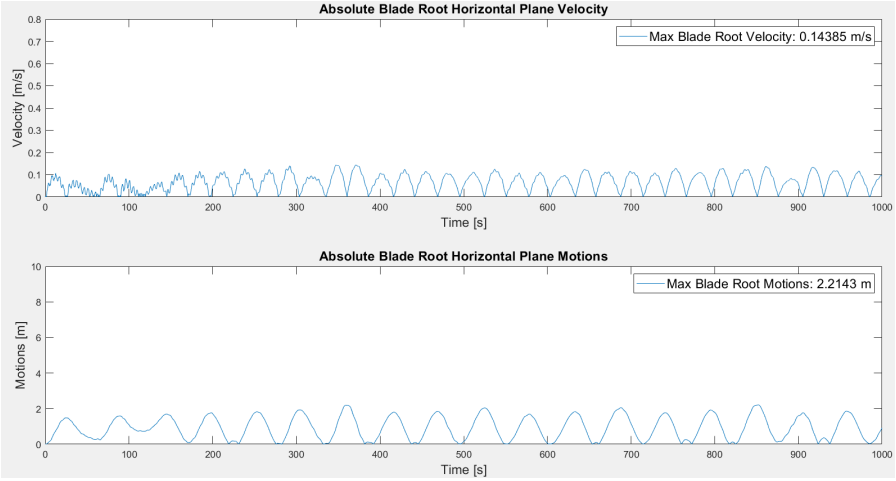

Figure F.10: Absolute values of horizontal blade motions of first case study.

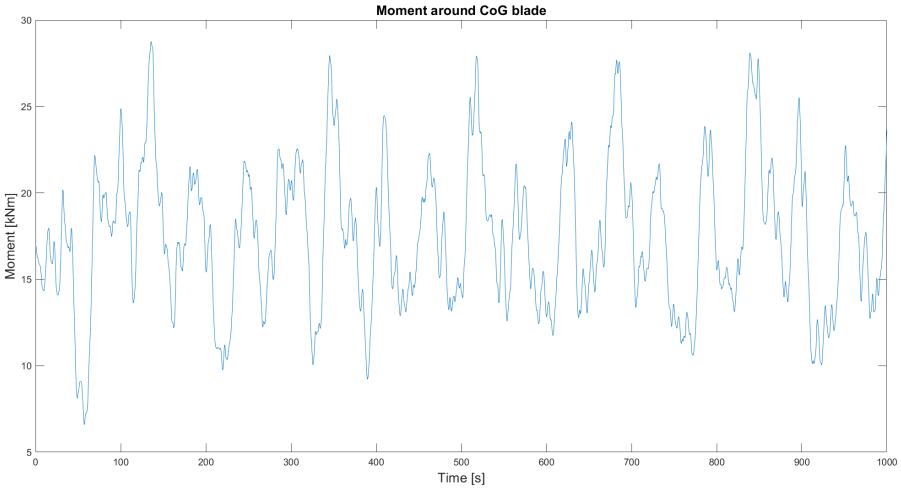

Figure F.11: Moment acting on blade around centre of gravity of first case study.

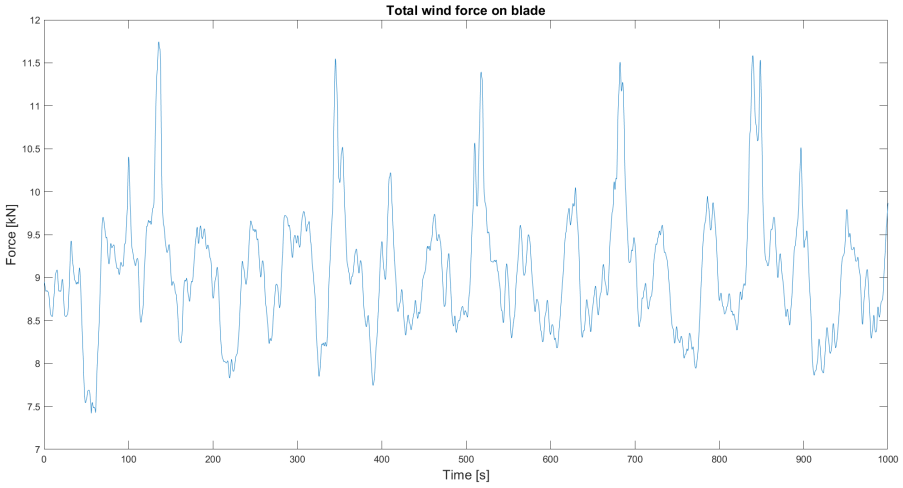

Figure F.12: Total wind force acting on blade in calm weather conditions.

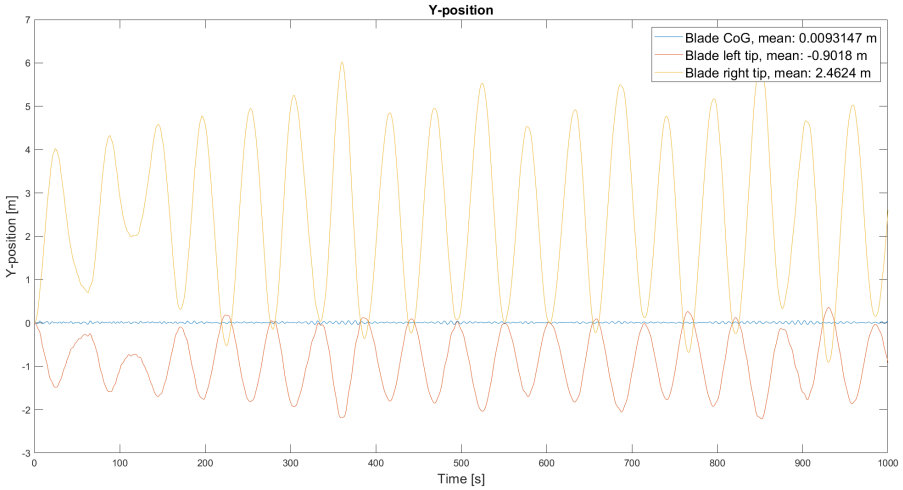

Figure F.13: Deflections of blade in y-direction of first case study.

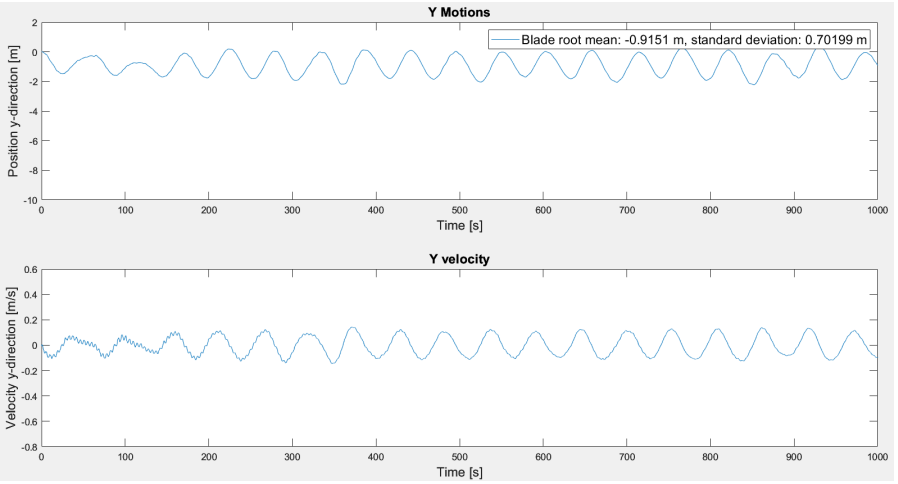

Figure F.14: Motions of blade root in y-direction of first case study.

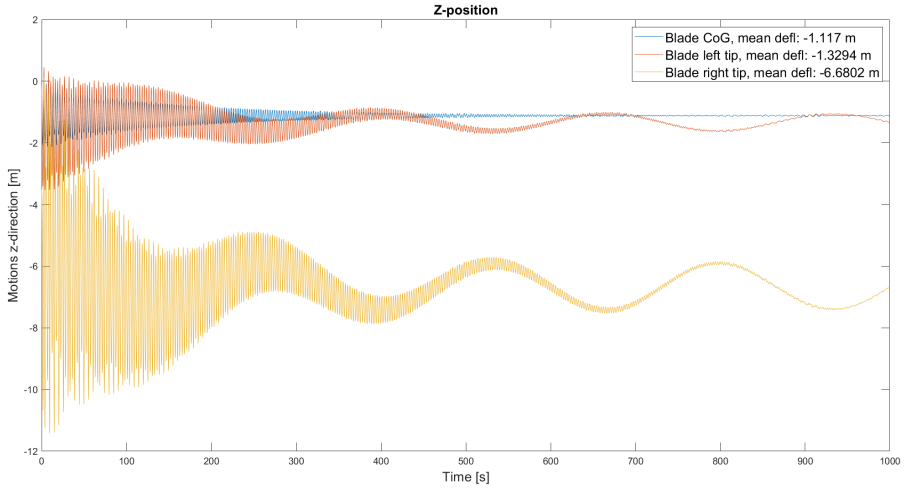

Figure F.15: Deflections of blade in z-direction in first case study.

F.2.2. Case study 2

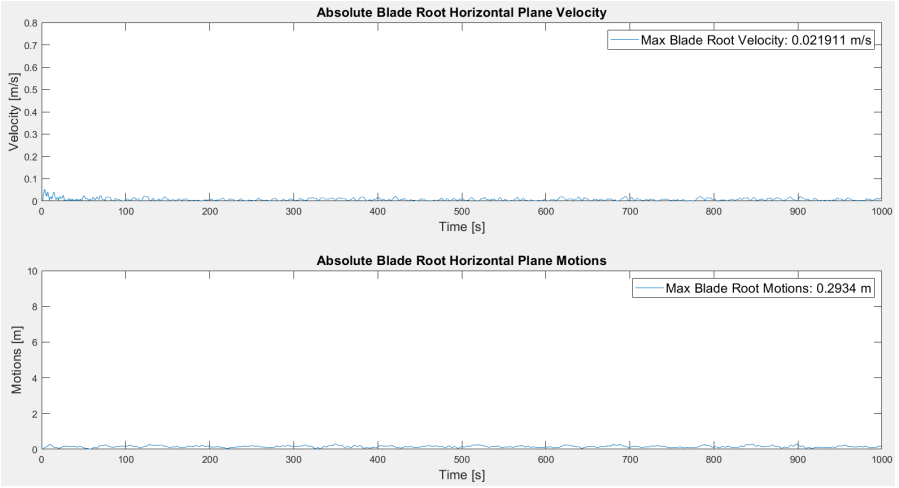

Figure F.16: Absolute values of horizontal blade motions of second case study.

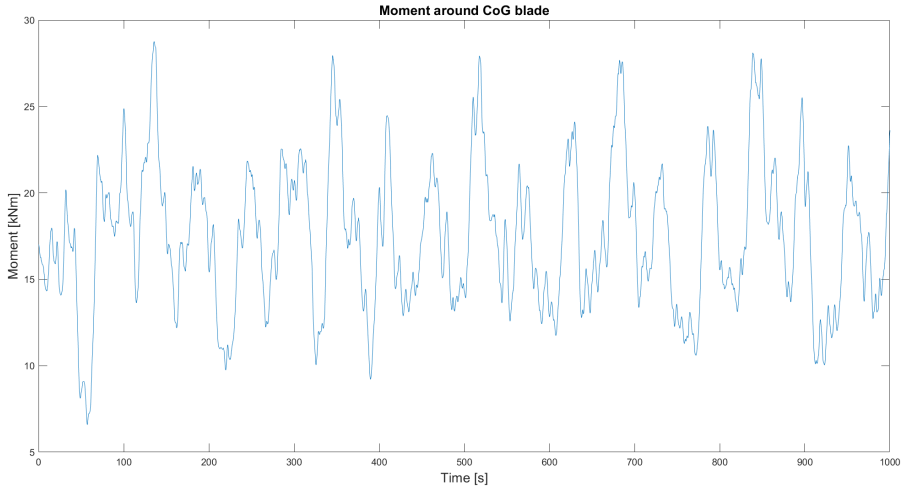

Figure F.17: Moment acting on blade around centre of gravity of second case study.

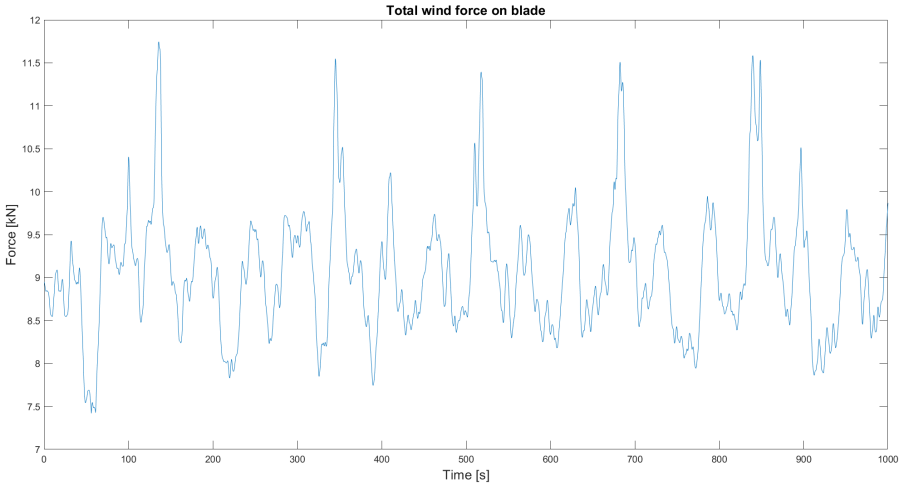

Figure F.18: Total wind force acting on blade in calm weather conditions.

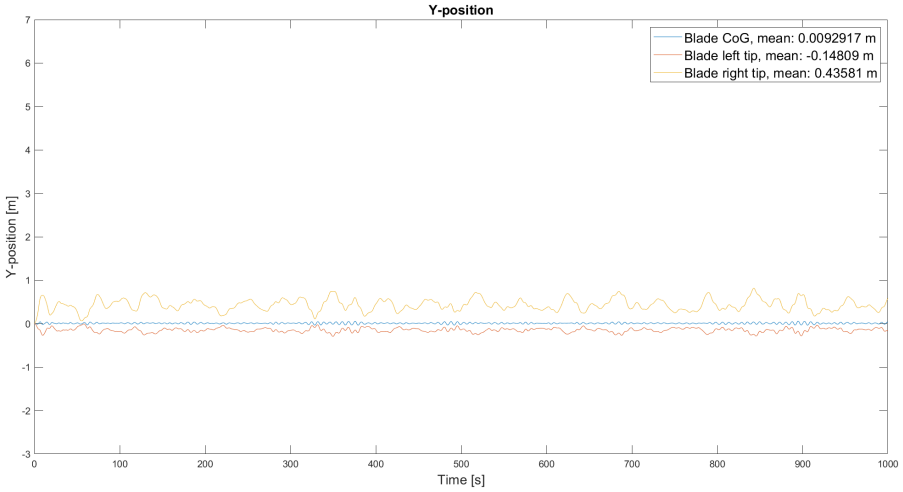

Figure F.19: Deflections of blade in y-direction of second case study.

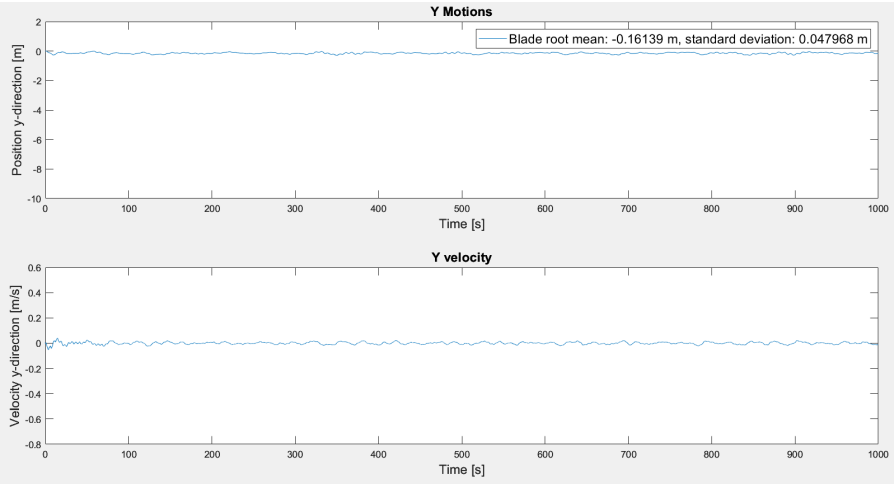

Figure F.20: Motions of blade root in y-direction of second case study.

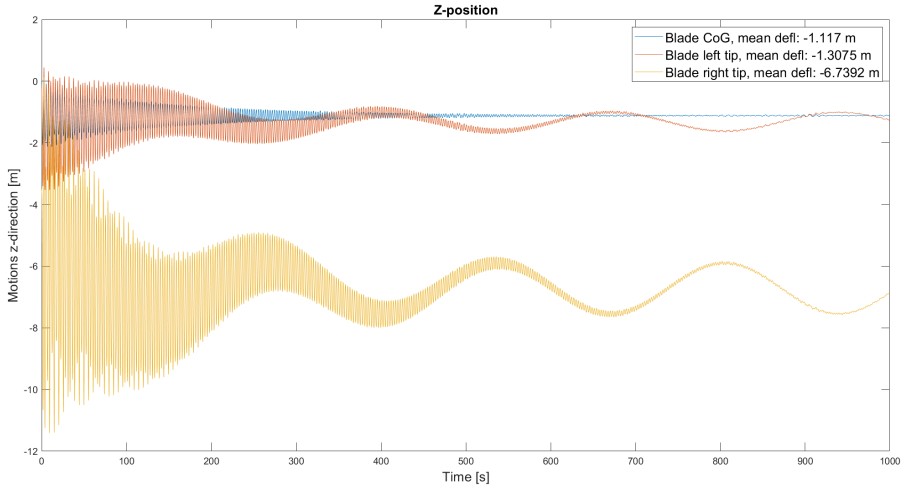

Figure F.21: Deflections of blade in z-direction in second case study.

Bibliography

[1] Redactie, "China drijft wereldwijde offshore windinstallaties in 2021 tot nieuw record," 2 2022. [Online]. Available: https://windenergie-nieuws.nl/19/china-drijft-wereldwijde-offshore-windinstallaties-in-2021-nieuw-record/

[2] WindEurope asbl/vzw, "Offshore wind energy," 9 2022. [Online]. Available: https://windeurope.org/policy/topics/offshore-wind-energy/

[3] "Wind turbine growth, EWEA." [Online]. Available: https://www.researchgate.net/figure/Growth-in-size-of-wind-turbines-since-1980-and-prospect-KEY-POINT-Scaling-up-turbines_fig1_320867742

[4] P. Schaumann and M. Böhm, "Development and challenges of support structures for offshore wind turbines," 2021. [Online]. Available: https://doi.org/10.1002/cepa.

[5] "Structural Analysis - HOWaT | Hybrid Offshore Wind and Tidal." [Online]. Available: https://www.esru.strath.ac.uk//EandE/Web_sites/16-17/windandtidal/structuralAnalysis.html

[6] Global offshore renewable map | 4c offshore. [Online]. Available: https://map.4coffshore.com/offshorewind/

[7] U. D. of Energy, "drivetrainpdf," 2010.

[8] Internetbureau Antum [www.antum.nl]. Barge master crane trials. [Online]. Available: https://www.barge-master.com/item/barge-master-crane-trials/

[9] I. J. W. Welleman Blad, "CTB3330 : VERGEET-MIJ-NIETJES CTB3330 FORMULES," Delft University of Technology, Tech. Rep.

[10] R. P. L. Nijssen, M. J. De Ruiter, F. Lahuerta, and E. Kuipers, "CONNECTION METHODS IN WIND TURBINE ROTOR BLADES Title: Connection methods in wind turbine rotor blades WMC," TNO, Tech. Rep., 2018. [Online]. Available: www.wmc.eu

[11] A. John Edwin Ashworth Briggs, H. Nath Dhakal, A. J. E Ashworth Briggs, Z. Y. Zhang, and H. N. Dhakal, "T-Bolt Bearing Strengths in Composite Blade Applications Gas generator engine exhaust heat recovery project View project Development of sustainable composites. View project T-BOLT BEARING STRENGTHS IN COMPOSITE BLADE APPLICATIONS," Tech. Rep., 2012. [Online]. Available: https://www.researchgate.net/publication/263581179

[12] Hindcastš. [Online]. Available: https://app.metoceanview.com/hindcast-squared/#/stats-point/lng/

[13] F. O. Windcarrier, "Classification and Rules," Tech. Rep., 2012. [Online]. Available: www.windcarrier.com

[14] Wikipedia contributors, "Wind power in China," 7 2022. [Online]. Available: https://en.wikipedia.org/wiki/Wind_power_in_China

[15] WindEurope asbl/vzw, "WindEurope - the voice of the wind energy industry," 11 2022. [Online]. Available: https://windeurope.org/

[16] R. O'SUllivan, "210224_windeurope_combined_2020_stats," Wind energy in Europe, 2020.

[17] Ministerie van Volkshuisvesting, Ruimtelijke Ordening en Milieubeheer, "Windenergie op zee," 9 2022. [Online]. Available: https://www.rijksoverheid.nl/onderwerpen/duurzame-energie/windenergie-op-zee

[18] f. given i=N., given=Nana, "Will offshore wind power the energy transition in the Netherlands?" 10 2021. [Online]. Available: https://www.airswift.com/blog/wind-energy-projects-netherlands

[19] Sif Group, "Monopiles & Transition Pieces," 4 2022. [Online]. Available: https://sif-group.com/en/monopiles-and-transition-pieces/

[20] "Jan De Nul laat Voltaire te water, het grootste jack-up installatieschip ter wereld," 1 2022. [Online]. Available: https://www.jandenul.com/nl/nieuws/jan-de-nul-laat-voltaire-te-water-het-grootste-jack-installatieschip-ter-wereld

[21] J. L. Tangler, "The Evolution of Rotor and Blade Design," National Renewable Energy Laboratory, Tech. Rep., 2000. [Online]. Available: http://www.doe.gov/bridge

[22] P. S. Veers, T. D. Ashwill, H. J. Sutherland, D. L. Laird, D. W. Lobitz, D. A. Griffin, J. F. Mandell, W. D. Musial, K. Jackson, M. Zuteck, A. Miravete, S. W. Tsai, and J. L. Richmond, "Trends in the Design, Manufacture and Evaluation of Wind Turbine Blades," WIND ENERGY Wind Energ, vol. 6, pp. 245–259, 2003.

[23] V. Martínez, A. Güemes, D. Trias, and N. Blanco, "Numerical and experimental analysis of stresses and failure in T-bolt joints," Composite Structures, vol. 93, no. 10, pp. 2636–2645, 9 2011.

[24] A. S. Verma, Z. Jiang, N. P. Vedvik, Z. Gao, and Z. Ren, "Impact assessment of a wind turbine blade root during an offshore mating process," Engineering Structures, vol. 180, pp. 205–222, 2 2019.

[25] Y. E. Liu, "Monopile Forever Overcoming the Technical Boundaries of Monopile Foundations in Deep Waters," Delft University of Technology, Tech. Rep., 2021. [Online]. Available: http://repository.tudelft.nl/.

[26] D. Bang, H. Polinder, G. Shrestha, and J. Ferreira, "Review of Generator Systems for Direct-Drive Wind Turbines," Delft University of Technology, Tech. Rep.

[27] M. Tandjaoui, C. Benachaiba, O. Abdelkhalek, and C. Banoudjafar, "Role of power electronics in grid integration of renewable energy systems," Journal of Electrical Engineering, vol. 16, no. 1, pp. 6–6, 2016.

[28] S. G. R. Energy, "The winds of change have never been stronger," Tech. Rep.

[29] E. Gaertner, J. Rinker, L. Sethuraman, F. Zahle, B. Anderson, G. Barter, N. Abbas, F. Meng, P. Bortolotti, W. Skrzypinski, G. Scott, R. Feil, H. Bredmose, K. Dykes, M. Shields, C. Allen, and A. Viselli, "Definition of the IEA Wind 15-Megawatt Offshore Reference Wind Turbine Technical Report," National Renewable Energy Laboratory, Tech. Rep., 2020. [Online]. Available: www.nrel.gov/publications.

[30] C. . Bak, F. . Zahle, R. . Bitsche, T. . Kim, A. . Yde, L. Henriksen, . Christian, M. Hansen, . Hartvig, J. Blasques, A. Pedro, . Amaral, M. . Gaunaa, A. Natarajan, C. Bak, F. Bitsche, R. Kim, T. Yde, A. Henriksen, L. C. Hansen, J. P. A. A. Gaunaa, and M. Natarajan, "General rights The DTU 10-MW Reference Wind Turbine). The DTU 10-MW Reference Wind Turbine. Sound/Visual production (digital)," DTU, Tech. Rep., 2013.

[31] M. Ghassempour, G. Failla, and F. Arena, "Vibration mitigation in offshore wind turbines via tuned mass damper," Engineering Structures, vol. 183, pp. 610–636, 3 2019.

[32] Y. Zhao, Z. Cheng, P. C. Sandvik, Z. Gao, T. Moan, and E. Van Buren, "Numerical modeling and analysis of the dynamic motion response of an offshore wind turbine blade during installation by a jack-up crane vessel," Ocean Engineering, vol. 165, pp. 353–364, 10 2018.

[33] Liebherr. Lr 1250.1 crawler crane. [Online]. Available: https://www.liebherr.com/en/can/products/mobile-and-crawler-cranes/crawler-cranes/lr-crawler-cranes/details/lr1250.html

[34] Liftra. Lt975 - blade dragon. [Online]. Available: https://www.liftra.com/products/lt975-blade-dragon.html

[35] Boom lock - tagline systems. [Online]. Available: http://www.high-wind.eu/boomlock/

[36] Boom lock allows offshore installation at higher wind speeds. [Online]. Available: https://www.offshorewindindustry.com/news/boom-lock-allows-offshore-installation-higher#:%7E:text=The%20Boom%20Lock%20is%20a,time%20can%20be%20drastically%20reduced.

[37] B. Ummels, "Bart Ummels, TU Delft Supervisor," 2022.

[38] Z. Jiang, Z. Gao, Z. Ren, Y. Li, and L. Duan, "A parametric study on the final blade installation process for monopile wind turbines under rough environmental conditions," Engineering Structures, vol. 172, pp. 1042–1056, 10 2018.

[39] Z. Ren, Z. Jiang, Z. Gao, and R. Skjetne, "Active tugger line force control for single blade installation," Wind Energy, vol. 21, no. 12, pp. 1344–1358, 12 2018.

[40] R. Rana and T. T. Soong, "Parametric study and simplified design of tuned mass dampers," Tech. Rep. 3, 1998.

[41] F. Taddei, M. L, S. Klinkel, C. Butenweg, and O. Altay, "Seismic protection of wind turbines using tuned mass dampers," 08 2014.

[42] M. Breivik, S. Kvaal, and P. Østby, "From Eureka to K-Pos: Dynamic Positioning as a Highly Successful and Important Marine Control Technology," IFAC-PapersOnLine, vol. 48, no. 16, pp. 313–323, 1 2015.

[43] M. Gaunaa, L. Bergami, S. Guntur, and F. Zahle, "First-order aerodynamic and aeroelastic behavior of a single-blade installation setup," in Journal of Physics: Conference Series, vol. 524, no. 1. Institute of Physics Publishing, 2014.

[44] E. A. Meindl and D. B. Gilhousen, "Determining the Power-Law Wind-Profile Exponent under Near-Neutral Stability Conditions at Sea," 1993.

[45] M. Zaaijer, A. Viré, R. B. Dos, S. Pereira, and A. Daneshbodi, "Introduction to wind turbines: physics and technology Editing (text and videos)," Delft University of Technology, Tech. Rep., 2021.

[46] E. de Vries, "Haliade-X uncovered: GE aims for 14MW," 3 2019.

[47] https://www.vestas.com/en/products/offshore/V236-15MW, "V236-15.0 MW," 2021.

[48] f. given i=S.D., "Structural capacity and the 20 MW wind turbine," 9 2010. [Online]. Available: https://journals.sagepub.com/doi/abs/10.1243/09576509JPE973?journalCode=piac

[49] C. E. S. d. Souza and E. E. Bachynski-Polić, "Design, structural modeling, control, and performance of 20 MW spar floating wind turbines," Marine Structures, vol. 84, 7 2022.

[50] Pendulum system - an overview | sciencedirect topics. [Online]. Available: https://www.sciencedirect.com/topics/engineering/pendulum-system

[51] S. Adhikari and S. Bhattacharya, "Dynamic analysis of wind turbine towers on flexible foundations," Shock and Vibration, vol. 19, no. 1, pp. 37–56, 2012.

[52] J. v. d. Temple, Design of support structures for offshore wind turbines. Published and distributed by the author in cooperation with Offshore Engineering, 2006.

[53] D. Morin, "The Lagrangian Method," Harvard University, Tech. Rep., 2007.

[54] G. J. Aubrecht, "Conservation of Energy, Overview," Encyclopedia of Energy, pp. 673–686, 2004. [Online]. Available: https://www.sciencedirect.com/topics/engineering/conservation-of-energy-principle

[55] Libretexts. 10.4: Rayleighs dissipation function. [Online]. Available: https://phys.libretexts.org/Bookshelves/Classical_Mechanics/Variational_Principles_in_Classical_Mechanics_(Cline)/10%3A_Nonconservative_Systems/10.04%3A_Rayleighs_Dissipation_Function

[56] Kurstjens, M, "Michel kurstjens: Product strategy director sif group," 2020.

[57] f. given i=L.H., given=Leo, Waves in Oceanic and Coastal Waters. Cambridge, United Kingdom: Cambridge University Press, 2010.

[58] P. Wang, M. Zhao, X. Du, J. Liu, and C. Xu, "Wind, wave and earthquake responses of offshore wind turbine on monopile foundation in clay," Soil Dynamics and Earthquake Engineering, vol. 113, pp. 47–57, 10 2018.

[59] Versteijlen, "Identification of effective 1D soil models for large-diameter offshore wind turbine foundations based on in-situ seismic measurements and 3D modelling," 2018. [Online]. Available: https://doi.org/10.4233/uuid:55e7ff00-02ba-495d-9863-889bb92ee548

[60] A. Malekjafarian, S. Jalilvand, P. Doherty, and D. Igoe, "Foundation damping for monopile supported offshore wind turbines: A review," 5 2021.

[61] f. given i=C.P., given=Cadence Pcb, "Resonant Frequency vs. Natural Frequency in Oscillator Circuits | Advanced PCB Design Blog | Cadence," 10 2022. [Online]. Available: https://resources.pcb.cadence.com/blog/2019-resonant-frequency-vs-natural-frequency-in-oscillator-circuits

[62] E. V. Lewis, "Principles of Naval Architecture (Second Revision), Volume III (1)," Principles of Naval Architacture, 1989.

[63] S. Windyty, "Windy as forecasted." [Online]. Available: https://www.windy.com/

[64] Z. Jiang, "The impact of a passive tuned mass damper on offshore single-blade installation," Journal of Wind Engineering and Industrial Aerodynamics, vol. 176, pp. 65–77, 5 2018.

[65] A. S. Verma, Z. Jiang, Z. Gao, and N. P. Vedvik, "Effects of a passive tuned mass damper on blade root impacts during the offshore mating process," Marine Structures, vol. 72, p. 102778, 7 2020.

[66] A. Engineering, "AllSeas Engineering Database," 8 2022.

[67] N. Karthikeyan and T. Suthakar, "Computational studies on small wind turbine performance characteristics," in Journal of Physics: Conference Series, vol. 759, no. 1. Institute of Physics Publishing, 11 2016.

[68] S. G. R. Energy, "The SG 11.0-200 DD Power for generations," Tech. Rep.

[69] K. E. Y. Creusen, G. Misios, J. S. Winkes, and M. Veljkovic, "Introducing the C1 Wedge Connection," Steel Construction, vol. 15, no. 1, pp. 13–25, 2 2022.

[70] A. K. Sengupta, "Stress Concentration."

[71] L. Manuel, P. T. Nguyen, J. Canning, R. G. Coe, A. C. Eckert-Gallup, and N. Martin, "Alternative approaches to develop environmental contours from metocean data," Journal of Ocean Engineering and Marine Energy, vol. 4, no. 4, pp. 293–310, 11 2018.

[72] Workability analysis. [Online]. Available: https://www.orca-offshore.com/workability-analysis/

[73] "DNVGL-ST-N001," DNV GL, 2018.

[74] A. Hölzer and M. Sommerfeld, "New simple correlation formula for the drag coefficient of non-spherical particles," Powder Technology, vol. 184, no. 3, pp. 361–365, 6 2008.

[75] T. Haukaas and E.-B. Beams, "Euler-Bernoulli Beams," University of British Columbia, Tech. Rep., 2020.

[76] M. H. Richardson, "Is it a mode shape, or an operating deflection shape?" Vibrant Technology, Inc., Tech. Rep.

[77] Libretexts. 7.4: Deflection by method of singularity function. [Online]. Available: https://eng.libretexts.org/Bookshelves/Mechanical_Engineering/Introduction_to_Aerospace_Structures_and_Materials_(Alderliesten)/02%3A_Analysis_of_Statically_Determinate_Structures/07%3A_Deflection_of_Beams-_Geometric_Methods/7.04%3A_Deflection_by_Method_of_Singularity_Function